

BABAR Analysis Document # 3000,

Version 3

May 26, 2021

Study of the process $e^+e^- \rightarrow \pi^+\pi^-\pi^0$ using initial state radiation with *BABAR*

V. P. Druzhinin, E. A. Kozyrev, and E. P. Solodov

Budker Institute of Nuclear Physics, Novosibirsk 630090, Russia

The process $e^+e^- \rightarrow \pi^+\pi^-\pi^0\gamma$ is studied at a center-of-mass energy near the $\Upsilon(4S)$ resonance using a 469 fb^{-1} data sample collected with the *BABAR* detector at the PEP-II collider.

Contents

I. Introduction	4
II. The <i>BABAR</i> detector and data samples	5
III. Event selection	6
IV. Background estimation and subtraction	13
A. $e^+e^- \rightarrow K^+K^-\pi^0\gamma$	13
B. $e^+e^- \rightarrow \pi^+\pi^-\gamma$	15
C. $e^+e^- \rightarrow \pi^+\pi^-\pi^0\pi^0\gamma$	17
D. Other ISR processes	19
E. Non-ISR background	20
F. Background subtraction in the mass region $0.6 < M_{3\pi} < 1.1 \text{ GeV}/c^2$	23
G. Background subtraction at $M_{3\pi} > 1.1 \text{ GeV}/c^2$.	26
H. Final state radiation	29
V. Detection efficiency	33
A. ISR photon inefficiency	34
B. π^0 efficiency and kinematic-fit χ^2 distribution	35
C. Efficiency correction due to the selection criteria	38
D. Efficiency correction due to track losses	39
E. Efficiency correction due to trigger and background filters	40
F. Model uncertainty	42
VI. Fit to the $\pi^+\pi^-\pi^0$ invariant mass distribution	42
VII. Measurement of the $e^+e^- \rightarrow \pi^+\pi^-\pi^0$ cross section below $1.1 \text{ GeV}/c^2$	52
VIII. Measurement of the $e^+e^- \rightarrow \pi^+\pi^-\pi^0$ cross section above $1.1 \text{ GeV}/c^2$	55
IX. The $e^+e^- \rightarrow \pi^+\pi^-\pi^0$ contribution to a_μ	58
X. Measurement of the $J/\psi \rightarrow \pi^+\pi^-\pi^0$ decay	60

XI. Summary	62
--------------------	----

References	62
-------------------	----

I. INTRODUCTION

The process $e^+e^- \rightarrow \pi^+\pi^-\pi^0$ has the second largest cross section after $e^+e^- \rightarrow \pi^+\pi^-$ in the energy region below 1 GeV and is therefore very important for the Standard Model calculation of the anomalous magnetic moment of muon $a_\mu \equiv (g-2)_\mu/2$. Currently the accuracy of the $e^+e^- \rightarrow \pi^+\pi^-\pi^0$ contribution to a_μ is about 3% [1] and needs to be improved.

The most precise measurements of the $e^+e^- \rightarrow \pi^+\pi^-\pi^0$ in the energy region of the ω and ϕ resonances were performed by the SND and CMD-2 detectors at the VEPP-2M e^+e^- collider [2–5]. Above the ϕ meson the latest measurements come from the BABAR experiment [6], which used the initial-state-radiation (ISR) technique, and the SND experiment at the VEPP-2000 e^+e^- collider [7]. There is also preliminary result of the BESIII experiment [8], which measured $e^+e^- \rightarrow \pi^+\pi^-\pi^0$ cross section in the energy range between 0.7 and 3.0 GeV using the ISR technique.

One of the reasons of the relatively low accuracy of $a_\mu^{3\pi}$ is the difference between the cross sections measurements in different experiments. For example, the SND cross section near the ω [3] is about 8% (1.8σ) larger than the cross section measured by CMD-2 [4]. BABAR did not measure the cross section in this region, but fitted to the 3π mass spectrum in the $e^+e^- \rightarrow \pi^+\pi^-\pi^0\gamma$ reaction with the vector-meson-dominance (VMD) model [6] and determined ω parameters. The BABAR value of the ω peak cross section as well as the BESIII preliminary result [8] support a larger cross-section value obtained by SND [3].

It is generally accepted that the process $e^+e^- \rightarrow \pi^+\pi^-\pi^0$ proceeds mainly through the $\rho(770)\pi$ intermediate state. This assumption has been well tested at the ω and ϕ resonances [9, 10]. The dynamics of the $e^+e^- \rightarrow \pi^+\pi^-\pi^0$ in the energy range between 1.1 and 2 GeV was recently studied in Ref. [7]. This study confirms the dominance of the $\rho(770)\pi$ mechanism below 1.5 GeV. However, in this region there is a 10–20% contribution from the isovector $\omega\pi^0$ mechanism and its interference with the dominant $\rho(770)\pi$ amplitude. In the region of the $\omega(1650)$ resonance (1.55–1.75 GeV) a large contribution of the $\rho(1450)\pi$ intermediate state was observed, which is comparable with that of the $\rho(770)\pi$. A relatively large fraction ($\sim 10\%$) of the $\rho(1450)\pi$ mechanism was also observed in the $J/\psi \rightarrow 3\pi$ decay [11].

In this article we update the BABAR $e^+e^- \rightarrow \pi^+\pi^-\pi^0$ measurement [6] using a five-times larger data set. We study the process $e^+e^- \rightarrow \pi^+\pi^-\pi^0\gamma$, where the photon emission is caused by initial state radiation. The Born cross section for this process integrated over

the momenta of the hadrons is given by

$$\frac{d\sigma(s, x, \theta)}{dx d\cos\theta} = W(s, x, \theta) \sigma_0(s(1-x)), \quad (1)$$

where \sqrt{s} is the e^+e^- center-of-mass (c.m.) energy, $x \equiv 2E_\gamma/\sqrt{s}$, E_γ and θ are the photon energy and polar angle in the c.m. frame, and σ_0 is the Born cross section for $e^+e^- \rightarrow \pi^+\pi^-\pi^0$. The so-called radiator function (see, for example, Ref. [12])

$$W(s, x, \theta) = \frac{\alpha}{\pi x} \left(\frac{2 - 2x + x^2}{\sin^2\theta} - \frac{x^2}{2} \right) \quad (2)$$

describes the probability of ISR photon emission for $\theta \gg m_e/\sqrt{s}$. Here α is the fine structure constant and m_e is the electron mass. The ISR photons are emitted predominantly at small angles relative to the initial electron or positron directions; however about 10% of the photons have c.m. polar angles in the range $30^\circ < \theta < 150^\circ$. In the present analysis, we require that the ISR photon is detected.

The goal of this analysis is to improve the accuracy of the $e^+e^- \rightarrow \pi^+\pi^-\pi^0$ cross section and the contribution of this process to the a_μ .

II. THE BABAR DETECTOR AND DATA SAMPLES

In this paper a data sample of 469 fb^{-1} , collected by the *BABAR* detector [13] at the PEP-II asymmetric-energy storage ring, is analyzed. At PEP-II, 9-GeV electrons collide with 3.1-GeV positrons at a center-of-mass energy of 10.58 GeV ($\Upsilon(4S)$ resonance). Most data were collected at the maximum of the $\Upsilon(4S)$. About 10% were recorded 40 MeV below the resonance.

Charged-particle tracking for the BABAR detector is provided by a five-layer silicon vertex tracker (SVT) and a 40-layer drift chamber (DCH), operating in a 1.5-T axial magnetic field. The transverse momentum resolution is 0.47% at 1 GeV/ c . Energies of photons and electrons are measured with a CsI(Tl) electromagnetic calorimeter (EMC) with a resolution of 3% at 1 GeV. Charged-particle identification is provided by measurement of ionization losses dE/dx in the SVT and DCH, and by an internally reflecting ring-imaging Cherenkov detector (DIRC). Muons are identified in the solenoid's instrumented flux return.

Signal and background ISR processes are simulated by a Monte Carlo (MC) event generator based on the approach suggested in Ref. [14]. A model of the $\rho(770)\pi$ intermediate

state is used to simulate the signal process $e^+e^- \rightarrow 3\pi\gamma$. The extra-photon radiation from the initial state is implemented with the structure function technique [15], while the final state radiation is simulated using the PHOTOS package [16]. Since the ISR photon is emitted predominantly at small angles relative to the beam directions, the events are generated with the restriction $20^\circ < \theta_\gamma^* < 160^\circ$, where θ_γ^* is the ISR photon polar angle in the c.m. frame. We also require that the invariant mass of the hadron system and ISR photon together is greater than $8 \text{ GeV}/c^2$. This condition restricts the maximum energy of extra photons emitted by the initial particles.

The following background ISR processes are simulated: $e^+e^- \rightarrow \pi^+\pi^-\gamma$, $\mu^+\mu^-\gamma$, $K_S K_L \gamma$, $K^+ K^- \pi^0 \gamma$, $\pi^+ \pi^- \pi^0 \pi^0 \gamma$, $\pi^+ \pi^- \eta \gamma$, $\omega \pi^0 \pi^0 \gamma$. The background from $e^+e^- \rightarrow q\bar{q}$ and $e^+e^- \rightarrow \tau^+\tau^-$ is simulated with JETSET [17] and KK2f [18] packages, respectively. The interaction of the generated particles with the *BABAR* detector and the detector response are simulated using the GEANT4 [19] package. The simulation takes into account the variation of the detector and accelerator conditions, and in particular describes the beam-induced background, which leads to the appearance of photons and tracks overlapping on the events of interest.

III. EVENT SELECTION

The selection of $e^+e^- \rightarrow \pi^+\pi^-\pi^0\gamma$ candidates is based on requirement that all the final particles are detected and well reconstructed. We select events with two good quality opposite-sign charged tracks and at least three photons. The tracks are required to have a transverse momentum above $100 \text{ MeV}/c$, and originate from the interaction region (within 2.5 cm of the collision axis and within 6 cm from the nominal collision point along the beam direction). Their polar angle must be between 23° and 140° . An event can contain any number of extra tracks not satisfying the above criteria.

The photons must have energies above 100 MeV and polar angles in the range $23^\circ < \theta < 137.5^\circ$. One of the photons (the ISR photon) is required to have a c.m. energy larger than 3 GeV. The remaining photons must form a π^0 candidate, a pair of photons with invariant mass in the range 0.1–0.17 GeV/c^2 .

Special conditions are imposed to suppress background from the process $e^+e^- \rightarrow e^+e^-\gamma$. At the preliminary selection stage the condition on the ratios of the calorimeter-deposited

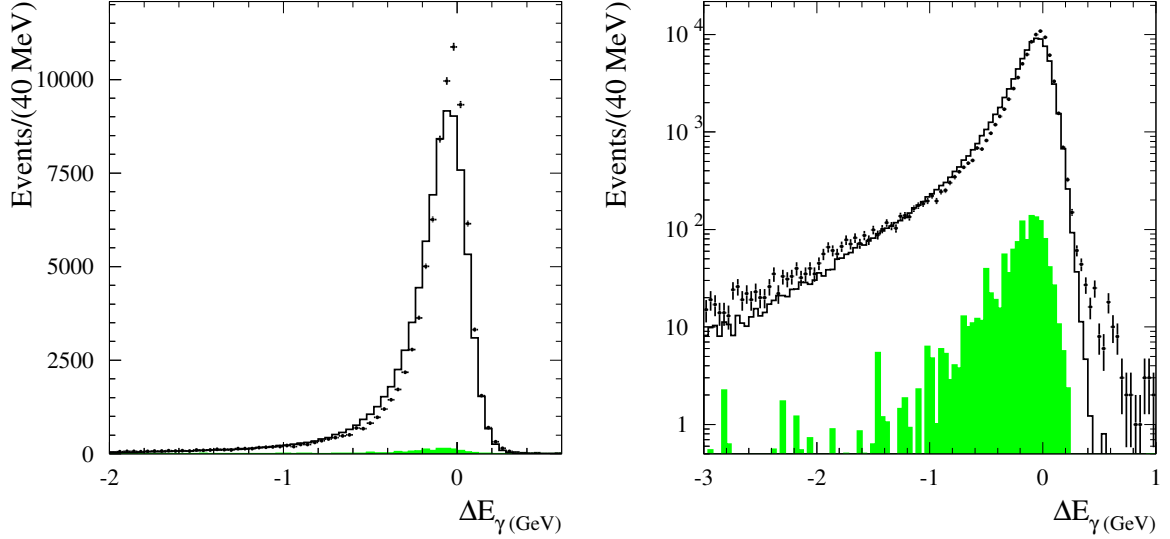


FIG. 1: Left panel: The distributions of the difference between the measured ISR photon energy and the energy obtained from the kinematic fit for data (points with error bars) and simulated (histogram) events from the ω mass region. The shaded histogram shows the distribution for simulated background events. Right panel: The same plot on a log scale.

energy to the track momentum for the two highest-momentum tracks is applied:

$$(E_{\text{cal},1}/p_1 - 1)^2 + (E_{\text{cal},2}/p_1 - 2)^2 < (0.35)^2. \quad (3)$$

The good quality charged track defined above must satisfy the condition

$$((E_{\text{cal}}/p - 1)/0.15)^2 + (((dE/dx)_{\text{DCH}} - 690)/150)^2 < 1. \quad (4)$$

For events satisfying the selection criteria described above, a kinematic fit is performed with requirements of energy and momentum conservation, and the π^0 mass constraint for the candidate π^0 . The MC simulation does not accurately reproduce the shape of the resolution function for the photon energy (see Fig. 1). To reduce effect of the data-MC simulation difference in the energy resolution, the fit uses only the measured direction for the ISR photon candidate; its energy is a free fit parameter. For events with two or more candidate π^0 s, all possible $\pi^+\pi^-\pi^0\gamma$ combinations are tested and the one with minimum χ^2 of the kinematic fit ($\chi^2_{3\pi\gamma}$) is used. As a result of the kinematic fit we obtain the corrected three-pion invariant mass ($M_{3\pi}$).

The $\chi^2_{3\pi\gamma}$ distribution for events from the 3π mass region near the ω mass (0.67–0.87 GeV/ c^2), where the contribution of background processes is small, is shown in Fig. 2. In

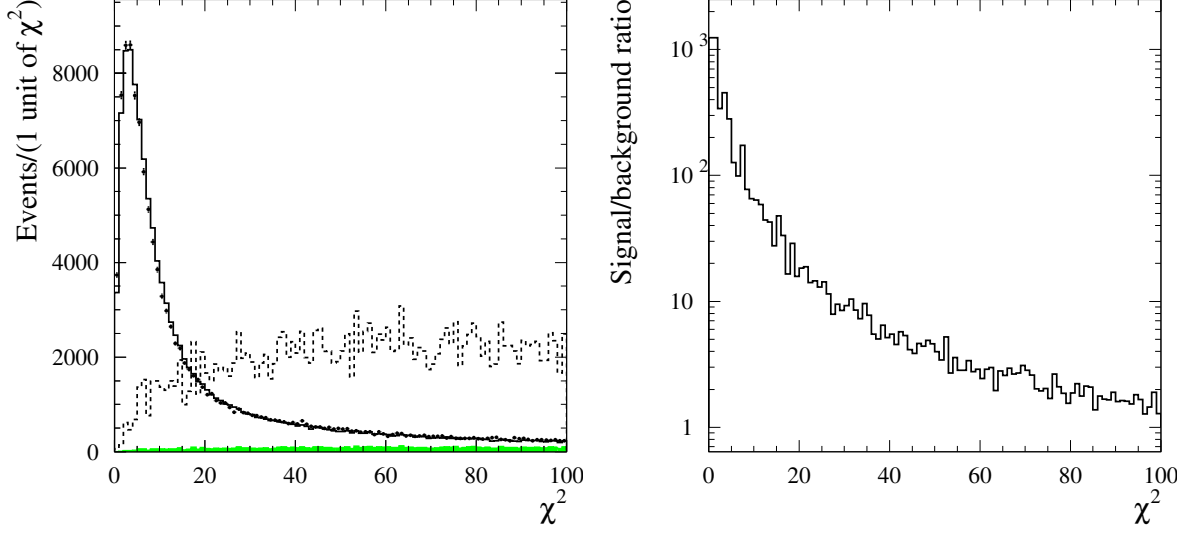


FIG. 2: Left panel: The $\chi^2_{3\pi\gamma}$ distributions for data (points with error bars) and simulated (histogram) events from the ω mass region. The shaded histogram shows the distribution for simulated background events. The dashed histogram is the background distribution multiplied by a factor of 25. Right panel: The ratio of the signal and background $\chi^2_{3\pi\gamma}$ distributions.

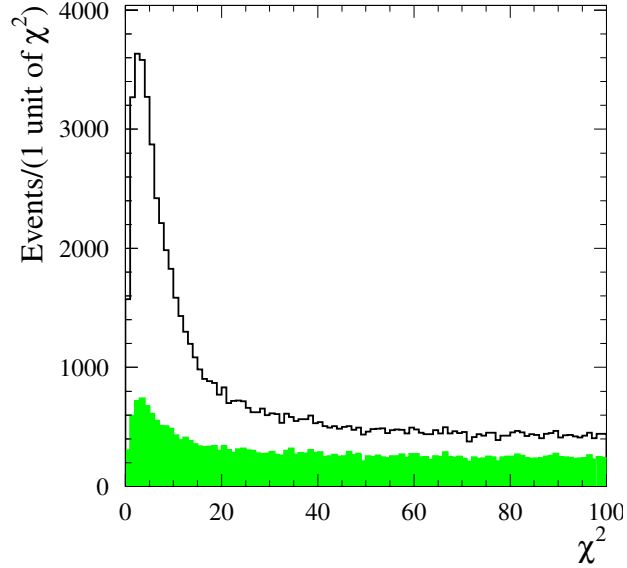


FIG. 3: The $\chi^2_{3\pi\gamma}$ distributions for data from the mass range $1.05 < M_{3\pi} < 3.00$ GeV/ c^2 . The shaded histogram shows events rejected by background suppression cuts.

TABLE I: Conditions applied to suppress background.

Condition	Description	Background processes to be suppressed
$N_K = 0$	number of charged tracks identified as kaons	$e^+e^- \rightarrow K^+K^-\pi^0\gamma$, $e^+e^- \rightarrow K^+K^-\gamma$, etc.
$N_e = 0$	number of charged tracks identified as electrons	$e^+e^- \rightarrow e^+e^-\gamma$
$E_{\pi^0} > 0.4 \text{ GeV}$	energy of the candidate π^0	$e^+e^- \rightarrow \pi^+\pi^-\gamma$, $e^+e^- \rightarrow \mu^+\mu^-\gamma$
$M_{\text{rec}}^2 < 5 \text{ GeV}^2/c^4$	mass recoiling against $\pi^+\pi^-$ pair	$e^+e^- \rightarrow \pi^+\pi^-\gamma$, $e^+e^- \rightarrow \pi^+\pi^-R$, where R is a light resonance (f_0, f_2, \dots) decaying to $2\pi^0$
$\chi_{4\pi\gamma}^2 < 30$	χ^2 of the kinematic fit to the $4\pi\gamma$ hypothesis	$e^+e^- \rightarrow \pi^+\pi^-\pi^0\pi^0\gamma$
$M_{\gamma\gamma}^*$ is outside the 0.10–0.17 GeV/c^2 range	invariant mass of two photons, one of which is the most energetic in an event	$e^+e^- \rightarrow q\bar{q}$
$M_{\pi\gamma} > 1.5 \text{ GeV}/c^2$	invariant mass of the most energetic photon and one of the charged pions	$e^+e^- \rightarrow \rho^\pm\pi^\mp\pi^0$, $e^+e^- \rightarrow \tau^+\tau^-$

further analysis we use two conditions on this parameter: the standard $\chi_{3\pi\gamma}^2 < 40$ and the tighter $\chi_{3\pi\gamma}^2 < 20$. The latter is applied for the $e^+e^- \rightarrow \pi^+\pi^-\pi^0$ cross section measurement. The $\chi_{3\pi\gamma}^2$ distribution for the mass range $1.05 < M_{3\pi} < 3.00 \text{ GeV}/c^2$ is shown in Fig. 3. In this region the background contribution is significantly larger.

The main sources of background for the process under study are the ISR processes $e^+e^- \rightarrow \pi^+\pi^-\pi^0\pi^0\gamma$, $\pi^+\pi^-\gamma$, $K^+K^-\pi^0\gamma$, etc., and non-ISR processes $e^+e^- \rightarrow q\bar{q}$, where $q = u, d, s$, and $e^+e^- \rightarrow \tau^+\tau^-$. Additional conditions are applied to suppress background. They are listed in Table I and discussed below.

Events with charged kaons in the final state ($e^+e^- \rightarrow K^+K^-\pi^0\gamma$, $e^+e^- \rightarrow K^+K^-\gamma$, etc.) are suppressed by the requirement that none of the charged tracks is identified as a kaon

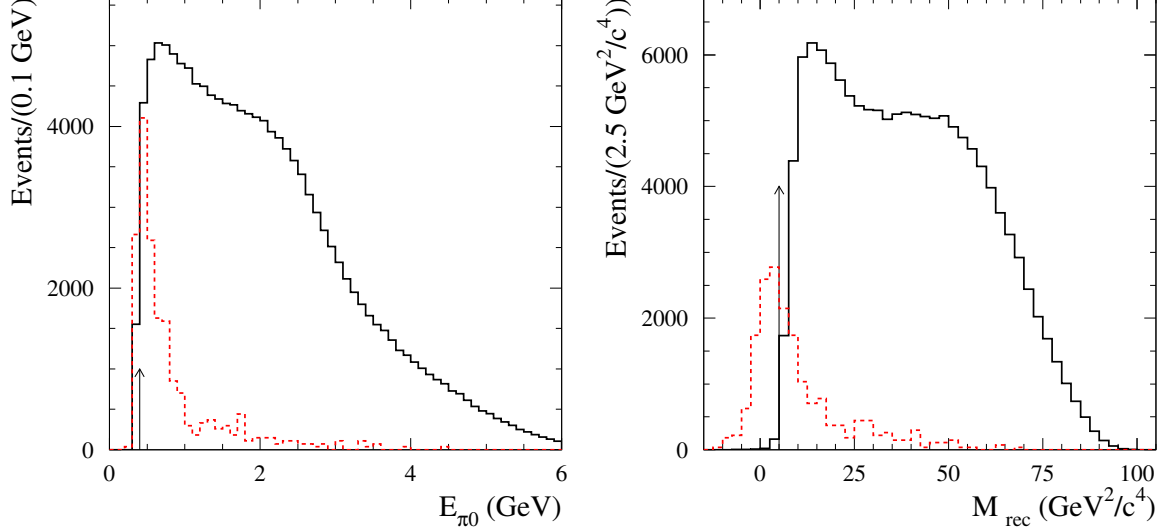


FIG. 4: Left panel: The E_{π^0} distribution for simulated signal and $e^+e^- \rightarrow \pi^+\pi^-\gamma$ background events with $\chi_{3\pi\gamma}^2 < 40$ from the region $M_{3\pi} < 1.1 \text{ GeV}/c^2$. The distributions are normalized to the integrated luminosity, but the $e^+e^- \rightarrow \pi^+\pi^-\gamma$ distribution is multiplied by a factor of 10. Right panel: The M_{rec}^2 distribution for simulated signal and $e^+e^- \rightarrow \pi^+\pi^-\gamma$ background events with $\chi_{3\pi\gamma}^2 < 40$ from the region $M_{3\pi} < 1.1 \text{ GeV}/c^2$. The distributions are normalized to the integrated luminosity, but the $e^+e^- \rightarrow \pi^+\pi^-\gamma$ distribution is multiplied by a factor of 10.

(with TightKMKaon selector). The remaining background from radiative Bhabha events is rejected by the requirement that none of the charged tracks is identified as an electron (with LooseKMElectronMicro selector).

Two-body ISR events from the processes $e^+e^- \rightarrow \pi^+\pi^-\gamma$ and $e^+e^- \rightarrow \mu^+\mu^-\gamma$ with extra spurious photons are suppressed by the two conditions: $E_{\pi^0} > 0.4 \text{ GeV}$, where E_{π^0} is the energy of the candidate π^0 , and $M_{\text{rec}}^2 < 5 \text{ GeV}^2/c^4$, where M_{rec} is the mass recoiling against $\pi^+\pi^-$ pair. The distributions of these parameters for signal events and background $e^+e^- \rightarrow \pi^+\pi^-\gamma$ events are shown in Fig. 4.

The process $e^+e^- \rightarrow \pi^+\pi^-\pi^0\pi^0\gamma$ is the main source of background for the process under study. Some fraction of background $4\pi\gamma$ events contain a π^0 among extra photons. For these events we perform a kinematic fit to the $4\pi\gamma$ hypothesis and reject events with $\chi_{4\pi\gamma}^2 < 30$. The $\chi_{4\pi\gamma}^2$ distribution for signal and $e^+e^- \rightarrow \pi^+\pi^-\pi^0\pi^0\gamma$ background events is shown in Fig. 5.

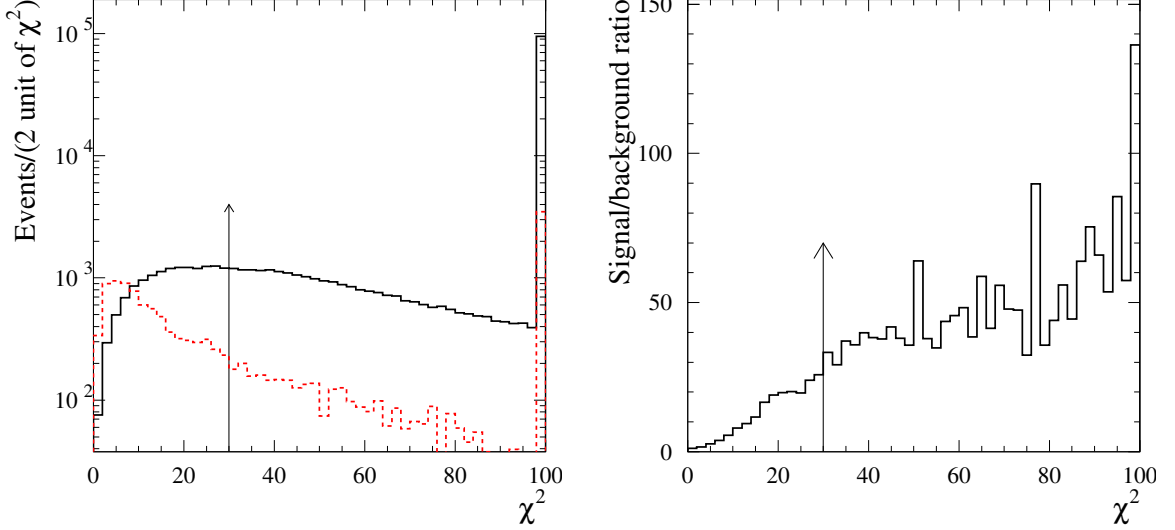


FIG. 5: Left panel: The $\chi^2_{4\pi\gamma}$ distribution for simulated signal and $e^+e^- \rightarrow \pi^+\pi^-\pi^0\pi^0\gamma$ background events with $\chi^2_{3\pi\gamma} < 40$ from the region $M_{3\pi} < 1.1 \text{ GeV}/c^2$. The distributions are normalized to the integrated luminosity, but the $e^+e^- \rightarrow \pi^+\pi^-\pi^0\pi^0\gamma$ distribution is multiplied by a factor of 5. Right panel: The ratio of the simulated signal and $e^+e^- \rightarrow \pi^+\pi^-\pi^0\pi^0\gamma$ $\chi^2_{4\pi\gamma}$ distributions.

Another important background source is $e^+e^- \rightarrow q\bar{q}$ events containing a very energetic π^0 in the final state. A fraction of these events is seen as a peak at the π^0 mass in the $M_{\gamma\gamma}^*$ distribution, where $M_{\gamma\gamma}^*$ is the invariant mass of two photons, one of which is the most energetic in an event. The second photon is required to have an energy above 100 MeV. Events with $0.10 < M_{\gamma\gamma}^* < 0.17 \text{ GeV}/c^2$ are rejected. The simulated $M_{\gamma\gamma}^*$ distribution for the two-photon combination with an invariant mass closest to the π^0 mass is shown in Fig. 6 (left) for signal and $e^+e^- \rightarrow q\bar{q}$ events. The same distributions but for the combination with the mass closest to the η mass are shown in Fig. 6 (right). The η -meson peak is also visible, but with a small amplitude. We don't use any conditions to remove $e^+e^- \rightarrow q\bar{q}$ events containing an η meson.

The $e^+e^- \rightarrow q\bar{q}$ background is dominated by $e^+e^- \rightarrow \pi^+\pi^-\pi^0\pi^0$ events. Events of this process passing the $\pi^+\pi^-\pi^0\gamma$ selection criteria have a $\chi^2_{3\pi\gamma}$ distribution peaked at low values, similar to the signal. A fraction of these events proceeding via $\rho^+\rho^-$ intermediate state is rejected by the condition $M_{\pi\gamma} > 1.5 \text{ GeV}/c^2$, where $M_{\pi\gamma}$ is the invariant mass of the most energetic photon and one of the charged pions. This condition also rejects $e^+e^- \rightarrow \tau^+\tau^-$

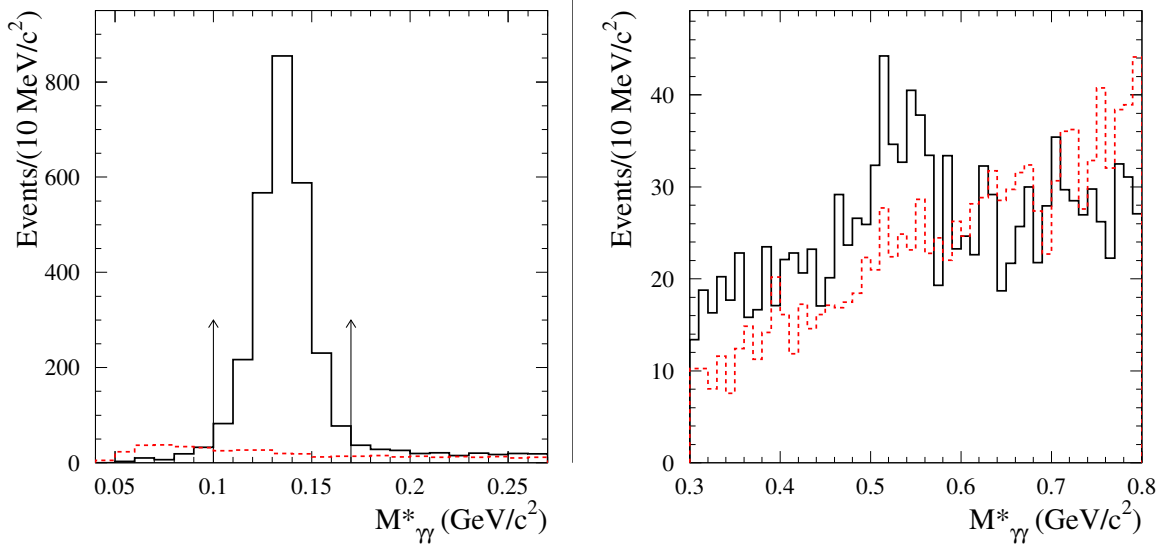


FIG. 6: Left panel: The $M_{\gamma\gamma}^*$ distribution for the two-photon combination with an invariant mass closest to the π^0 mass for simulated signal and $e^+e^- \rightarrow q\bar{q}$ events with $\chi_{3\pi\gamma}^2 < 40$ from the region $1.1 < M_{3\pi} < 3.5$ GeV/c^2 . The distributions are normalized to the integrated luminosity. Right panel: The same distributions but for the two-photon combination with the mass closest to the η mass.

events, which imitate $\pi^+\pi^-\pi^0\gamma$ events when both τ 's decay into $\rho\nu$. The $M_{\pi\gamma}$ distribution for simulated signal and $e^+e^- \rightarrow \tau^+\tau^-$ events from the region $2 < M_{3\pi} < 3.5$ GeV/c^2 is shown in Fig. 7 (left). The same distribution for data events is shown in Fig. 7 (right). The excess of events at low $M_{\pi\gamma}$ over the expected $e^+e^- \rightarrow \tau^+\tau^-$ distribution may be explained by the contribution of $e^+e^- \rightarrow \rho^+\rho^-$ events. It should be noted that the $e^+e^- \rightarrow \rho^+\rho^-$ events are absent in the $e^+e^- \rightarrow q\bar{q}$ simulation.

The effect of the background selection cuts is demonstrated in Tables II and III. The first represents the number of selected events in data and in simulation for different processes and the fraction of events with $\chi_{3\pi\gamma}^2 < 40$ passing the background suppression cuts. The second shows the fractions of signal and background events rejected by the background suppression cuts. It is seen that in the 3π mass region below 1.1 GeV/c^2 , most important for calculation of $a_\mu^{3\pi}$, the background suppression cuts decrease the fraction of background events by a factor of about 3, from 4.7% to 2.0%, with loss of signal events of 15%.

The $\chi_{3\pi\gamma}^2$ distribution for data events rejected by the background suppression cuts in the mass region $1.05 < M_{3\pi} < 3$ is shown as the shaded histogram in Fig. 3. In this region the

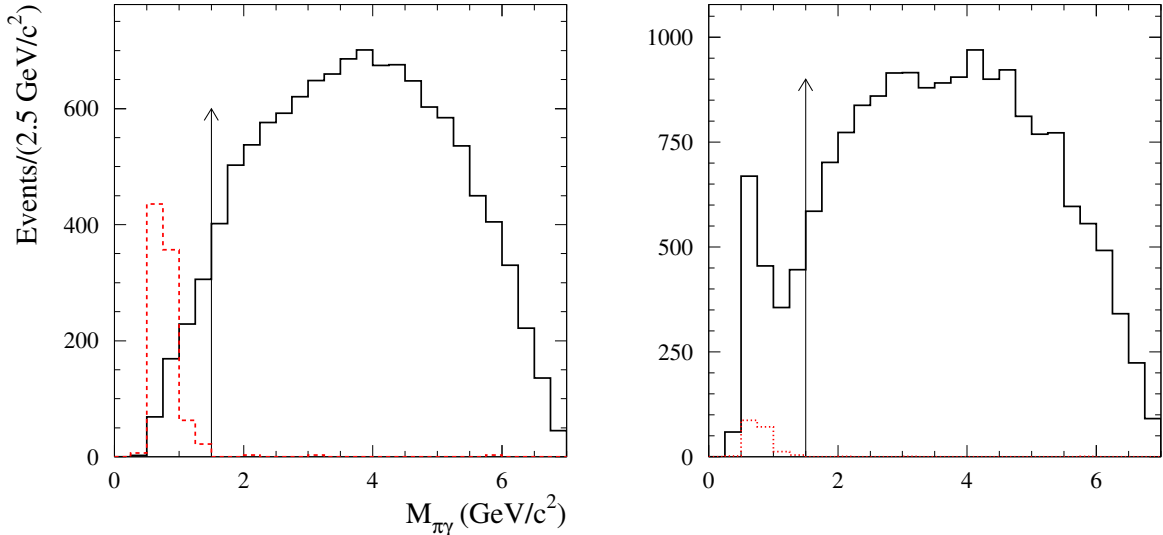


FIG. 7: Left panel: The $M_{\pi\gamma}$ distribution for simulated signal and $e^+e^- \rightarrow \tau^+\tau^-$ events with $\chi_{3\pi\gamma}^2 < 40$ from the region $2 < M_{3\pi} < 3.5$ GeV/c^2 . The distributions are normalized to the integrated luminosity, but the $e^+e^- \rightarrow \tau^+\tau^-$ distribution is multiplied by a factor of 5. Right panel: The $M_{\pi\gamma}$ distribution for data events with $\chi_{3\pi\gamma}^2 < 40$ from the region $2 < M_{3\pi} < 3.5$ GeV/c^2 . The dashed histogram represents the expected contribution of $e^+e^- \rightarrow \tau^+\tau^-$ events.

background is suppressed by a factor of 2.6 with loss of signal events of 17%.

IV. BACKGROUND ESTIMATION AND SUBTRACTION

A. $e^+e^- \rightarrow K^+K^-\pi^0\gamma$

The mass distribution for events with charged kaons survived our selection (we select events with both particles not identified as kaons) can be obtained from the distribution of events with two identified kaons: $N_{0K} = R_K N_{2K}$. The coefficient R_K is determined from $e^+e^- \rightarrow K^+K^-\pi^0\gamma$ simulation. To take into account difference between data and simulation in the charged-kaon identification efficiency, a control sample of kaons from the decay chain $D^{*+} \rightarrow \pi^+D^0$, $D^0 \rightarrow K^-\pi^+$ is used. The efficiency is determined as a function of the track momentum and polar angle. The ratio of the efficiencies obtained in data and simulation is then used to reweight simulated events. The correction for the coefficient R_K is found to vary from 16% at ω to 22% at 3 GeV/c^2 . The half of the correction is taken as an estimate of

TABLE II: In columns 2-5 for four $M_{3\pi}$ regions (in GeV/c^2) are shown: the number of selected events in data and simulation (the number of simulated events is normalized to 469 pb^{-1}), the fraction of events with $\chi^2_{3\pi\gamma} < 40$ satisfying the background suppression cuts (see Table I), and the scale factor used for normalization. The 1st column represents the list of simulated processes.

Process	0.6–1.1	1.1–2	2–3.05	3.15–3.5
Data	117195/0.83	29145/0.74	4772/0.51	636/0.40
$3\pi\gamma$	115267/0.85/5.9	24435/0.84/4.2	2807/0.78/2.0	185/0.70/3.0
total bkg.	2391/0.36	4854/0.44	2002/0.28	389/0.17
$4\pi\gamma$	1263/0.44/2.0	2590/0.48/1.6	410/0.40/0.84	26/0.28/0.65
$2\pi\gamma$	766/0.42/0.27	41/0.24/0.27	7/0.18/0.29	0
$4\pi q\bar{q}$	167/0.69/1.2	1956/0.62/2.6	1426/0.35/2.0	346/0.18/1.2
non- $4\pi q\bar{q}$	22/0.28/3.3	112/0.29/3.5	83/0.16/2.2	12/0.07/2.3
$K^+K^-\pi^0\gamma$	58/0.053/36	78/0.046/64	49/0.037/77	2/0.03/5
$K^+K^-\gamma$	72/0.15/2.2	13/0.15/2.2	0	0
$K_S K_L \gamma$	24/0.84/3.2	0	0	0
$K_S K^+ \pi^- \gamma$	9/0.11/3.0	29/0.13/3.4	12/0.19/7.0	0
$\mu^+\mu^-\gamma$	4/0.33/0.25	20/0.71/0.25	12/0.25/0.25	4/0.5/0.25
$2\pi\eta\gamma$	4/0.53/5.3	11/0.63/4.9	0	0
$\omega\pi^0\pi^0\gamma$	1/0.45/55	1/0.48/73	0	0
$\omega\eta\gamma$	1/0.44/15	1/0.74/5	0	0
$\tau^+\tau^-$	0	1/0.07/1.6	1/0.011/1.6	0

its systematic uncertainty. With this correction the R_K coefficients changes from 0.12 ± 0.01 at ω to 0.08 ± 0.01 at $3 \text{ GeV}/c^2$.

The estimated kaon background spectrum for the standard selection criteria is shown in Fig. 8 in comparison with the spectrum for simulated $e^+e^- \rightarrow K^+K^-\pi^0\gamma$ events. The $e^+e^- \rightarrow K^+K^-\pi^0\gamma$ simulation is reweighted to reproduce the $e^+e^- \rightarrow K^+K^-\pi^0$ and $e^+e^- \rightarrow \phi\pi^0$ data obtained in Ref. [20]. It is seen that the data spectrum in Fig. 8 is almost completely saturated by the $e^+e^- \rightarrow K^+K^-\pi^0\gamma$ events. The peak between 2.9 and 3.0 GeV/c^2 is due to $J/\psi \rightarrow K^+K^-\pi^0$ decay.

TABLE III: In columns 2-5 for four $M_{3\pi}$ regions (in GeV/c^2) are shown: the fractions (in %) of background and signal events with $\chi_{3\pi\gamma}^2 < 40$ rejected by the background suppression cuts (see Table I). The 1st column represents the list of the cuts.

Condition	0.6–1.1	1.1–2	2–3.05	3.15–3.5
$N_K = 0$	26/3	20/3	23/3	9/5
$E_{\pi^0} > 0.4 \text{ GeV}$	5/1	2/1	3/1	2/1
$M_{\text{rec}}^2 < 5 \text{ GeV}^2/c^4$	14/0	2/0	8/3	12/6
$\chi_{4\pi\gamma}^2 < 30$	30/10	32/11	23/11	23/13
$M_{\gamma\gamma}^*$ is outside the range 0.10–0.17 GeV/c^2	2/0	7/0	17/0	25/1
$M_{\pi\gamma} > 1.5 \text{ GeV}/c^2$	1/0	3/1	25/5	46/8
all cuts	64/15	56/16	72/22	83/30

The procedure described above does not work for the process $e^+e^- \rightarrow K^+K^-\gamma$. The simulation shows that only a small fraction of $e^+e^- \rightarrow K^+K^-\gamma$ events satisfying the selection criteria (with the exception of the kaon ID condition) contain two identified kaons. This may be due to the fact that one from the kaons decays into $\pi^+\pi^0$ inside the DCH. Therefore the $K^+K^-\gamma$ background is subtracted using MC simulation. The $e^+e^- \rightarrow K^+K^-\gamma$ simulation is normalized to the number of data events under the ϕ -meson peak in the K^+K^- invariant mass spectrum for events with one identified kaon.

B. $e^+e^- \rightarrow \pi^+\pi^-\gamma$

Figure 9 shows the distribution of events with $40 < \chi_{3\pi\gamma}^2 < 250$ and $M_{\text{rec}}^2 < 10 \text{ GeV}^2/c^4$. The latter condition suppresses contribution of all processes except $e^+e^- \rightarrow \pi^+\pi^-\gamma$. The spectrum is fitted by a sum of simulated signal and background distributions. The only free parameter of the fit is the scale factor for the $e^+e^- \rightarrow \pi^+\pi^-\gamma$ distributions. It is found to be 1.60 ± 0.2 . The quoted error is systematic. It is estimated by variation of the conditions on $\chi_{3\pi\gamma}^2$ and M_{rec}^2 . The large difference between fitted and expected numbers of $e^+e^- \rightarrow \pi^+\pi^-\gamma$ background events may be explained by inaccurate simulation of nuclear interaction of charged π mesons in the calorimeter. In particular, number of fake photons

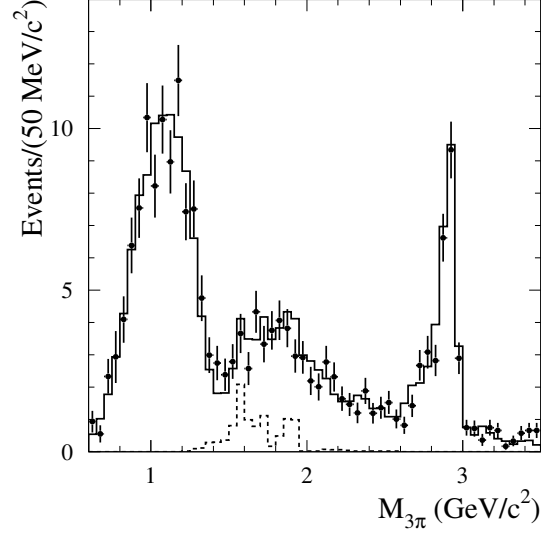


FIG. 8: The 3π mass spectrum for selected background events with two charged kaons (points with error bars). The solid histogram represents the distribution for simulated $e^+e^- \rightarrow K^+K^-\pi^0\gamma$ events. The dashed histogram shows the contribution of the $\phi\pi^0$ intermediate state.

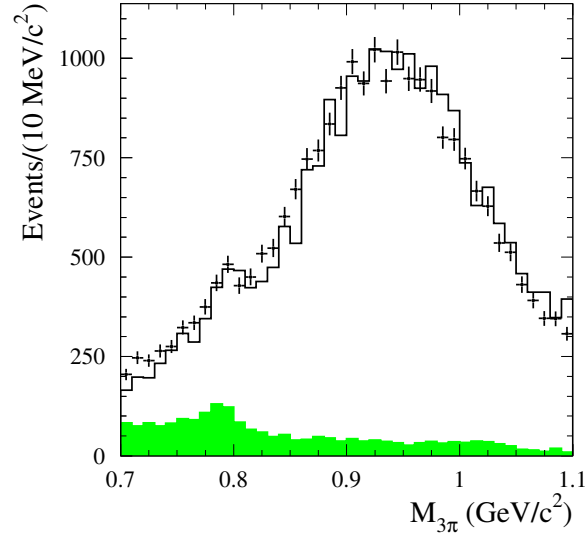


FIG. 9: The 3π invariant mass spectrum for data events with $40 < \chi_{3\pi\gamma}^2 < 250$ and $M_{\text{rec}}^2 < 10 \text{ GeV}^2/c^4$. The solid histogram represent the result of the fit with a sum of signal and background distributions. The difference between the solid and green histograms represents the $e^+e^- \rightarrow \pi^+\pi^-\gamma$ contribution.

due to nuclear interaction may be different in data and simulation.

The $e^+e^- \rightarrow \mu^+\mu^-\gamma$ background below $M_{3\pi} = 1.1 \text{ GeV}/c^2$ estimated using simulation is found to about 1/200 of the $e^+e^- \rightarrow \pi^+\pi^-\gamma$ background.

C. $e^+e^- \rightarrow \pi^+\pi^-\pi^0\pi^0\gamma$

The most important ISR background process is $e^+e^- \rightarrow \pi^+\pi^-\pi^0\pi^0\gamma$. The MC simulation is not quite correctly reproduce the 4π mass distribution for the $\pi^+\pi^-\pi^0\pi^0\gamma$ events. Therefore, we normalize the simulation to data. To do this we select events with two charged particle and at least five photons. One of the photons must have a c.m. energy larger than 3 GeV. Other photons must have energies higher than 50 MeV and form at least two candidate π^0 's with two-photon invariant mass in the range 0.085–0.185 GeV/ c^2 . For selected events a kinematic fit to the $e^+e^- \rightarrow \pi^+\pi^-\pi^0\pi^0\gamma$ hypothesis is performed. Events with $\chi_{4\pi\gamma}^2 < 30$ are selected. Background is suppressed by the conditions $\chi_{3\pi\gamma}^2 > 30$, $M_{\text{rec}}^2 < 5 \text{ GeV}^2/c^4$, $0.10 < M_{\gamma\gamma}^* < 0.17 \text{ GeV}/c^2$, $M_{\pi\gamma} > 1.5 \text{ GeV}/c^2$ and the requirement that none of the charged tracks is identified as a kaon. The remaining background is estimated from the sideband $30 < \chi_{4\pi\gamma}^2 < 60$ and subtracted. The number of signal events is calculated as $N_1 - \beta N_2$, where N_1 and N_2 are the numbers of events in the $\chi_{4\pi\gamma}^2$ signal and sidebands regions, respectively, and β is the N_1/N_2 ratio for background events. The β is estimated to be about 0.5 from $e^+e^- \rightarrow \pi^+\pi^-\pi^0\pi^0\pi^0\gamma$ simulation.

Several intermediate states ($\omega\pi^0$, $a_1\pi$, $\rho^+\rho^-$, etc.) contribute to the $e^+e^- \rightarrow \pi^+\pi^-\pi^0\pi^0\gamma$ process. The $\pi^+\pi^-\pi^0$ invariant mass spectrum for selected $e^+e^- \rightarrow \pi^+\pi^-\pi^0\pi^0\gamma$ events is shown in Fig. 10. A narrow peak at ω mass arising from the $\omega\pi^0$ intermediate state is clearly seen in the spectrum. Other intermediate states produce a wide $M_{3\pi}$ distribution with maximum near 1.1 GeV/ c^2 . We measure the 4π mass spectra separately for $\omega\pi$ and non- $\omega\pi$ events. These spectra are shown in Fig. 11. The $\omega\pi^0$ events are selected by the requirement that the invariant mass of one of two $\pi^+\pi^-\pi^0$ combinations is in the 0.767–0.8 GeV/ c^2 window.

To compensate the discrepancy between data and simulation seen in Fig. 11, we reweight $e^+e^- \rightarrow \pi^+\pi^-\pi^0\pi^0\gamma$ simulated events using the ratio of the data and simulated spectra as a weight function.

The accuracy of prediction of the $e^+e^- \rightarrow \pi^+\pi^-\pi^0\pi^0\gamma$ background is estimated from the

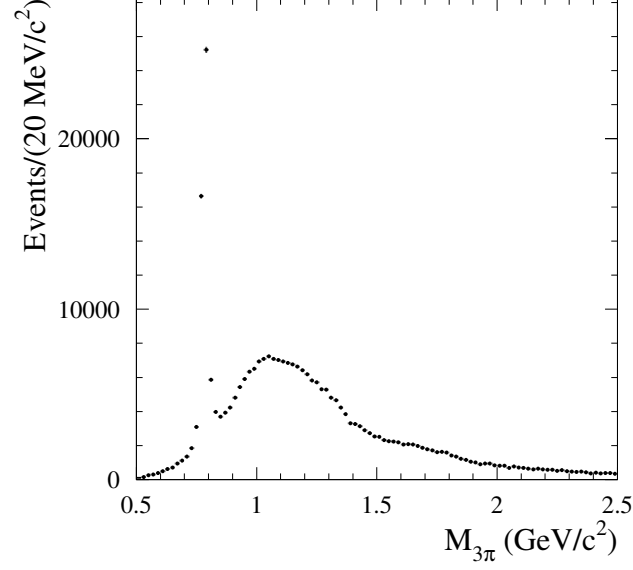


FIG. 10: The $\pi^+\pi^-\pi^0$ spectrum distributions for data from the mass range $1.05 < M_{3\pi} < 3.00$ GeV/c^2 . The shaded histogram shows events rejected by background suppression cuts.

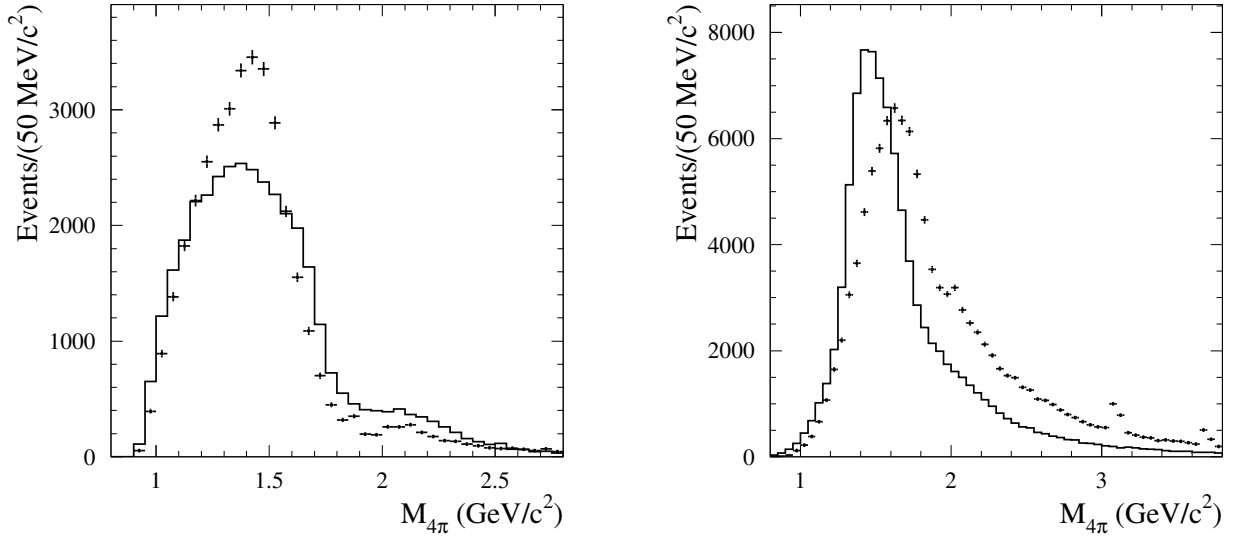


FIG. 11: The 4π invariant mass spectra for selected $e^+e^- \rightarrow \pi^+\pi^-\pi^0\pi^0\gamma$ data events (points with error bars) with the $\pi^+\pi^-\pi^0$ invariant mass in the $0.767\text{--}0.8$ GeV/c^2 window (left plot) and for events with both $\pi^+\pi^-\pi^0$ masses out of this window (right plot). The dashed histograms represent the same spectra for simulated $e^+e^- \rightarrow \pi^+\pi^-\pi^0\pi^0\gamma$ events.

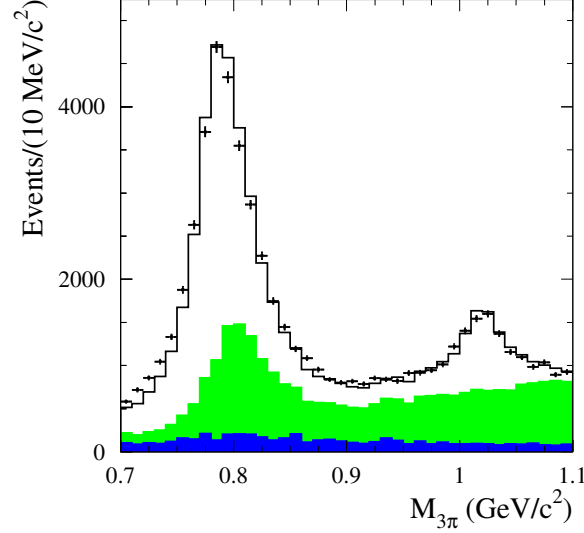


FIG. 12: The 3π invariant mass spectrum for data events with $50 < \chi_{3\pi\gamma}^2 < 500$ and $M_{\text{rec}}^2 > 10 \text{ GeV}^2/c^4$. The solid histogram represent the result of the fit with a sum of signal and background distributions. The green histogram is the spectrum for background processes. The difference between the green and blue histograms represents the $e^+e^- \rightarrow \pi^+\pi^-\pi^0\pi^0\gamma$ contribution.

study of the the 3π mass spectrum for predominantly background events with $50 < \chi_{3\pi\gamma}^2 < 500$. Such spectrum is shown in Fig. 12. To additionally suppress the $e^+e^- \rightarrow \pi^+\pi^-\gamma$ background, a tighter condition $M_{\text{rec}}^2 > 10 \text{ GeV}^2/c^4$ is used. The spectrum is fitted by a sum of simulated signal and background distributions. The following background processes are taken into account: $e^+e^- \rightarrow \pi^+\pi^-\gamma$, $e^+e^- \rightarrow \mu^+\mu^-\gamma$, $e^+e^- \rightarrow K^+K^-\pi^0\gamma$, $e^+e^- \rightarrow K_S K_L \gamma$, $e^+e^- \rightarrow K_S K^\pm \pi^\mp \gamma$, $e^+e^- \rightarrow \pi^+\pi^-\eta\gamma$, $e^+e^- \rightarrow \pi^+\pi^-\pi^0\pi^0\gamma$, $e^+e^- \rightarrow \tau^+\tau^-$, $e^+e^- \rightarrow q\bar{q}$. The normalization for these background processes is described below. The free fit parameters are scale factors for the $e^+e^- \rightarrow \pi^+\pi^-\pi^0\gamma$ and $e^+e^- \rightarrow \pi^+\pi^-\pi^0\pi^0\gamma$ distributions. The $\pi^+\pi^-\pi^0\pi^0\gamma$ scale factor is found to be 1.30 ± 0.15 . The quoted error is systematic. It is estimated by variation of the conditions on $\chi_{3\pi\gamma}^2$ and M_{rec}^2 .

D. Other ISR processes

We also study a contribution to the background from the following ISR processes with two charged particles in the final state: $e^+e^- \rightarrow K_S K_L \gamma$, $e^+e^- \rightarrow K_S K^\pm \pi^\mp \gamma$, $e^+e^- \rightarrow \pi^+\pi^-\eta\gamma$, $e^+e^- \rightarrow \omega\eta$, $e^+e^- \rightarrow \omega\pi^0\pi^0$. The hadron mass spectra for these processes are normalized

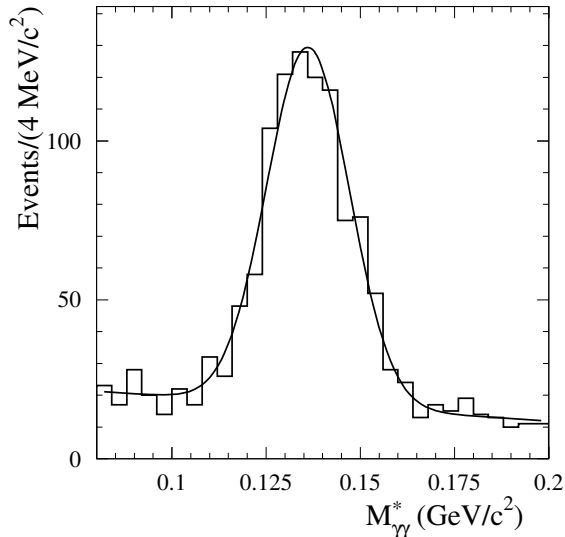


FIG. 13: The $M_{\gamma\gamma}^*$ distribution for data events from the region $0.6 < M_{3\pi} < 3.5 \text{ GeV}/c^2$ selected with our standard selection criteria except for the condition $0.10 < M_{\gamma\gamma}^* < 0.17 \text{ GeV}/c^2$. The curve is the result of the fit described in the text.

using the measured cross-sections for the corresponding non-radiative processes. The total contribution to the background from these processes at $M_{3\pi} < 1.1 \text{ GeV}$ is calculated to be less than $1/50$ of the $e^+e^- \rightarrow \pi^+\pi^-\pi^0\pi^0\gamma$ background.

E. Non-ISR background

The $e^+e^- \rightarrow q\bar{q}$ background events can be divided into two classes. The first class contains events from the $e^+e^- \rightarrow \pi^+\pi^-\pi^0\pi^0$ process, while the second contains events from all other processes. Events of the 4π class has $\chi_{3\pi\gamma}^2$ distribution peaked at small values similar to the signal process $e^+e^- \rightarrow \pi^+\pi^-\pi^0\gamma$.

To estimate the $e^+e^- \rightarrow q\bar{q}$ background we study the $M_{\gamma\gamma}^*$ distribution. This distribution for data events with $0.6 < M_{3\pi} < 3.5 \text{ GeV}/c^2$ selected using our standard selection criteria except for the condition on $M_{\gamma\gamma}^*$ is shown in Fig. 13. The events in the π^0 peak ($N_1^{q\bar{q}}$) originate mainly from the 4π class, while the flat distribution is dominated by $e^+e^- \rightarrow \pi^+\pi^-\pi^0\gamma$ events. The distribution is fitted by a sum of Gaussian and linear functions.

The ISR photon in the most non- 4π $q\bar{q}$ events is also imitated by the photon from the π^0 decay. Therefore the non- 4π background is also estimated from the number of events in the

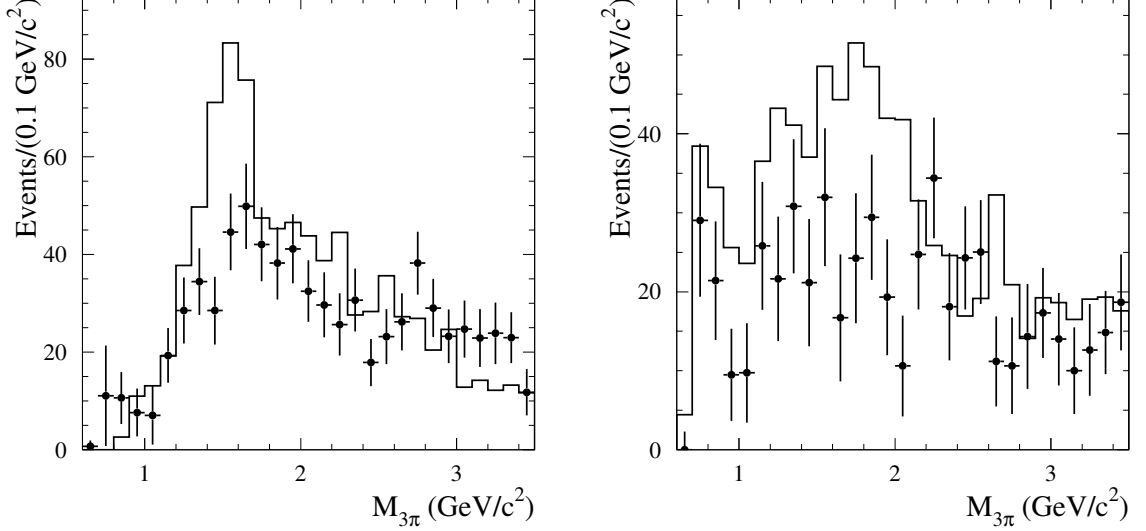


FIG. 14: The $M_{3\pi}$ spectra for data (points with error bars) and simulated (histogram) $e^+e^- \rightarrow q\bar{q}$ events. The numbers of 4π (left plot) and non- 4π (right plot) $q\bar{q}$ events are obtained from the fits to the $M_{\gamma\gamma}^*$ distributions as described in the text.

π^0 peak in the $M_{\gamma\gamma}^*$ distribution ($N_2^{q\bar{q}}$), but for events with $40 < \chi_{3\pi\gamma}^2 < 200$. The numbers of 4π ($N_{4\pi}$) and non- 4π ($N_{\text{non-}4\pi}$) $q\bar{q}$ events are calculated from the equations

$$\begin{aligned} N_1^{q\bar{q}} &= N_{4\pi} + bN_{\text{non-}4\pi}, \\ N_1^{q\bar{q}} &= aN_{4\pi} + N_{\text{non-}4\pi}, \end{aligned} \quad (5)$$

where the coefficients $a = 0.35 \pm 0.02$ and $b = 0.07 \pm 0.01$ are determined using $e^+e^- \rightarrow q\bar{q}$ simulation.

The 3π mass region $0.6\text{--}3.5 \text{ GeV}/c^2$ is divided into 29 intervals with $0.1 \text{ GeV}/c^2$ width. The procedure described above is performed in each $M_{3\pi}$ interval for data and simulated $e^+e^- \rightarrow q\bar{q}$ events. The Gaussian sigma and peak position in the fit are fixed at the values obtained from the fit to the total $M_{\gamma\gamma}^*$ spectrum shown in Fig. 13. The obtained $N_{4\pi}$ and $N_{\text{non-}4\pi}$ for data and simulation as a function of $M_{3\pi}$ are shown in Fig. 14.

It is seen that the $e^+e^- \rightarrow q\bar{q}$ simulation reproduce reasonably well the total number of selected $e^+e^- \rightarrow \pi^+\pi^-\pi^0\pi^0$ events. The overall scale factor for the simulation is 0.83 ± 0.05 . However the shapes of the $M_{3\pi}$ spectra for data and simulation are different, especially in the region $1.3\text{--}1.8 \text{ GeV}/c^2$. At $M_{3\pi} > 0.9 \text{ GeV}/c^2$ the ratio of the data and simulated spectra shown in Fig. 14 (left) is used to reweight the yield of simulated $e^+e^- \rightarrow \pi^+\pi^-\pi^0\pi^0$ events.

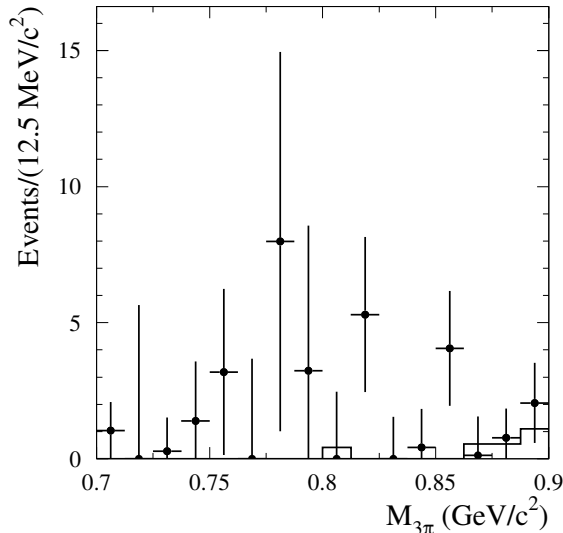


FIG. 15: The $M_{3\pi}$ spectrum for data (points with error bars) and simulated (histogram) $e^+e^- \rightarrow \pi^+\pi^-\pi^0\pi^0$ events with the finer binning.

It should be noted that the ratio of the number of 4π events selected with our standard criteria to the number of events shown in Fig. 14 (left) is about five. The uncertainty in the number of 4π background events obtained using the reweighted simulation is dominated by the uncertainty in the number of events in each mass bin in Fig. 14 (left).

An excess of data over simulation is seen in Fig. 14 (left) in the mass region 0.7–0.9 GeV/c^2 . This excess may be indication of a contribution of the $e^+e^- \rightarrow \omega\pi^0 \rightarrow \pi^+\pi^-\pi^0\pi^0$ process, which is absent in our $e^+e^- \rightarrow q\bar{q}$ simulation. This process produces events peaked at ω mass. We repeat the fitting procedure described above with finer binning. The result is shown in Fig. 15. This spectrum is used to estimate the $e^+e^- \rightarrow \pi^+\pi^-\pi^0\pi^0$ background in the $\pi^+\pi^-\pi^0$ mass region from 0.7 to 0.9 GeV/c^2 . To do this, the spectrum in Fig. 15 is multiplied by a scale factor of five, obtained using simulation at $M_{3\pi} > 0.9 \text{ GeV}$. The systematic uncertainty of this estimation is taken to be 100%. The same scale factor is used for the interval $0.6 < M_{3\pi} < 0.7 \text{ GeV}/c^2$, where the number of fitted 4π events in Fig. 14 (left) is 0.7 ± 1.2 .

In Fig. 14 (right) the $M_{3\pi}$ spectrum for non- 4π $q\bar{q}$ events having the peak in the $M_{\gamma\gamma}^*$ distribution at the π^0 mass. However, in some $q\bar{q}$ events the ISR photon is imitated by a photon from the $\eta \rightarrow \gamma\gamma$ decay. It should be noted that the $\chi_{3\pi\gamma}^2$ distribution for these events similar to the non- 4π $q\bar{q}$ events do not have a peak at low $\chi_{3\pi\gamma}^2$ values. To study

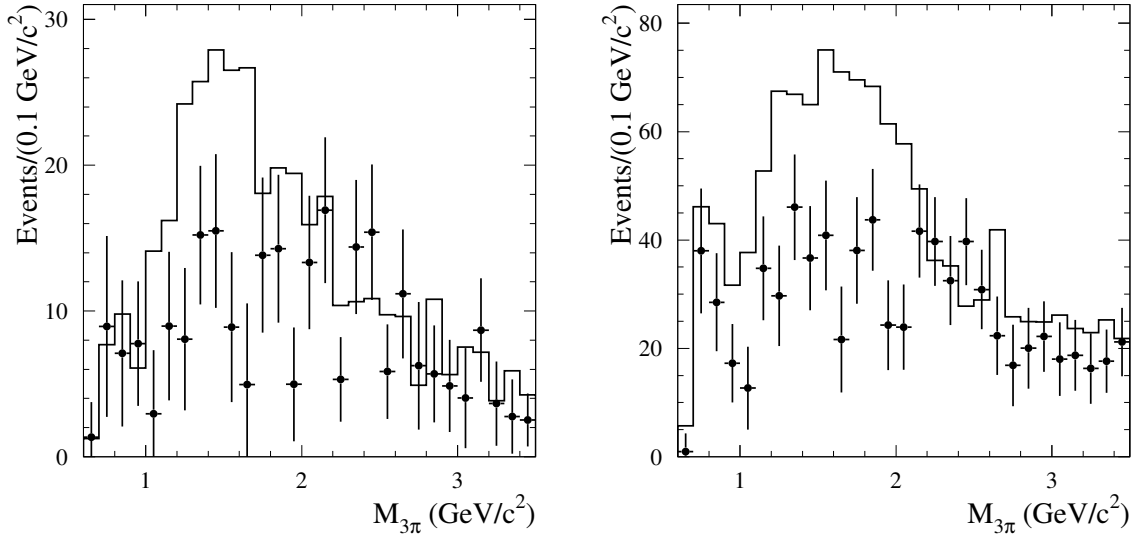


FIG. 16: Left panel: The fitted number of data (points with error bars) and simulated (histogram) $e^+e^- \rightarrow q\bar{q}$ events in the η -meson peak as a function of $M_{3\pi}$. Right panel: The sum of the distributions shown in Fig. 14 (right) and Fig. 16 (left).

this background source, we select events with $40 < \chi_{3\pi\gamma}^2 < 200$ and the standard conditions on all other parameters and fit to the $M_{\gamma\gamma}^*$ distribution for them near the η mass by a sum of Gaussian and linear functions. The fitted number of events in the η -meson peak as a function of $M_{3\pi}$ is shown in Fig. 16 (left). The number of events in this spectrum is about 1/3 of the number of events in Fig. 14 (right). The total spectrum for non- 4π $q\bar{q}$ [sum of Fig. 16 (left) and Fig. 14 (right)] is shown in Fig. 16 (right). The ratio of the data and simulated spectra is used to reweight the non- 4π $q\bar{q}$ simulation. The ratio of the number of non- 4π $q\bar{q}$ events selected with the standard criteria to the number of events shown in Fig. 16 (left) is about 0.4.

The $M_{3\pi}$ spectrum for the $q\bar{q}$ background events selected with the standard criteria is shown in Fig. 17. It is obtained using the $q\bar{q}$ simulation reweighted as described above. It is seen that fraction of non- 4π $q\bar{q}$ events is relatively small.

F. Background subtraction in the mass region $0.6 < M_{3\pi} < 1.1 \text{ GeV}/c^2$

The mass region $0.6 < M_{3\pi} < 1.1 \text{ GeV}/c^2$ is divided into 116 bins. The bin width varies from $2.5 \text{ MeV}/c^2$ near the peaks of the ω and ϕ resonances to $5 \text{ MeV}/c^2$ between

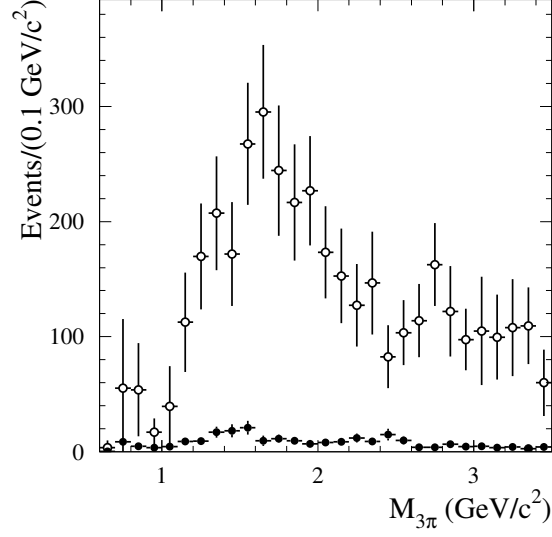


FIG. 17: The $M_{3\pi}$ spectrum for the $4\pi q\bar{q}$ (open circles) and non- $4\pi q\bar{q}$ (filled circles) background events selected with the standard criteria. The spectra are obtained using reweighted $q\bar{q}$ simulation.

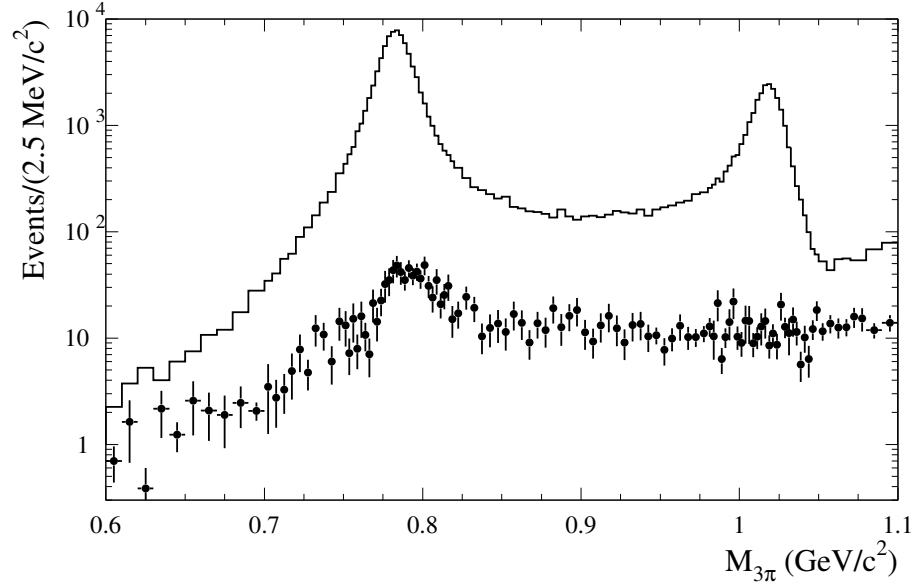


FIG. 18: The $M_{3\pi}$ spectrum for selected data events in the range from 0.6 to 1.1 GeV/c^2 (histogram). The points with error bars represent estimated background contribution.

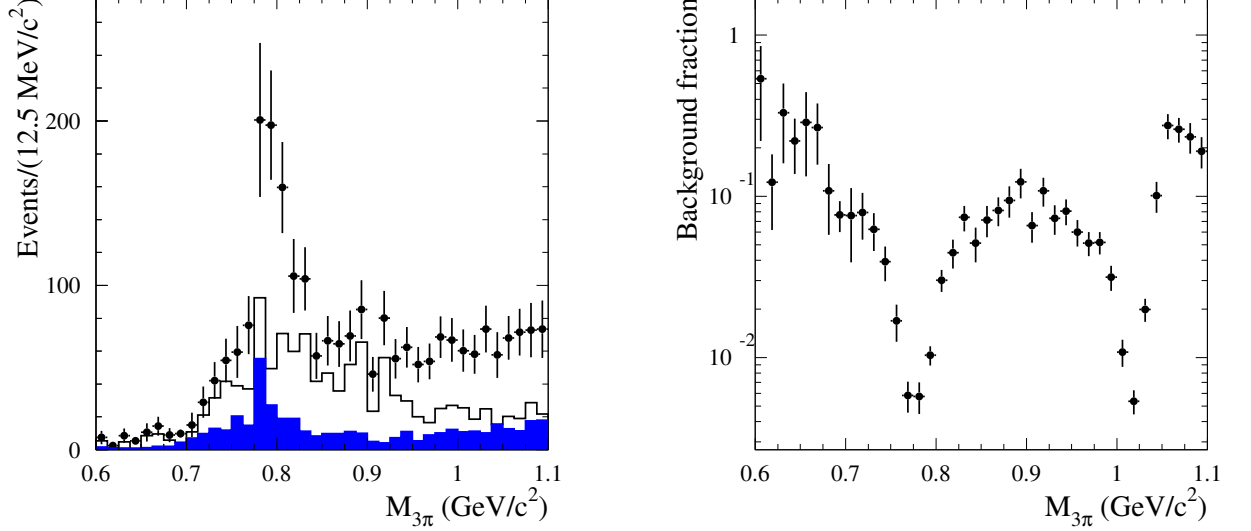


FIG. 19: Left panel: The $M_{3\pi}$ spectrum for background events (points with error bars). The filled histogram represents the contribution of all background sources except $e^+e^- \rightarrow \pi^+\pi^-\pi^0\pi^0\gamma$ and $e^+e^- \rightarrow \pi^+\pi^-\gamma$. The open histogram is a sum of the filled histogram and the spectrum for $e^+e^- \rightarrow \pi^+\pi^-\gamma$ events. Right panel: The ratio of the background spectrum to the spectrum for selected data events.

the resonances and 10 MeV/ c^2 near 0.6 and 1.1 GeV/ c^2 . The $M_{3\pi}$ spectrum for data events selected with the standard criteria is shown in Fig. 18. The points with error bars in Fig. 18 represent the total background contribution from the sources described above. The background $M_{3\pi}$ spectrum on a linear scale is displayed in Fig. 19 (left). The filled histogram represents the contribution of all background sources except $2\pi\gamma$ and $4\pi\gamma$. About two-thirds of events in this histogram come from the $e^+e^- \rightarrow \pi^+\pi^-\pi^0\pi^0$ process. The open histogram is a sum of the filled histogram and the $e^+e^- \rightarrow \pi^+\pi^-\gamma$ background spectrum. It is seen from Fig. 19 (left) that background in this $M_{3\pi}$ region is dominated by the processes $e^+e^- \rightarrow \pi^+\pi^-\pi^0\pi^0\gamma$ and $e^+e^- \rightarrow \pi^+\pi^-\gamma$.

The ratio of the background spectrum to the data spectrum is shown in Fig. 18 (right). The background fraction decreases from $(25 \pm 15)\%$ at 0.65 GeV/ c^2 to $(7 \pm 3)\%$ at 0.7 GeV/ c^2 and to $(0.5 \pm 0.1)\%$ in the ω region, then increases to $(9 \pm 2)\%$ at 0.9 GeV/ c^2 and decreases again to $(0.5 \pm 0.1)\%$ at the ϕ . Near 1.05 GeV/ c^2 , where the $e^+e^- \rightarrow \pi^+\pi^-\pi^0$ cross section has a minimum, the background fraction is $(27 \pm 5)\%$. With the tighter cut $\chi^2_{3\pi\gamma} < 20$ the background fraction decreases by a factor of about two.

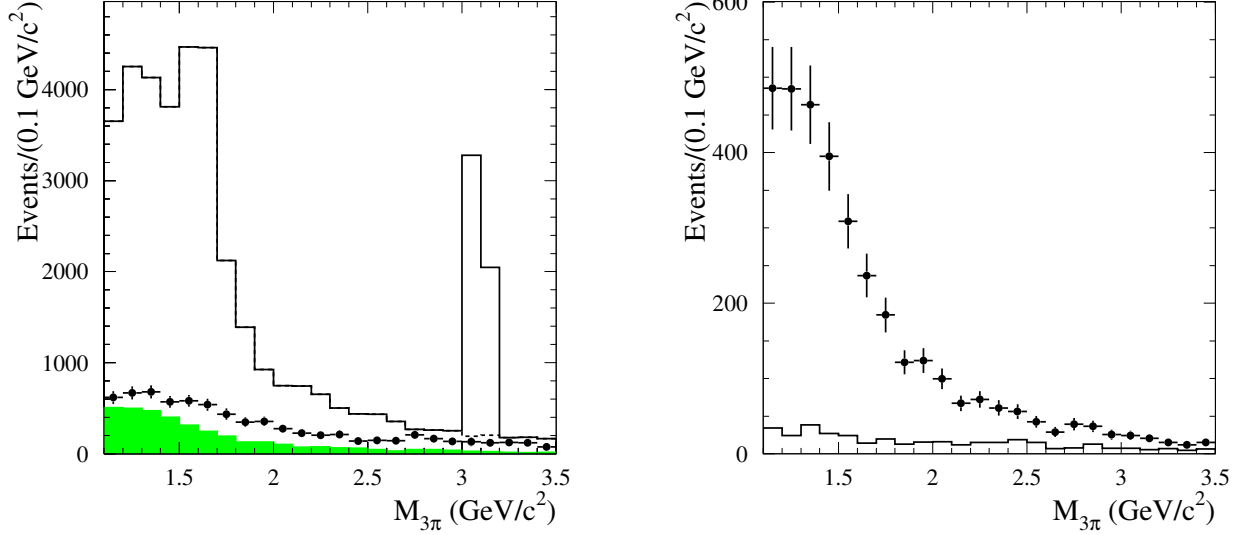


FIG. 20: Left panel: The $M_{3\pi}$ spectrum for selected data events with $1.1 < M_{3\pi} < 3.5 \text{ GeV}/c^2$ (histogram). The dashed histogram at $3.0 < M_{3\pi} < 3.2 \text{ GeV}/c^2$ represents the spectrum after subtraction of the J/ψ resonance contribution (see Sec. X). The points with error bars show the calculated spectrum for background events. The filled histogram represents the background spectrum with the $e^+e^- \rightarrow \pi^+\pi^-\pi^0\pi^0$ contribution subtracted. Right panel: The $M_{3\pi}$ spectrum for background events from all sources except $e^+e^- \rightarrow \pi^+\pi^-\pi^0\pi^0$ and $e^+e^- \rightarrow K^+K^-\pi^0\gamma$ (point with error bars). The histogram represents the same spectrum with the $e^+e^- \rightarrow \pi^+\pi^-\pi^0\pi^0\gamma$ contribution subtracted.

The estimated background is subtracted from the number of selected data events in each $M_{3\pi}$ bin. It should be noted that the numbers of background events in different mass bins are correlated. This correlation arises from the uncertainties of the scale factors for $e^+e^- \rightarrow \pi^+\pi^-\pi^0\pi^0\gamma$ and $e^+e^- \rightarrow \pi^+\pi^-\gamma$ events, which are equal to 10.5% and 12.5%, respectively.

G. Background subtraction at $M_{3\pi} > 1.1 \text{ GeV}/c^2$.

The $M_{3\pi}$ spectrum for selected data events with $1.1 < M_{3\pi} < 3.5 \text{ GeV}/c^2$ is shown in Fig. 20 (left). The points with error bars in Fig. 20 (left) represents the calculated spectrum for the background processes studied in previous sections, while the filled histogram shows the background spectrum with the $e^+e^- \rightarrow \pi^+\pi^-\pi^0\pi^0$ contribution subtracted. It is seen

that the process $e^+e^- \rightarrow \pi^+\pi^-\pi^0\pi^0$ becomes the largest source of background above 1.5 GeV/ c^2 . This background has $\chi_{3\pi\gamma}^2$ distribution similar to that for signal events. It is estimated from data (see Sec. IV E) and subtracted. The $e^+e^- \rightarrow K^+K^-\pi^0\gamma$ background is also estimated from data (see Secs. IV A). It is found to be relatively small, about 4% of the $e^+e^- \rightarrow \pi^+\pi^-\pi^0\pi^0$ contribution. Figure 20 (right) displays the calculated background from all other sources. Here the dominate contribution arises from the $e^+e^- \rightarrow \pi^+\pi^-\pi^0\pi^0\gamma$ process. The next largest contribution comes from non- 4π $q\bar{q}$ events. In the mass region $M_{3\pi} > 1.1$ GeV/ c^2 the background from ISR processes, even from $e^+e^- \rightarrow \pi^+\pi^-\pi^0\pi^0\gamma$, is estimated very roughly, because the MC event generator used does not include many intermediate states contributing to the ISR processes.

Therefore, we use the following procedure of background subtraction based on the difference in $\chi_{3\pi\gamma}^2$ distributions for signal and background events. For each mass bin the numbers of events with $\chi_{3\pi\gamma}^2 \leq 20$ (N_1) and $20 < \chi_{3\pi\gamma}^2 < 40$ (N_2) are determined. From these numbers we subtract background events of the $e^+e^- \rightarrow K^+K^-\pi^0\gamma$ and $e^+e^- \rightarrow \pi^+\pi^-\pi^0\pi^0$ processes:

$$\begin{aligned} N'_1 &= N_1 - \alpha_{4\pi}N_{4\pi} - \alpha_{KK\pi}N_{KK\pi}, \\ N'_2 &= N_2 - (1 - \alpha_{4\pi})N_{4\pi} - (1 - \alpha_{KK\pi})N_{KK\pi}, \end{aligned} \quad (6)$$

The numbers of signal (N_{sig}) and remaining background (N_{bkg}) events are then determined from the system of linear equations:

$$\begin{aligned} N'_1 &= \alpha_{sig}N_{sig} + \alpha_{bkg}N_{bkg}, \\ N'_2 &= (1 - \alpha_{sig})N_{sig} + (1 - \alpha_{bkg})N_{bkg}. \end{aligned} \quad (7)$$

The numbers $N_{KK\pi}$ and $N_{4\pi}$ are determined above in Secs. IV A and IV E. The coefficients $\alpha = N_1/(N_1 + N_2)$ for pure signal and background events are determined using simulation. The $M_{3\pi}$ dependence of the $\alpha_{4\pi}$ coefficient shown in Fig. 21 (left) is well described by a linear function, while the $\alpha_{KK\pi}$ is independent of $M_{3\pi}$ and is about 0.5.

The coefficient α_{sig} has a more complex mass dependence shown in Fig. 21 (right). The values of α_{sig} at the ϕ and J/ψ masses can be extracted from data. In the ϕ mass region we determine N_1 and N_2 for pure signal events by subtracting the calculated background from data events as described in Sec IV F. In the J/ψ mass region the same numbers are obtained using a fit to the $M_{3\pi}$ spectrum by a sum of a J/ψ line shape and a linear function (see Sec. X). The resulting values of α_{sig} are 0.859 ± 0.003 at the ϕ mass and 0.890 ± 0.005

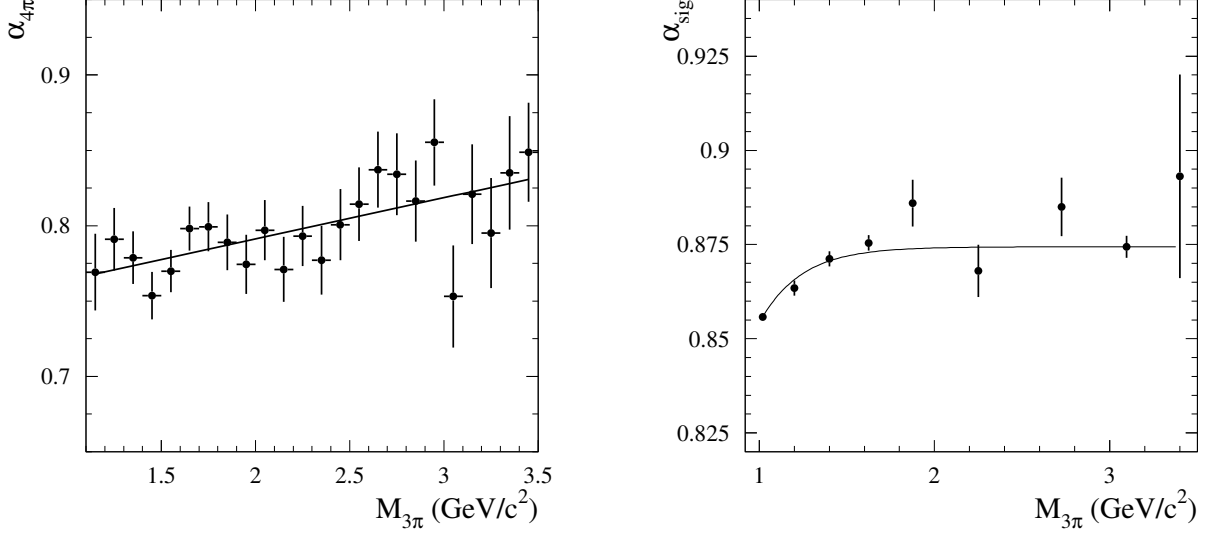


FIG. 21: Left panel: The $M_{3\pi}$ dependence of the $\alpha_{4\pi}$ coefficient fitted by a linear function. Right panel: The $M_{3\pi}$ dependence of the α_{sig} coefficient. The dependence is fitted by the function $y = p_1[1 - p_2 \exp(-p_3 M_{3\pi})]$, in which two parameters p_i are determined from the relations $y(m_\phi) = \alpha_{sig}(m_\phi)$ and $y(m_{J/\psi}) = \alpha_{sig}(m_{J/\psi})$.

at the J/ψ mass. Their ratios to the corresponding values obtained from simulation are $R_\phi = 1.004 \pm 0.004$ and $R_{J/\psi} = 1.018 \pm 0.007$, respectively. In Eqs. (7) we use for α_{sig} the fitting function shown in Fig. 21 (right) multiplied by a linear function interpolating between R_ϕ and $R_{J/\psi}$.

The $M_{3\pi}$ dependence of the α_{bkg} coefficient is shown in Fig. 22 (left). It is obtained using a mixture of background simulated events shown in Fig. 20 (right). The contribution of the $e^+e^- \rightarrow \pi^+\pi^-\pi^0\pi^0\gamma$ process dominates in this mixture. It decreases from about 90% in the range 1.1–1.5 GeV/c^2 to about 60% near 3.5 GeV/c^2 . However, the value of the α_{bkg} coefficient remains constant. Its average value over the range $1.1 < M_{3\pi} < 3.5 \text{ GeV}/c^2$ is 0.316 ± 0.007 . This is due to a relatively small difference between α_{bkg} values for different processes. For example, the α_{bkg} value is 0.31 ± 0.01 for $e^+e^- \rightarrow \pi^+\pi^-\pi^0\pi^0\gamma$ and 0.37 ± 0.02 for non $4\pi q\bar{q}$. To estimate the systematic uncertainty of the α_{bkg} , we vary the fraction non- $\pi^+\pi^-\pi^0\pi^0\gamma$ events in the mixture of simulated background events by a factor of two. The variation of the α_{bkg} value is taken as a measure of the systematic uncertainty. It is less than 5% below 2 GeV/c^2 , 8% between 2 and 3 GeV/c^2 , and 15% above 3 GeV/c^2 .

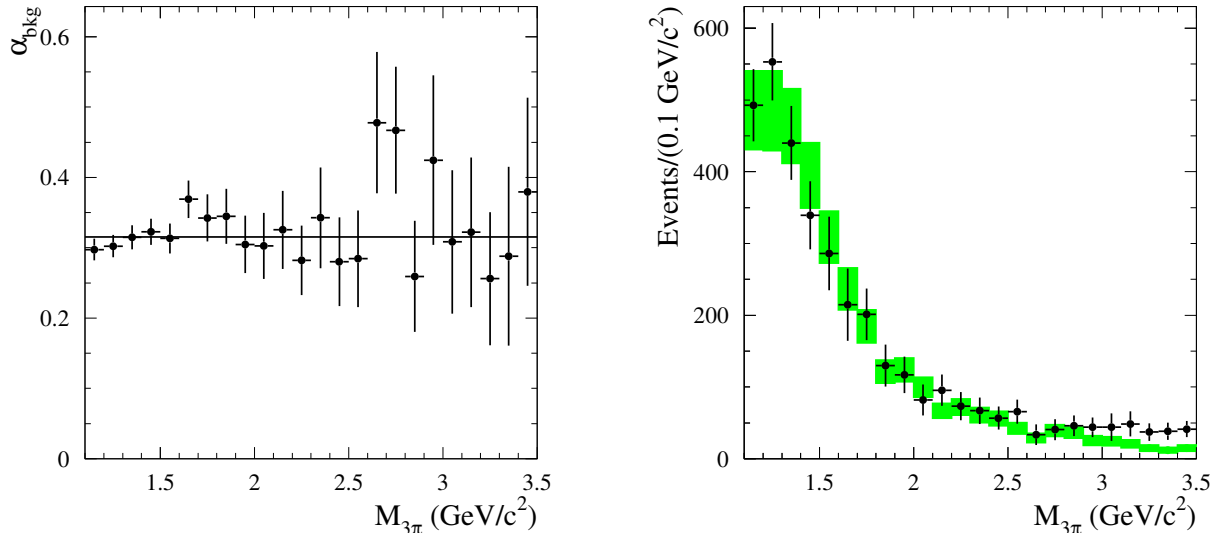


FIG. 22: Left panel: The $M_{3\pi}$ dependence of the α_{bkg} coefficient fitted by a constant. Right panel: The $M_{3\pi}$ spectrum for background events obtained by the solution of the system of equations (7) (point with error bars) compared with the spectrum obtained using simulation (filled rectangles).

The $M_{3\pi}$ spectrum for background events obtained by the solution of the system of equations (7) is shown Fig. 22 (right) in comparison with the same spectrum obtained using simulation. It is seen that the simulation reproduce the data spectrum reasonably well up to 3 GeV. The $M_{3\pi}$ spectrum for signal events is shown in Fig. 23.

H. Final state radiation

A high-energy photon can be also emitted from the final state. Since the 3π system in the ISR and final-state-radiation (FSR) processes has different C -parity, the contribution of the interference between them to the total cross section vanishes when integrating over the final hadron momenta.

We analyze two FSR mechanisms. The first is emission of the photon by charged pions. Its cross section is calculated as $\sigma_{3\pi}(10.58 \text{ GeV})f_{FSR}$, where f_{FSR} is the FSR probability. The $e^+e^- \rightarrow \pi^+\pi^-\pi^0$ cross section at 10.58 GeV can be estimated from the CLEO measurement at 3.67 GeV $\sigma_{3\pi}(3.67 \text{ GeV}) = (13.1_{-1.7}^{+1.0} \pm 2.1) \text{ pb}$ [21]. Perturbative QCD predicts the same asymptotic energy dependence $1/E^8$ for all vector-pseudoscalar ($e^+e^- \rightarrow VP$) cross sections [22, 23]. This dependence can be tested experimentally using the CLEO [21] and

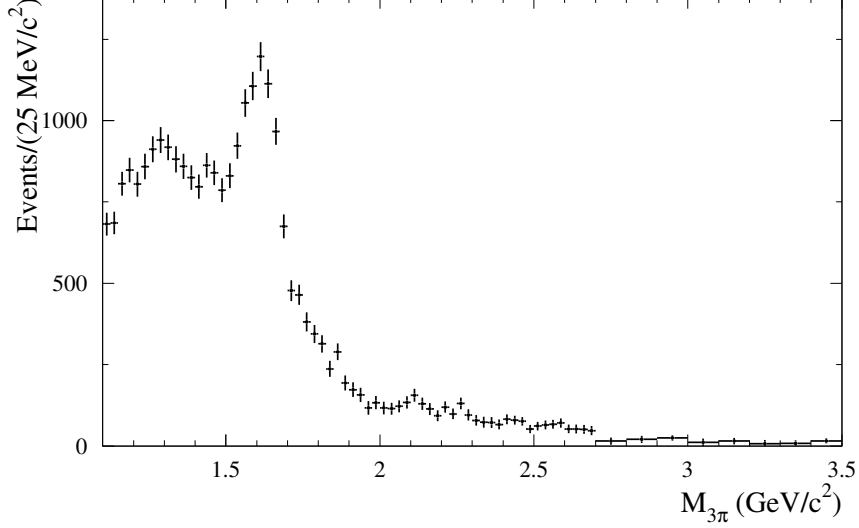


FIG. 23: The $M_{3\pi}$ spectrum for signal data events obtained by the solution of the system of equations (7).

Belle [24, 25] results on $e^+e^- \rightarrow VP$ cross sections at 3.67 GeV and 10.58 GeV, respectively. For the most accurately measured cross sections for $e^+e^- \rightarrow \rho\eta$, $\omega\pi^0$, and K^*K , the ratio $\sigma(3.67 \text{ GeV})/\sigma(10.58 \text{ GeV}) \approx 3000$, which corresponds to the dependence $1/E^{7.6}$. With this dependence $\sigma_{3\pi}(10.58 \text{ GeV})$ is expected to be about 4.4 fb.

The mass region under study $M_{3\pi} < 3.5 \text{ GeV}/c^2$ corresponds to the FSR photon c.m. energy $E_\gamma^* > 4.7 \text{ GeV}$. Such a photon can be radiated only by the most energetic pion in the $e^+e^- \rightarrow \pi^+\pi^-\pi^0$ process. For the dominant mechanism $e^+e^- \rightarrow \rho(770)\pi \rightarrow \pi^+\pi^-\pi^0$, the c.m. energy of the most energetic pion is 5.26 GeV. To estimate the FSR probability, we use the formula for the FSR $e^+e^- \rightarrow \pi^+\pi^-\gamma$ cross section from Ref. [26] obtained for point-like pions. The FSR probability for $\pi^+\pi^-$ final state at 10.52 GeV ($f_{2\pi}(E_\gamma^* > 4.7 \text{ GeV}) = 0.26\alpha/\pi$) must be multiplied by a factor of 1/3 (only the most energetic pion in the 3π final state can emit such a photon and this pion must be charged). Thus, the FSR contribution to the $e^+e^- \rightarrow \pi^+\pi^-\pi^0\gamma$ cross section in the assumption that the photon is emitted by charged pions is estimated to be about 0.001 fb and is negligible.

The second FSR mechanism is photon emission from the quarks, which then hadronize into $\pi^+\pi^-\pi^0$. In the 3π mass region under study this process is expected to be dominated by production of resonances decaying to $\pi^+\pi^-\pi^0$, e.g. the processes $e^+e^- \rightarrow \eta\gamma$, $a_1(1260)\gamma$, $a_2(1320)\gamma$, $\pi(1300)\gamma$.

The process $e^+e^- \rightarrow \eta\gamma$ has a 3π invariant mass well below the mass range under study. This process and the process $e^+e^- \rightarrow \eta'\gamma$ were studied by BABAR in Ref. [27]. The measured $e^+e^- \rightarrow \eta\gamma$ and $e^+e^- \rightarrow \eta'\gamma$ cross sections are $4.5_{-1.1}^{+1.2} \pm 0.3$ fb and $5.4 \pm 0.8 \pm 0.3$ fb, respectively. In Ref. [27] they are compared with the pQCD prediction obtained with asymptotic η and η' distribution amplitudes, 2.2 fb and 5.5 fb, respectively.

The cross section for the processes $e^+e^- \rightarrow a_1(1260)\gamma$, $a_2(1320)\gamma$ at large c.m. energy is given by [28]

$$\frac{\sigma(e^+e^- \rightarrow M\gamma)}{d\cos\theta} = \frac{\pi^2\alpha^3}{4}|F_{M\gamma\gamma}|^2(1 + \cos^2\theta), \quad (8)$$

where $F_{M\gamma\gamma}$ is a meson-photon transition form factor for the helicity-zero state, which dominates at large momentum transfers,

$$q^2|F_{M\gamma\gamma}| = \frac{1}{3}\frac{|f_M|}{\sqrt{2}}I_M, \quad (9)$$

where I_M is an integral depending on shape of the meson distribution amplitude. For asymptotic distribution amplitude $I_{a_1} = 6$ and $I_{a_2} = 10$. With the meson decay constants, $f_{a_1} \approx 200$ MeV [29], and $f_{a_2} \approx f_{f_2} \approx 110$ MeV [30], the cross section for the processes $e^+e^- \rightarrow a_1(1260)\gamma$ and $a_2(1320)\gamma$ are estimated to be 6.4 fb and 5.4 fb, respectively. There are no experimental data on these cross sections. There is, however, measurements of the $e^+e^- \rightarrow f_2(1260)\gamma$ cross section at 10.58 GeV performed by BABAR [31]: (37_{-18}^{+24}) fb, which is in reasonable agreement with the prediction $\sigma_{f_2\gamma} \approx (25/9)\sigma_{a_2\gamma} \approx 15$ fb. The radiative process with excited pion $e^+e^- \rightarrow \pi(1300)\gamma$ is expected to be small due to suppression the $\pi(1300)$ leptonic decay constant [32].

The next group of C -even resonances decaying to $\pi^+\pi^-\pi^0$ is located near 1.7 GeV. It consists of the radial excitations of a_1 and a_2 mesons, $a_1(1640)$ and $a_2(1700)$, and the D -wave $q\bar{q}$ state $\pi_2(1670)$. We do not expect significant decrease of the leptonic decay constants for radially excited P -wave $q\bar{q}$ states compared with the ground states. However, due to larger masses their branching fractions to $\pi^+\pi^-\pi^0$ must be lower. The theoretical predictions for them are about 30–50% [33, 34]. For a_2 family we can assume that $f_{a_2(1700)}^2/f_{a_2(1320)}^2 \sim \Gamma(a_2(1700) \rightarrow \gamma\gamma)/\Gamma(a_2(1320) \rightarrow \gamma\gamma)$ and use the measurements of the products $\Gamma(a_2(1320) \rightarrow \gamma\gamma)B(a_2(1320) \rightarrow \pi^+\pi^-\pi^0) = 0.65 \pm 0.02 \pm 0.02$ keV, and $\Gamma(a_2(1700) \rightarrow \gamma\gamma)B(a_2(1700) \rightarrow \pi^+\pi^-\pi^0) = 0.37 \pm 0.10 \pm 0.10$ keV [35] to obtain that $f_{a_2(1700)}^2B(a_2(1700) \rightarrow \pi^+\pi^-\pi^0) \approx 0.4f_{a_2(1320)}^2$. The same relation is used to estimate the

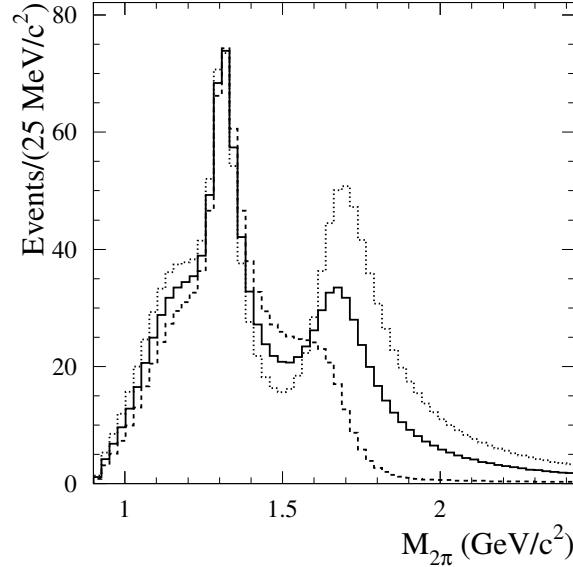


FIG. 24: The expected $M_{3\pi}$ spectrum from the FSR processes $e^+e^- \rightarrow M\gamma \rightarrow \pi^+\pi^-\pi^0\gamma$, where $M = a_1(1260)\gamma$, $a_2(1320)\gamma$, $a_1(1640)$, and $a_2(1700)$. The solid histogram represents the incoherent sum of the processes. The dotted (dashed) histogram demonstrate effect of constructive (destructive) interference between the $a_1(1260)$ and $a_1(1640)$ amplitudes, and $a_2(1320)$ and $a_2(1700)$ amplitudes.

$e^+e^- \rightarrow a_1(1640)\gamma$ cross section. The $\pi_2(1670)$ two-photon width is found to be low compared with $\Gamma(a_2(1320) \rightarrow \gamma\gamma)$ [35]. So, we neglect the contribution of the $e^+e^- \rightarrow \pi_2(1670)\gamma$ process.

To estimate the detection efficiency for the FSR processes we assume that the efficiency is weakly dependent on 3π internal structure and reweight simulated ISR $e^+e^- \rightarrow 3\pi\gamma$ events to reproduce the photon angular distribution given by Eq. (8). The obtained detection efficiency at $a_2(1320)$ mass is 17.9% for the standard selection criteria. The 3π mass distribution for the $e^+e^- \rightarrow M\gamma$ process has a resonance shape. The expected mass spectrum for the FSR processes calculated as a sum of the $a_1(1260)$, $a_2(1320)$, $a_1(1640)$, and $a_2(1700)$ Breit-Wigner functions is shown in Fig. 24 by the solid histogram. Interference between amplitudes of different resonances may strongly modify this spectrum. The effect of interference is demonstrated in Fig. 24. We take into account the interference between the $a_1(1260)$ and $a_1(1640)$ amplitudes, and $a_2(1320)$ and $a_2(1700)$ amplitudes, but neglect the interference between a_1 and a_2 states. The dotted (dashed) histogram represents the

result for relative phases between resonances equal to 0 (π). We subtract the spectrum without interference from the spectra for selected data events shown in Figs. 18 and 23. The systematic uncertainty of the FSR contribution, which takes into account the uncertainty of the theoretical prediction and the effect of interference, is estimated to be 100%. The fraction of the FSR background is maximal (7–8%) in the region 1.05–1.08 GeV/ c^2 , where the measured $M_{3\pi}$ spectrum has a minimum, and near $M_{3\pi} = 1.32$ GeV/ c^2 . Near 1.7 GeV/ c^2 the background fraction is about 6%.

In the mass region near 2 GeV/ c^2 there are several poorly established excited a_1 and a_2 states [40]. We model their contribution by a sum of the $a_1(1930)$ and $a_2(2030)$ resonances assuming that $f_{a_1(1930)}2B(a_1(1930) \rightarrow \pi^+\pi^-\pi^0) \approx 0.2f_{a_1(1260)}^2$ and $f_{a_2(2030)}2B(a_2(2030) \rightarrow \pi^+\pi^-\pi^0) \approx 0.2f_{a_2(1320)}^2$. The latter relation is based on the results of the measurement of the $\gamma\gamma \rightarrow \pi^+\pi^-\pi^0$ cross section in Ref. [35]. It is obtained that the radiative production of the excited a_1 and a_2 states with mass near 2 GeV/ c^2 may give 10% contribution to the measured $M_{3\pi}$ spectrum above 1.8 GeV. This value is used as an estimate of an additional systematic uncertainty associated with FSR at $M_{3\pi} > 1.8$ GeV/ c^2 .

V. DETECTION EFFICIENCY

The detection efficiency is determined using MC simulation as the ratio of the true 3π mass spectra computed after and before applying the selection criteria. The detection efficiency calculated in this way is shown in Fig. 25. Its mass dependence is fitted by a combination of a third-order polynomial in the range 0.62–2.3 GeV/ c^2 , a linear function in the range 2.3–2.9 GeV/ c^2 , and a constant above 2.9 GeV/ c^2 . For the tighter cut $\chi_{3\pi\gamma}^2 < 20$ the detection efficiency is smaller by 12–17%. The statistical error of the fitted detection efficiency is about 0.1% at the ω , 0.2% at the ϕ , and then increases to 1% at 2 GeV/ c^2 and up to 2.2% at 2.5 GeV and above.

The roll-off of the efficiency below 0.62 GeV/ c^2 is due to the merging of clusters from photons and charged pions in the calorimeter. This effect leads to π^0 loss, which increases with decrease of 3π mass. To avoid a possible systematic uncertainty due to imperfect simulation of this effect, we perform the measurement of the $e^+e^- \rightarrow \pi^+\pi^-\pi^0$ cross section at masses above 0.62 GeV/ c^2 .

The efficiency (ε_{MC}) found using MC simulation must be corrected to account for data-

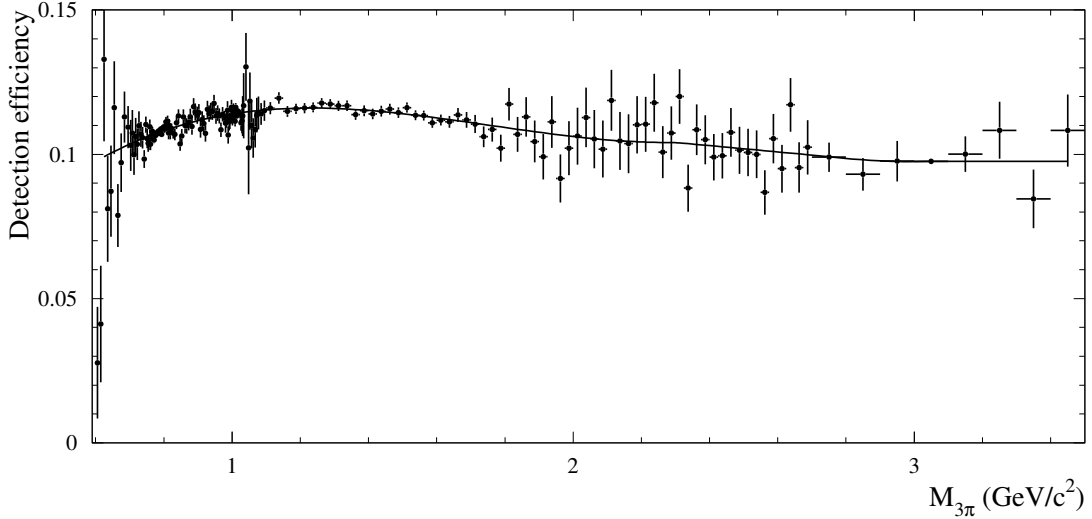


FIG. 25: The 3π -mass dependence of the detection efficiency obtained using MC simulation. The curve is the result of the fit described in the text.

MC simulation differences in detector response:

$$\varepsilon = \varepsilon_{MC} \Pi(1 + \delta_i), \quad (10)$$

where δ_i are efficiency corrections for different effects discussed below.

A. ISR photon inefficiency

A correction is applied to the ISR photon detection efficiency. There are two sources of this correction: data-MC simulation differences in the probability of photon conversion in the detector material before the DCH, and dead calorimeter channels. A sample of $e^+e^- \rightarrow \mu^+\mu^-\gamma$ events is used to determine the calorimeter photon inefficiency in data. Events with exactly two charged tracks identified as muons are selected, and a one-constraint kinematic fit is performed with the requirement that the recoil mass against the muon pair is zero. A tight condition on the χ^2 of the kinematic fit selects events with only one photon in the final state. The photon direction is determined from the fit. The detection inefficiency is calculated as the ratio of the number of events not satisfying the condition $E_\gamma^* > 3$ GeV, to the total number of selected events. The same procedure is applied to simulated $e^+e^- \rightarrow \mu^+\mu^-\gamma$ events. The efficiency correction is determined from the data-MC simulation ratio as a function of the photon polar and the $\mu^+\mu^-$ invariant mass. The

data-MC simulation difference in the probability of photon conversion is also studied using $e^+e^- \rightarrow \mu^+\mu^-\gamma$ events. In addition to two identified muons, we require that an event contain a converted-photon candidate, i.e., a pair of oppositely charged tracks with e^+e^- invariant mass close to zero, momentum directed along the expected photon direction, and forming a secondary vertex well-separated from the interaction region. The data-MC difference in the probability of photon conversion is measured as a function of the photon polar angle. Then we calculate total correction to the ISR photon efficiency due to the calorimeter inefficiency and the photon conversion.

The measured angular dependence of the correction is used to reweight the simulated $e^+e^- \rightarrow \pi^+\pi^-\pi^0\gamma$ events and calculate efficiency correction. It is found to be $-(1.0 \pm 0.2)\%$ for 3π masses below $1.1 \text{ GeV}/c^2$, $-(1.2 \pm 0.2)\%$ in the mass range $1.1\text{--}2.0 \text{ GeV}/c^2$, and $-(1.4 \pm 0.2)\%$ in the range $2.0\text{--}3.5 \text{ GeV}/c^2$. The contribution to this correction from the photon conversion is about -0.2% .

B. π^0 efficiency and kinematic-fit χ^2 distribution

From the study of the ISR photon inefficiency it is expected that the difference between data and simulation in the π^0 detection efficiency be at least -2% . To study the π^0 losses more accurately, we perform a kinematic fit for data and simulated events to the $e^+e^- \rightarrow \pi^+\pi^-\pi^0\gamma$ hypothesis using the measured parameters for only the two charged tracks and the ISR photon. The π^0 energy and angles are determined as a result of the fit. We apply a very tight condition on the fit quality and the background suppression conditions described in Sec. III. Due to the high level of remaining background we restrict our study to the ω -mass region.

The π^0 detection efficiency is determined as the fraction of selected signal events with a detected π^0 . The results depends on the definition of the π^0 candidate. For the simple π^0 definition as a pair of photons with the invariant mass near the π^0 mass, for example, in the range $0.1\text{--}0.17 \text{ GeV}/c^2$, there are a substantial probability to observe a false π^0 candidate due to a large number of spurious photons in an event. To avoid difficulties with false π^0 's, we require that an event containing the π^0 candidate satisfy our standard kinematic-fit condition $\chi^2_{3\pi\gamma} < 40$.

The 3π mass spectra for selected events with $\chi^2_{3\pi\gamma} < 40$ and $\chi^2_{3\pi\gamma} > 40$ are shown in

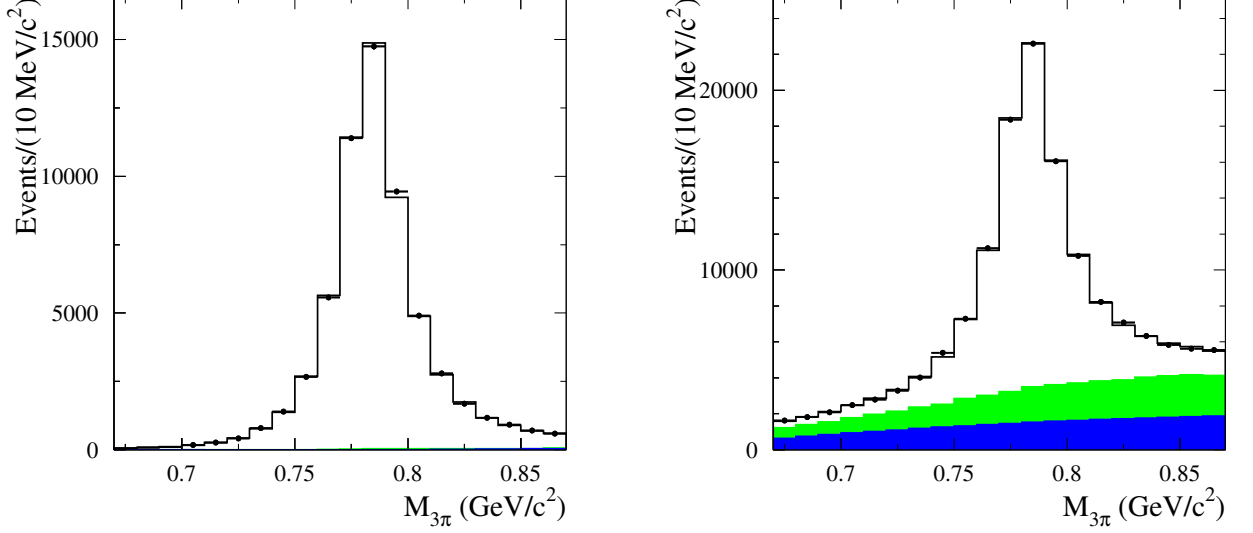


FIG. 26: The 3π mass distributions for events selected without using the photons from the π^0 decay. The left (right) plot is for events with $\chi^2_{3\pi\gamma} < 40$ ($\chi^2_{3\pi\gamma} > 40$). The points with error bars show the data distribution. The solid histogram is the result of the fit described in the text. The light shaded region represents the simulated $e^+e^- \rightarrow \pi^+\pi^-\pi^0\pi^0\gamma$ contribution. The dark shaded histogram is the fitted background contribution from other sources.

Fig. 26. The mass spectra are fitted with a sum of distributions for signal and background events. The signal distribution is extracted from the simulation. The background spectrum is a sum of the simulated distribution for $e^+e^- \rightarrow \pi^+\pi^-\pi^0\pi^0\gamma$ events and a second order polynomial with free coefficients. The efficiency correction due to π^0 losses is determined to be $\delta_2 = f_{\text{data}}/f_{\text{MC}} - 1 = -(3.4 \pm 0.5)\%$. Here f is the fraction of selected events with $\chi^2_{3\pi\gamma} < 40$.

In a similar way, we determine the efficiency correction at different ranges of the π^0 energy. The obtained energy dependence shown in Fig. 27 (left) is well described by a constant. At the current level of statistics the correction is independent of the π^0 energy. Therefore, the efficiency correction due to π^0 losses determined at the ω region can be used also at higher 3π masses.

The π^0 correction includes a part of the efficiency correction due to the $\chi^2_{3\pi\gamma} < 40$ cut related to the photons from the π^0 decay. To understand influence of the data-simulation difference in the parameters of the charged tracks and the ISR photon, we study $e^+e^- \rightarrow \mu^+\mu^-\gamma$

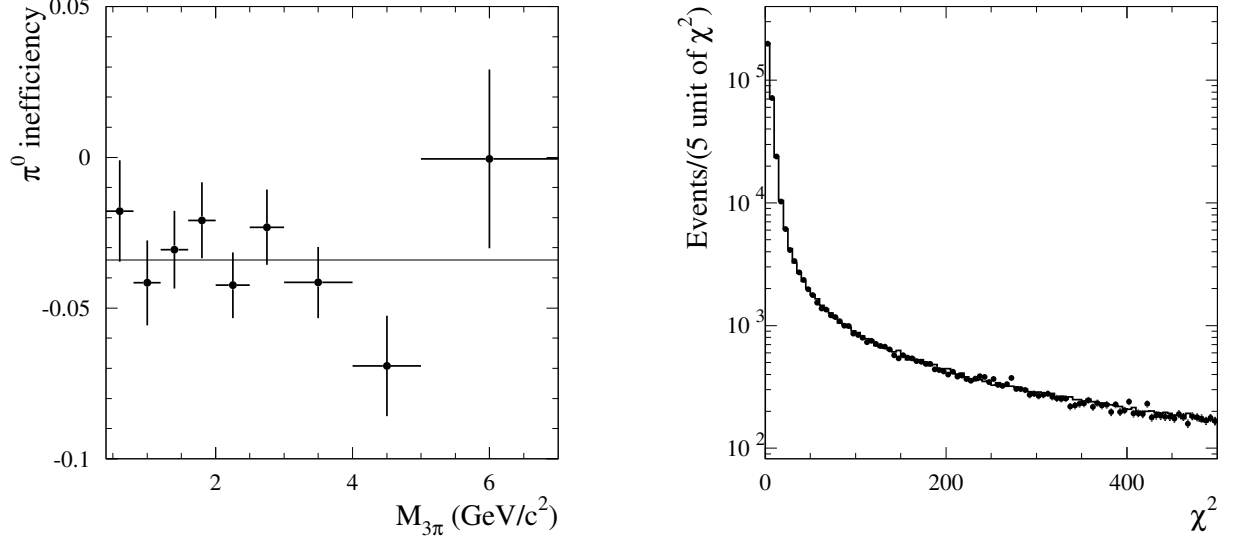


FIG. 27: Left panel: The dependence of the efficiency correction due to π^0 losses on the π^0 energy. The line is the fit to a constant. Right panel: The distributions of the χ^2 of the kinematic fit for selected data (histogram) and simulated (points with error bars) $e^+e^- \rightarrow \mu^+\mu^-\gamma$ events with the $\mu^+\mu^-$ invariant mass in the range 0.2-1.1 GeV/c^2 .

events. We select events with two charged particles identified as muons and a photon with c.m. energy larger than 3 GeV. As mentioned in Sec. II the simulation uses the requirement that the invariant mass of the muon pair and ISR photon is greater than 8 GeV/c^2 . To ensure compliance with this requirement in the data, we apply an additional condition that the invariant mass of the muon and the ISR photon candidates is greater than 9 GeV/c^2 .

For selected events a kinematic fit is performed with the requirements of energy and momentum balance. The fit uses measured momenta and angles of the muons and only angles of the ISR photon. The χ^2 distributions for selected data and simulated $e^+e^- \rightarrow \mu^+\mu^-\gamma$ events with $\mu^+\mu^-$ invariant mass $M_{\mu\mu} < 1.1 \text{ GeV}/c^2$ are compared in Fig. 27 (right). It is seen that the data and simulated distributions are in good agreement. To estimate difference between them numerically, we calculate the double ratio $R_\chi^2 = [N(\chi^2 < c)/N_0]_{\text{data}}/[N(\chi^2 < c)/N_0]_{\text{MC}}$, where N_0 is the total number of selected $\mu^+\mu^-\gamma$ events, and $N(\chi^2 < c)$ is the number of events satisfying the condition $\chi^2 < c$. This ratio is practically independent of the c value in the range $20 < c < 40$. Its deviation from unity $R_\chi^2 - 1$ in the invariant mass range $0.6 < M_{\mu\mu} < 1.1 \text{ GeV}/c^2$ equal to $-(0.4 \pm 0.2)\%$ can be used as an estimation of the

efficiency correction for $e^+e^- \rightarrow \pi^+\pi^-\pi^0\gamma$ events.

We, however, must take into account the difference in the charged-particle momentum distributions for the processes $e^+e^- \rightarrow \mu^+\mu^-\gamma$ and $e^+e^- \rightarrow \pi^+\pi^-\pi^0\gamma$. To understand a possible effect of this difference, we study the dependence of R_χ^2 on the minimum muon momentum in an event and do not observe any statistically significant dependence. However, since the phase space distribution of charged pions from the $e^+e^- \rightarrow \pi^+\pi^-\pi^0\gamma$ cannot be fully reproduced using the $e^+e^- \rightarrow \mu^+\mu^-\gamma$ events, we assign a 100% systematic uncertainty to this correction.

So, the efficiency correction associated with the difference in the χ^2 distribution between data and simulation is estimated to be $-(0.4 \pm 0.4)\%$ in the 3π mass region $0.6\text{--}1.1 \text{ GeV}/c^2$. For higher masses the correction is larger. Its average value in the mass range $1.1\text{--}3.5 \text{ GeV}/c^2$ is $(1 \pm 1)\%$.

C. Efficiency correction due to the selection criteria

Our preliminary selection contains the requirement of exactly two good quality charged tracks in an event. The definition of the good charged track is given in Sec. III. To determine an efficiency correction due to this requirement, we analyze events with three good tracks. Two of them with opposite charge having closest distance to the beam axis are selected as candidates for charged pions from the $e^+e^- \rightarrow \pi^+\pi^-\pi^0\gamma$ reaction. The fraction of three-track events determined in the 3π mass regions near the ω and ϕ resonances is about 0.4% both in data and simulation. No efficiency correction due to the requirement of exactly two charged tracks is needed.

Events satisfying the condition (3) are prescaled by a factor of 40. To determine a possible efficiency correction due to this condition, we study a sample of prescaled events passing our standard selection criteria and having $M_{3\pi}$ in the range between 0.6 and $1.1 \text{ GeV}/c^2$. From 13 events selected in data (they are located near the ω and ϕ peak positions) the fraction of $e^+e^- \rightarrow \pi^+\pi^-\pi^0\gamma$ events rejected by the condition (3) is found to be $(0.44 \pm 0.12)\%$. The same fraction in simulation is $(0.24 \pm 0.01)\%$. The efficiency correction is $-(0.20 \pm 0.12)\%$. To study the effect of the condition (4) we study a sample of events, in which one of the charged tracks does not satisfy this condition. The fraction of such events is $(1.3 \pm 0.3) \times 10^{-4}$ in data and $(2.0 \pm 0.1) \times 10^{-3}$ in simulation. The corresponding efficiency correction is

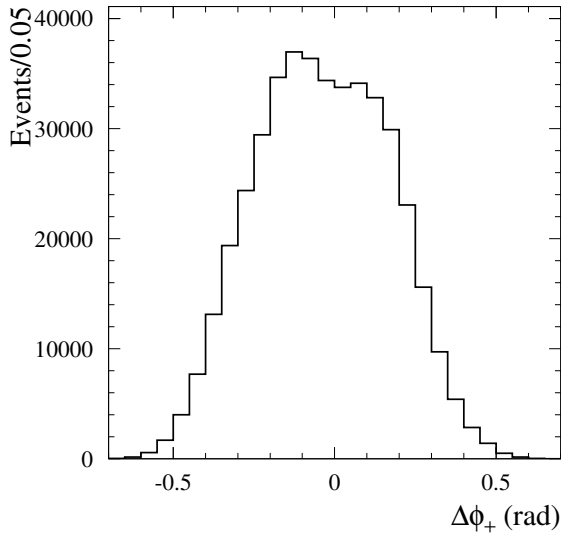


FIG. 28: The $\Delta\varphi_{\pm}$ distribution for simulated signal events from the ω mass region.

$(0.19 \pm 0.01)\%$. The total correction due to the preliminary cuts against radiative Bhabha events is $-(0.01 \pm 0.12)\%$.

The efficiency correction for the background suppression cuts described in Sec. III is determined near the ω , ϕ , and J/ψ resonances from ratios of the number of events selected with and without these cuts, in data and MC simulation. The background subtraction procedure described in Sec. IV F is used at the ω and ϕ . At the J/ψ the number of signal events is determined from the fit to the $M_{3\pi}$ spectrum by a sum of a J/ψ line shape and a linear function (see Sec. X). The fraction of signal events rejected by the background suppression cuts varies from 15% in the ω and ϕ mass region to 25% at J/ψ . This dependence is reproduced by the simulation. The efficiency correction is $(0.4 \pm 0.2)\%$ at the ω and ϕ , and $(0.6 \pm 0.8)\%$ at the J/ψ . The latter correction are used in the energy region above 1.1 GeV.

D. Efficiency correction due to track losses

The data-MC simulation difference in track losses for isolated tracks is studied using $e^+e^- \rightarrow \tau^+\tau^-$ events, with one τ decaying leptonically and the other τ hadronically with three charged particles. No difference between data and simulation in the tracking efficiency is observed within an uncertainty of 0.24% per track. In $e^+e^- \rightarrow \pi^+\pi^-\pi^0\gamma$ events, especially

at small $M_{3\pi}$, the angle between charged tracks may be small, and the effect of track overlap in the DCH should be taken into account. To study this effect we analyze the distribution of the azimuthal angle difference between the positive and negative tracks $\Delta\varphi_{\pm} = \varphi^+ - \varphi^-$. In the BABAR magnetic field events with $\Delta\varphi_{\pm} > 0$ exhibit a “fishtail” two-track configuration in which the tracks tend to overlap. The $\Delta\varphi_{\pm}$ distribution for simulated signal events from the ω mass region is shown in Fig. 28. The track overlap leads to asymmetry of the distribution. It should be noted that larger $\Delta\varphi_{\pm}$ value corresponds to larger difference between charged pion momenta. Therefore the asymmetry in the distribution is seen even at relatively large $\Delta\varphi_{\pm} \sim 0.5$. With $M_{3\pi}$ increase the $\Delta\varphi_{\pm}$ becomes wider and more symmetric. We estimate the fraction of events lost because of track overlap as

$$f_{\text{overlap}} = \frac{N(\Delta\varphi_{\pm} < 0) - N(\Delta\varphi_{\pm} > 0)}{2N(\Delta\varphi_{\pm} < 0)}. \quad (11)$$

This fraction is 11% at the ω , 8% at the ϕ , and about 1% at the J/ψ . We do not observe any significant difference in this fraction between data and simulation. The difference calculated over the 3π mass range 0.6–1.1 GeV/ c^2 is $-(0.03 \pm 0.23)\%$. The error of this difference is used as an estimate of the systematic uncertainty associated with track overlap in the DCH. The total systematic uncertainty in the detector efficiency due to data-MC simulation difference in the tracking efficiency and track overlap is estimated to be 0.5%.

E. Efficiency correction due to trigger and background filters

We also studied the quality of the simulation of trigger and background filters used in event reconstruction. In the analysis we use events passing through the two trigger lines L3OutDCH and L3OutEMC, which are based on signals from the DCH and EMC, respectively. The inefficiency of these lines in the simulation is 6.1% for L3OutDCH and $(2.3 \pm 0.2) \times 10^{-4}$ for L3OutEMC. A logical OR of the L3OutDCH and L3OutEMC lines has a very small inefficiency, $(1.2 \pm 0.1) \times 10^{-4}$. The inefficiencies for the trigger lines in data can be estimated using the overlap of the samples of events passing through them. The simulation shows that these estimates are very close to the true inefficiencies of the trigger lines. This method applied to data gives the inefficiency $(6.6 \pm 0.1)\%$ for L3OutDCH and $(3.8 \pm 0.6) \times 10^{-4}$ for L3OutEMC. Although the efficiency in data is lower, the efficiency itself is very close to 100%. Therefore no correction is needed for the trigger inefficiency.

TABLE IV: Efficiency corrections (in %) for different effects in three $M_{3\pi}$ regions.

effect	$M_{3\pi} < 1.1 \text{ GeV}/c^2$	$1.1 < M_{3\pi} < 2 \text{ GeV}/c^2$	$M_{3\pi} > 2 \text{ GeV}/c^2$
photon efficiency	-1.0 ± 0.2	-1.2 ± 0.2	-1.4 ± 0.2
π^0 loss	-3.4 ± 0.5	-3.4 ± 0.5	-3.4 ± 0.5
$\chi^2_{3\pi\gamma}$ distribution	-0.4 ± 0.4	-1 ± 1	-1 ± 1
rad. Bhabha suppression	0.0 ± 0.1	0.0 ± 0.1	0.0 ± 0.1
background suppression	0.4 ± 0.2	0.6 ± 0.5	0.6 ± 0.8
track loss	0.0 ± 0.5	0.0 ± 0.5	0.0 ± 0.5
trigger and filters	-1.4 ± 0.7	-1 ± 1	-1 ± 1
total	-5.8 ± 1.1	-6.0 ± 1.7	-6.2 ± 1.8
$\chi^2_{3\pi\gamma} < 20$	0.1 ± 0.1 at ω 0.4 ± 0.4 at ϕ	$0.5-1.1$	$1.1-1.8$

The inefficiency of the background filters in simulation is about 1.8% at the ω and ϕ mass regions and then decrease to 0.5% at $2 \text{ GeV}/c^2$ and to 0.3% at the J/ψ . To measure this inefficiency in data we use a subsample of prescaled events, which does not pass through the background filters. The prescale factor is 200. The filter inefficiency for 3π masses below 1.1 GeV is measured to be $(3.2 \pm 0.7)\%$. The efficiency correction in this mass region is $-(1.4 \pm 0.7)\%$. At $M_{3\pi} > 1.1 \text{ GeV}/c^2$ insufficient statistics and large background do not allow to determine the inefficiency with acceptable accuracy. Therefore, in this region we use the correction $-(1 \pm 1)\%$, which cover the range of its possible variations as a function of mass.

Efficiency corrections δ_i are summarized in Table IV. The total efficiency correction is about -6% .

In Sec. VI we also analyze the mass spectrum for events with $\chi^2_{3\pi\gamma} < 20$. The additional correction related to this cut is 0.001 ± 0.001 at the ω , 0.004 ± 0.004 at the ϕ , and 0.018 ± 0.007 at the J/ψ . A linear interpolation is used between the resonances.

F. Model uncertainty

The signal simulation uses the model of the $\rho(770)\pi$ intermediate state. This model works well in the ω and ϕ mass region, below 1.1 GeV [9, 10]. To estimate the model dependence of the detection efficiency in the mass range 1.1–2 GeV/ c^2 the simulated signal events are reweighed using the model with a sum of the $\rho(770)\pi$, $\omega\pi^0$, and $\rho(1450)\pi$ mechanisms with coefficients and relative phases taken from the SND measurement [7]. The difference in the detection efficiency between the two models depends on energy but does not exceed 1.5%. This number is taken as an estimate of the model uncertainty of the detection efficiency both in the region 1.1–3.5 GeV/ c^2 .

The similar procedure is used to find the correction to the detection efficiency at J/ψ . Here we use the result of the Dalitz plot analysis of Ref. [11]. About 10% contribution of the $\rho(1450)\pi$ mechanism leads to a shift in the detection efficiency of $-(0.5 \pm 0.1)\%$.

VI. FIT TO THE $\pi^+\pi^-\pi^0$ INVARIANT MASS DISTRIBUTION

To measure the $e^+e^- \rightarrow \pi^+\pi^-\pi^0$ cross section, detector resolution effects need to be unfolded from the measured 3π invariant-mass spectrum. In Fig. 29 (left) the simulated distribution of the true 3π mass in the energy regions of the ω and ϕ resonances is compared with the distribution of the reconstructed 3π mass. The true spectrum varies by four orders of magnitude and has two narrow peaks. The reconstructed spectrum strongly differ from the true one. For such a spectrum, the result of the unfolding procedure is very sensitive to the quality of simulation used to obtain the resolution function. To study the difference between data and simulation in resolution, we fit to the measured 3π mass spectrum with the vector-meson-dominance model including several resonances. The ω and ϕ masses and widths are known with relatively high accuracy. Therefore from the fit we can extract mass shift and sigma of an additional smearing Gaussian function needed to describe data-MC simulation difference in the mass resolution. These parameters can be determined separately for the ω and ϕ resonances.

The detector resolution function has long non-Gaussian tails as seen in Fig. 29 (right), where the distribution of the difference between the reconstructed and true mass ($\Delta M_{3\pi}$) is shown for events from the ω peak. To increase the fraction of events in non-Gaussian tails,

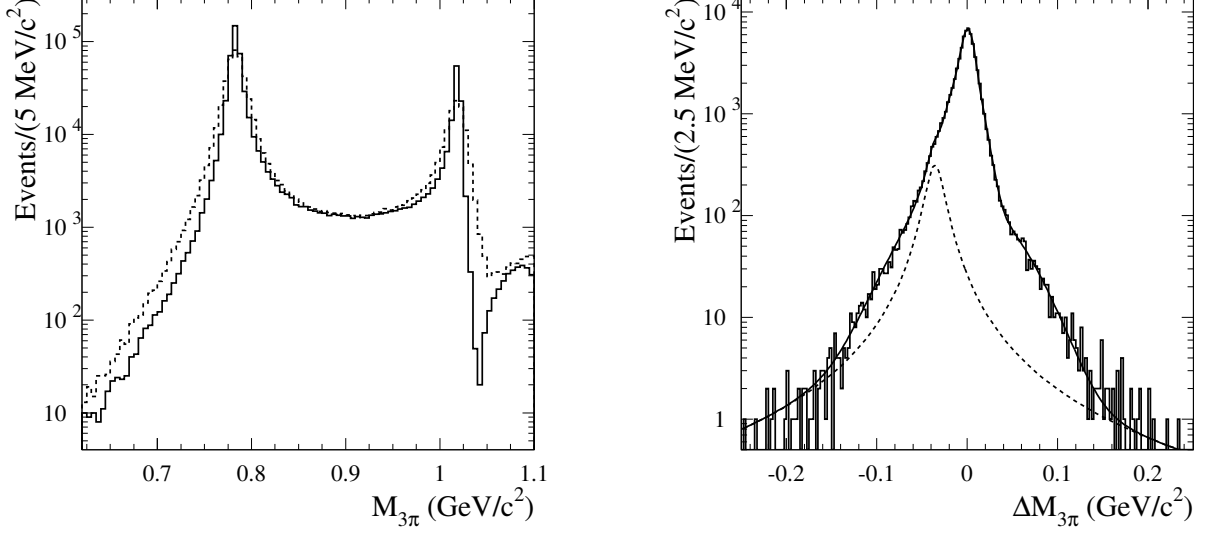


FIG. 29: Left panel: The distributions of the true (solid histogram) and reconstructed (dashed histogram) 3π mass for simulated signal events. Right panel: The distribution of the difference between the reconstructed and true mass for simulated signal events with $20 < \chi^2_{3\pi\gamma} < 40$ from the ω peak. The curve is the result of the fit described in the text.

events are selected with the condition $20 < \chi^2_{3\pi\gamma} < 40$. The distribution is fitted by a sum of three Gaussians and a Lorentzian function $L(x) = (\gamma/\pi)/((x - x_0)^2 + \gamma^2)$. The latter is shown in Fig. 29 (right) by the dashed histogram. Because of asymmetry of the $\Delta M_{3\pi}$ distribution the maximum of the Lorentzian function is shifted from zero by about -30 MeV. The same shift is observed in the $\Delta M_{3\pi}$ distribution at $750, 900 \text{ GeV}/c^2$, and the ϕ . To describe a possible difference between data and simulation in the tails of the resolution function, we introduce to the fit a smearing Lorentzian function with $x_0 = -30 \text{ MeV}$.

The following probability density function is used in the fit to the measured $M_{3\pi}$ spectrum

$$\left(\frac{dN}{dm}\right)_i^{meas} = (1 - \epsilon) \sum_j P_{ij} \left[\left(\frac{dN}{dm}\right) * G \right]_j + \epsilon \left[\left(\frac{dN}{dm}\right) * L \right]_i, \quad (12)$$

where the theoretical spectrum of true 3π mass (dN/dm) is convolved with the smearing Gaussian (G) and Lorentzian (L) functions. The spectra of true and measured masses are presented as histograms with the same binning. The folding matrix $P_{i,j}$ obtained using simulation gives the probability that an event with true mass in bin j is actually reconstructed in bin i . From the fit we determine the sigmas of the smearing Gaussian and mass shifts at

the ω and ϕ , ϵ , and γ of the smearing Lorentzian.

The width of the mass bins near the ω and ϕ resonances is chosen to be 2.5 MeV/ c^2 . This width is not much smaller than the resonance widths. Therefore the elements of the matrix $P_{i,j}$ depend on the values of the resonance parameters used in simulation. We correct the folding matrix by an iterative procedure. The procedure uses results of the fit without Lorentzian smearing (Model 4 in Table V) for events with $\chi^2_{3\pi\gamma} < 20$. Simulated events are reweighted by the ratio of the fitted spectrum $(dN/dm) * G$ to the true simulated spectrum. The reweighting is performed with bin width of 0.5 MeV/ c^2 . Then a new matrix $P_{i,j}$ is obtained, and the fit is repeated. We iterate until the change in $(dN/dm)^{true} * G$ between two successive iterations is less than 0.1%.

The true mass spectrum in the fit is described by the following function:

$$\frac{dN}{dm} = \sigma_{3\pi}(m) \frac{dL}{dm} R \varepsilon, \quad (13)$$

where $\sigma_{3\pi}(m)$ is the Born cross section for $e^+e^- \rightarrow 3\pi$, dL/dm is the so-called ISR differential luminosity, ε is the detection efficiency as a function of mass, and R is a radiative correction factor accounting for the Born mass spectrum distortion due to emission of several photons by the initial electron and positron. The ISR luminosity is calculated using the total integrated luminosity L and the probability density function for ISR photon emission (Eq. (2)):

$$\frac{dL}{dm} = \frac{\alpha}{\pi x} \left((2 - 2x + x^2) \log \frac{1+C}{1-C} - x^2 C \right) \frac{2m}{s} L. \quad (14)$$

Here $x = 1 - m^2/s$, \sqrt{s} is the e^+e^- c.m. energy, $C = \cos \theta_0$, and θ_0 determines the range of polar angles in the c.m. frame: $\theta_0 < \theta_\gamma < 180^\circ - \theta_0$ for the ISR photon. In our case θ_0 is equal to 20° , since we determine the detector efficiency using the simulation with $20^\circ < \theta_\gamma < 160^\circ$.

The Born cross section for $e^+e^- \rightarrow 3\pi$ can be written as the sum of the contributions of five resonances $\rho \equiv \rho(770)$, $\omega \equiv \omega(782)$, $\phi \equiv \phi(1020)$, $\omega' \equiv \omega(1420)$, and $\omega'' \equiv \omega(1650)$

$$\sigma_{3\pi}(m) = \frac{12\pi}{m^3} F_{\rho\pi}(m) \left| \sum_{V=\rho,\omega,\phi,\omega',\omega''} \frac{\Gamma_V m_V^{3/2} \sqrt{\mathcal{B}(V \rightarrow e^+e^-) \mathcal{B}(V \rightarrow 3\pi)}}{D_V(m)} \frac{e^{i\phi_V}}{\sqrt{F_{\rho\pi}(m_V)}} \right|^2, \quad (15)$$

where m_V and Γ_V are the mass and width of the resonance V , ϕ_V is its phase, $\mathcal{B}(V \rightarrow e^+e^-)$ and $\mathcal{B}(V \rightarrow 3\pi)$ are the branching fractions of V into e^+e^- and 3π ,

$$D_V(m) = m_V^2 - m^2 - im\Gamma_V(m), \quad \Gamma_V(m) = \sum_f \Gamma_f(m).$$

Here $\Gamma_f(m)$ is the mass-dependent partial width of the resonance decay into the final state f , and $\Gamma_f(m_V) = \Gamma_V \mathcal{B}(V \rightarrow f)$. The mass-dependent width for the ω and ϕ mesons has been calculated taking into account all significant decay modes. The corresponding formulae can be found, for example, in Ref. [3]. We assume that $V \rightarrow 3\pi$ decay proceeds via the $\rho\pi$ intermediate state, and $F_{\rho\pi}(m)$ is the 3π phase space volume calculated under this hypothesis. The formula for $F_{\rho\pi}$ calculation can be found in Ref. [3].

The radiative correction factor is determined using Monte Carlo simulation (at the generator level, with no detector simulation) with PHOKHARA event generator [36]. This generator includes the next-to-leading (NLO) ISR contributions. Accuracy of the cross section calculation for ISR processes with ISR photon emitted at large angle is estimated to be 0.5% [37]. Since the radiative correction is independent on process, we generate $e^+e^- \rightarrow \mu^+\mu^-\gamma$ events with switched off final state radiation, and take a ratio the mass spectra obtained in the NLO and LO generator modes. With the cut on the invariant mass of the $\mu^+\mu^-\gamma$ system $M_{\mu\mu\gamma} > 8 \text{ GeV}/c^2$, this ratio is weakly dependent on mass and is equal to $R = 1.0077 \pm 0.0005$ below $1.1 \text{ GeV}/c^2$, 1.0086 ± 0.0004 between 1.1 and $2 \text{ GeV}/c^2$, and 1.0091 ± 0.0004 in the range $2\text{--}3.5 \text{ GeV}/c^2$. The quoted error reflects the R variation in the specified mass range. The radiative correction factor does not include the corrections due to leptonic and hadronic vacuum polarization. Here we follow the generally accepted practice [38] of including the vacuum polarization correction to the resonance electronic width. The total integrated luminosity is measured with accuracy of 0.43% [39].

The free parameters in the fit are the scale factors for products of the branching fractions $\mathcal{B}(V \rightarrow e^+e^-)\mathcal{B}(V \rightarrow 3\pi)$, the masses and widths for ω' and ω'' . The ω meson mass is fixed at the Particle Data Group (PDG) value [40], while for the width we take the value of $(8.68 \pm 0.13) \text{ MeV}/c^2$ obtained in the CMD2 [4] and SND [3] experiments. The mass and width of the ϕ meson are fixed at the PDG values [40].

The phase of ω meson is set to zero. The relative phase between the ω and ϕ amplitudes, $\phi_\phi = (163 \pm 7)^\circ$, is taken from Ref. [3]. The phases of the ω' and ω'' are fixed at values of 180° and 0° [41] with uncertainty of 20° . This uncertainty is estimated from the deviation of ϕ_ϕ from 180° . Our fitting function does not take into account the isovector $e^+e^- \rightarrow \omega\pi\gamma \rightarrow 3\pi\gamma$ contribution and the presence of $\omega'' \rightarrow \rho(1450)\pi$ decay. Therefore we do not expect that the parameters of excited ω states are determined correctly. Their inclusion into the fit is needed to study effect of interference of the ω and ϕ amplitudes with

TABLE V: Models used to describe the 3π mass spectrum (142 bins) and the obtained χ^2/ν values of the fits, where ν is the number of degrees of freedom. The first four rows shows the results for the standard selection criteria, while the last four are for the tighter cut on the χ^2 of the kinematic fit ($\chi^2_{3\pi\gamma} < 20$).

Model	Lorentzian smearing	$\mathcal{B}(\rho \rightarrow 3\pi)$	χ^2/ν
1	yes	free	136/127
2	no	$\equiv 0$	201/131
3	yes	$\equiv 0$	180/129
4	no	free	147/129
1	yes	free	135/127
2	no	$\equiv 0$	181/131
3	yes	$\equiv 0$	178/129
4	no	free	136/129

the contributions of the excited states. The fitted mass region is restricted to masses below 1.8 GeV.

The branching fraction of the $\rho \rightarrow \pi^+\pi^-\pi^0$ decay can be estimated assuming that the dominant mechanism of the $\omega \rightarrow \pi^+\pi^-$ and $\rho \rightarrow \pi^+\pi^-\pi^0$ decay is the ρ - ω mixing. Under this assumption the coupling $g_{\rho \rightarrow 3\pi} = \varepsilon g_{\omega \rightarrow 3\pi}$, where the mixing parameter $|\varepsilon|^2 \approx \Gamma(\omega \rightarrow 2\pi)/\Gamma(\rho \rightarrow 2\pi)$, and $\mathcal{B}(\rho \rightarrow 3\pi) \approx 0.4 \times 10^{-4}$. The phase ϕ_ρ is expected to be close to -90° . A significantly larger value of ε is obtained in Ref. [42], where data on the pion electromagnetic form factor are analyzed in the model including both ρ - ω mixing and direct isospin-breaking $\omega \rightarrow 2\pi$ decay. Using the result of Ref. [42] we obtain $\mathcal{B}(\rho \rightarrow 3\pi) \approx (2.5 \pm 1.0) \times 10^{-4}$ and $\phi_\rho = -(40 \pm 13)^\circ$. The experimental values of the branching fraction and phase are $1.01^{+0.54}_{-0.36} \pm 0.34$ and $-(135^{+17}_{-13} \pm 0.9)^\circ$ [3]. With current experimental accuracy, $\sim 1\%$ at ω meson, the contribution of the $\rho \rightarrow \pi^+\pi^-\pi^0$ decay with a branching fraction of about 10^{-4} must be taken into account in the fit.

The 3π mass spectrum and the results of the fit in Models 1,2,3 listed in Table V are shown in Fig. 30. The smearing Gaussian sigma obtained in Model 1 is 1.5 ± 0.2 GeV/ c^2 at the ω and 1.5 ± 0.4 GeV/ c^2 at the ϕ . Therefore, in what follows we use the mass-independent smearing sigma. The fitted parameters of the smearing Lorentzian function are following:

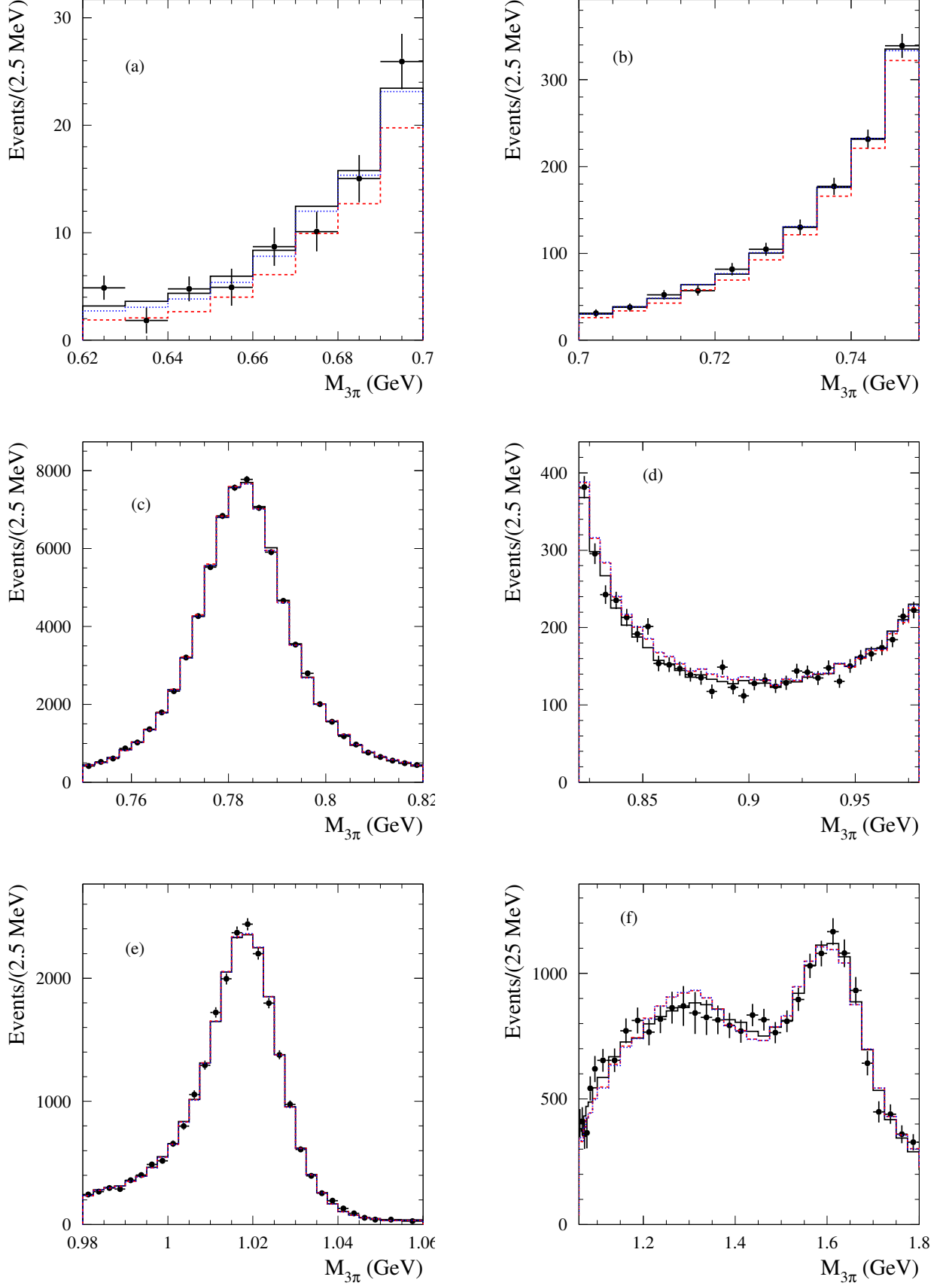


FIG. 30: The 3π mass spectrum in six regions: (a) $0.62-0.70 \text{ GeV}/c^2$, (b) $0.70-0.74 \text{ GeV}/c^2$, (c) $0.74-0.82 \text{ GeV}/c^2$, (d) $0.82-0.98 \text{ GeV}/c^2$, (e) $0.98-1.06 \text{ GeV}/c^2$, (f) $1.06-1.80 \text{ GeV}/c^2$. The solid, dashed, and dotted histograms represent the results of the fit in Models 1, 2, and 3 listed in Table V, respectively.

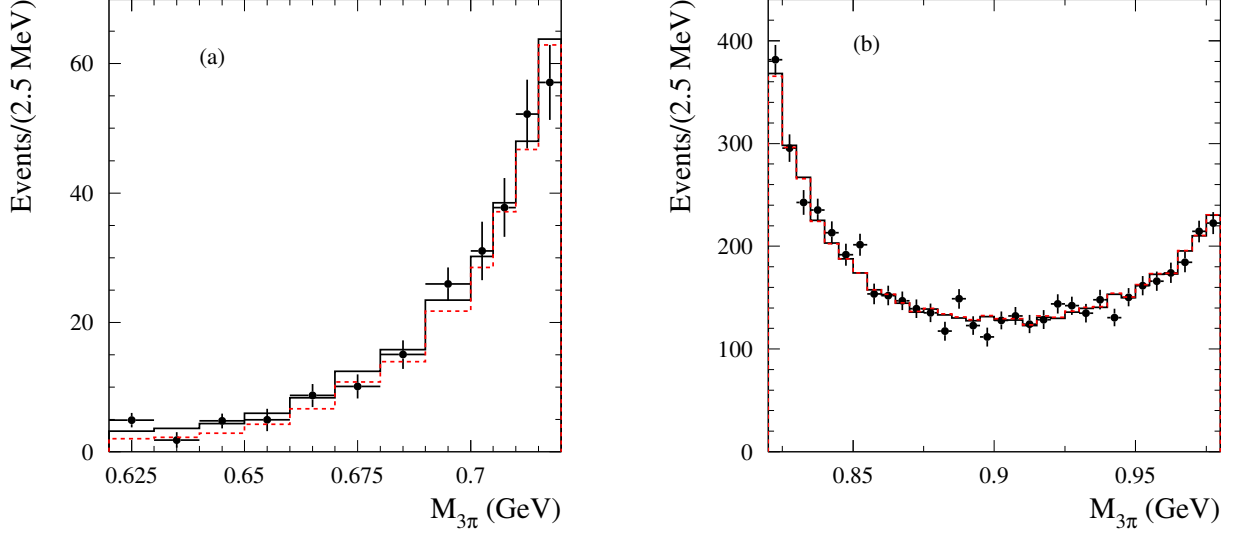


FIG. 31: The 3π mass spectrum in the regions (a) $0.62\text{--}0.72\text{ GeV}/c^2$ and (b) $0.82\text{--}0.98\text{ GeV}/c^2$. The solid, dash-dotted histograms represent the results of the fit in Models 1 and 4 listed in Table V, respectively.

$\epsilon = 0.007 \pm 0.002$, $\gamma = 63 \pm 35\text{ GeV}/c^2$. The physical fit parameters will be discussed below.

It is seen from the Fig. 30, that the fit in Model 2 ($\mathcal{B}(\rho \rightarrow 3\pi) = 0$, no smearing Lorentzian) cannot describe data well below $0.73\text{ GeV}/c^2$ and in the region $0.82\text{--}0.9\text{ GeV}/c^2$. Including the smearing Lorentzian function (Model 3) improve fit in the energy region below the ω . The region $0.82\text{--}0.9\text{ GeV}/c^2$ cannot be described reasonably without the $\rho \rightarrow 3\pi$ decay. The model 2 and 3 have also a worse fit quality in the mass range $1.05\text{--}1.8\text{ GeV}/c^2$. This is because the fit tries to compensate the absence of the $\rho \rightarrow 3\pi$ decay by increasing the contribution from the tails of the $\omega(1420)$ and $\omega(1650)$ resonances.

The difference between Model 1 and Model 4 (free $\mathcal{B}(\rho \rightarrow 3\pi)$, no Lorentzian smearing) is maximal in the 3π mass region $0.62\text{--}0.72\text{ GeV}/c^2$ (see Fig. 31). To decrease the difference between the measured and predicted spectrum below the ω peak in absence of the Lorentzian smearing, the fit in Model 4 increase $\mathcal{B}(\rho \rightarrow 3\pi)$ by 14%.

To minimize the influence of the data-simulation difference in resolution to the fitted parameters, we tighten the condition on $\chi^2_{3\pi\gamma}$ from 40 to 20. In the last four rows of Table V, we compare the quality of the fit with Models 1–4 to the mass spectrum obtained with the tighter $\chi^2_{3\pi\gamma}$ cut. It is seen that inclusion of the Lorentzian smearing in this case improves the fit quality insignificantly. The obtained parameters of the Lorentzian smearing function

are $\epsilon = 0.0022 \pm 0.0016$ and $\gamma = 59_{-31}^{+54} \text{ MeV}/c^2$. Therefore, below we quote fit parameters for Model 4. The sigma of the smearing Gaussian function and the mass shifts for the ω and ϕ mesons are obtained to be $\sigma_s = 1.4 \pm 0.2 \text{ MeV}/c^2$, $m_\omega - m_\omega^{\text{PDG}} = 0.04 \pm 0.06 \text{ MeV}/c^2$, and $m_\phi - m_\phi^{\text{PDG}} = 0.08 \pm 0.08 \text{ MeV}/c^2$. The latter two parameters are consistent with zero.

Since the mass resolution (full width at half-maximum is about $13 \text{ MeV}/c^2$ at the ω and $15 \text{ MeV}/c^2$ at the ϕ) is larger than the ω and ϕ widths, the parameter less sensitive to the resolution effects is the area under resonance curve, i.e. $\Gamma(V \rightarrow e^+e^-)\mathcal{B}(V \rightarrow \pi^+\pi^-\pi^0)$. From the fit we obtain

$$\begin{aligned}\Gamma(\omega \rightarrow e^+e^-)\mathcal{B}(\omega \rightarrow \pi^+\pi^-\pi^0) &= (0.5698 \pm 0.0031 \pm 0.0082) \text{ keV}, \\ \Gamma(\omega \rightarrow e^+e^-)\mathcal{B}(\omega \rightarrow \pi^+\pi^-\pi^0) &= (0.1841 \pm 0.0021 \pm 0.0080) \text{ keV}.\end{aligned}\quad (16)$$

For the ρ meson, we determine

$$\begin{aligned}\mathcal{B}(\rho \rightarrow 3\pi) &= (0.88 \pm 0.23 \pm 0.30) \times 10^{-4}, \\ \phi_\rho &= -(99 \pm 9 \pm 15)^\circ.\end{aligned}\quad (17)$$

The significance of the $\rho \rightarrow 3\pi$ decay estimated from the difference between the χ^2 values for Models 4 and 2 is greater than 6σ .

The first errors in Eqs. (16) and (17) are statistical, while the second systematic. The latter include the systematic uncertainties of the ISR luminosity, radiative correction and detection efficiency. The uncertainty due to the data/MC difference in the mass resolution line shape is estimated as a difference between results of the fits with Models 4 and 1. We also vary within the errors the values of the parameters ϕ_ϕ , Γ_ω and Γ_ϕ , and the scale factors for the background processes. These contributions to the systematic uncertainties are listed in Table VI.

Our fitting model given by Eq. (15) assumes that the $e^+e^- \rightarrow \pi^+\pi^-\pi^0$ process proceed via the $\rho(770)\pi$ intermediate state. Actually, due to a sizable $\omega(1650) \rightarrow \rho(1450)\pi \rightarrow 3\pi$ transition [7] and existence of the $e^+e^- \rightarrow \omega\pi^0 \rightarrow \pi^+\pi^-\pi^0$ process the $e^+e^- \rightarrow \pi^+\pi^-\pi^0$ amplitude above the ϕ cannot be presented as a simple coherent sum of the $\omega(1420)$ and $\omega(1650)$ amplitudes. To study effect of non- $\rho(770)\pi$ mechanisms, we remove from the fit the BABAR data above $1.1 \text{ GeV}/c^2$ and use instead of them the the SND data on the $\rho(770)\pi$ and $\rho(1450)\pi$ cross sections and the phase difference between these amplitudes [7]. The new fit includes the $\omega(1420)$ transition to $\rho(770)\pi$ and $\omega(1650)$ transitions to $\rho(770)\pi$

TABLE VI: Contributions to the systematic errors of fit parameters from different effects ($P_1 = \Gamma(\omega \rightarrow e^+e^-)\mathcal{B}(\omega \rightarrow \pi^+\pi^-\pi^0)$, $P_2 = \Gamma(\phi \rightarrow e^+e^-)\mathcal{B}(\phi \rightarrow \pi^+\pi^-\pi^0)$, $P_3 = \mathcal{B}(\rho \rightarrow \pi^+\pi^-\pi^0)$, $P_4 = \phi_\rho$).

Effect	P_1 (%)	P_2 (%)	P_3 (%)	P_4 (deg)
Luminosity	0.4	0.4	0.4	–
Radiative correction	0.5	0.5	0.5	–
Detection efficiency	1.1	1.1	1.1	–
MC statistics	0.1	0.2	0.2	–
Lorentzian smearing	0.3	0.4	4.7	12
Γ_ω	0.4	0.2	13.0	8
Γ_ϕ	0.0	0.0	0.3	0
ϕ_ϕ	0.2	3.1	6.1	1
Background subtraction	0.1	0.2	7.3	2
$\omega(1680) \rightarrow \rho(1450)\pi$	0.4	2.7	30.0	0
total	1.4	4.3	34.5	15

and $\rho(1450)\pi$. The $e^+e^- \rightarrow \pi^+\pi^-\pi^0$ cross section below 1.1 GeV/ c^2 is calculated taking into account interference between the $\rho(770)\pi$ and $\rho(1450)\pi$ amplitudes. This new approach modifies the contribution of the $\omega(1420)$ and $\omega(1650)$ resonances in the 3π mass region below 1.1 GeV/ c^2 and shifts the parameters of the ρ , ω and ϕ resonances. In particular, for the ρ decay we obtain

$$\mathcal{B}(\rho \rightarrow 3\pi) = (1.14_{-0.28}^{+0.32}) \times 10^{-4}. \quad (18)$$

The difference between results of this new fit and our nominal fit are used as an estimate of systematic uncertainty due to the $\omega(1650) \rightarrow \rho(1450)\pi$ decay (see Table VI.)

The fitted values of $\Gamma(V \rightarrow e^+e^-)\mathcal{B}(V \rightarrow 3\pi)$ for the ω and ϕ mesons given by Eq. (16) are in reasonable agreement with the corresponding world average values [40]: 0.557 ± 0.011 keV and 0.1925 ± 0.0043 keV, respectively. For the ω meson the accuracy of our result is comparable with the accuracy of the PDG value. For ϕ meson we have large systematic uncertainty related to the interference between ϕ -meson amplitude and amplitudes of the resonances of the ω family. The fitted values of $\mathcal{B}(\rho \rightarrow 3\pi)$ and ϕ_ρ given by Eq. (17) are in

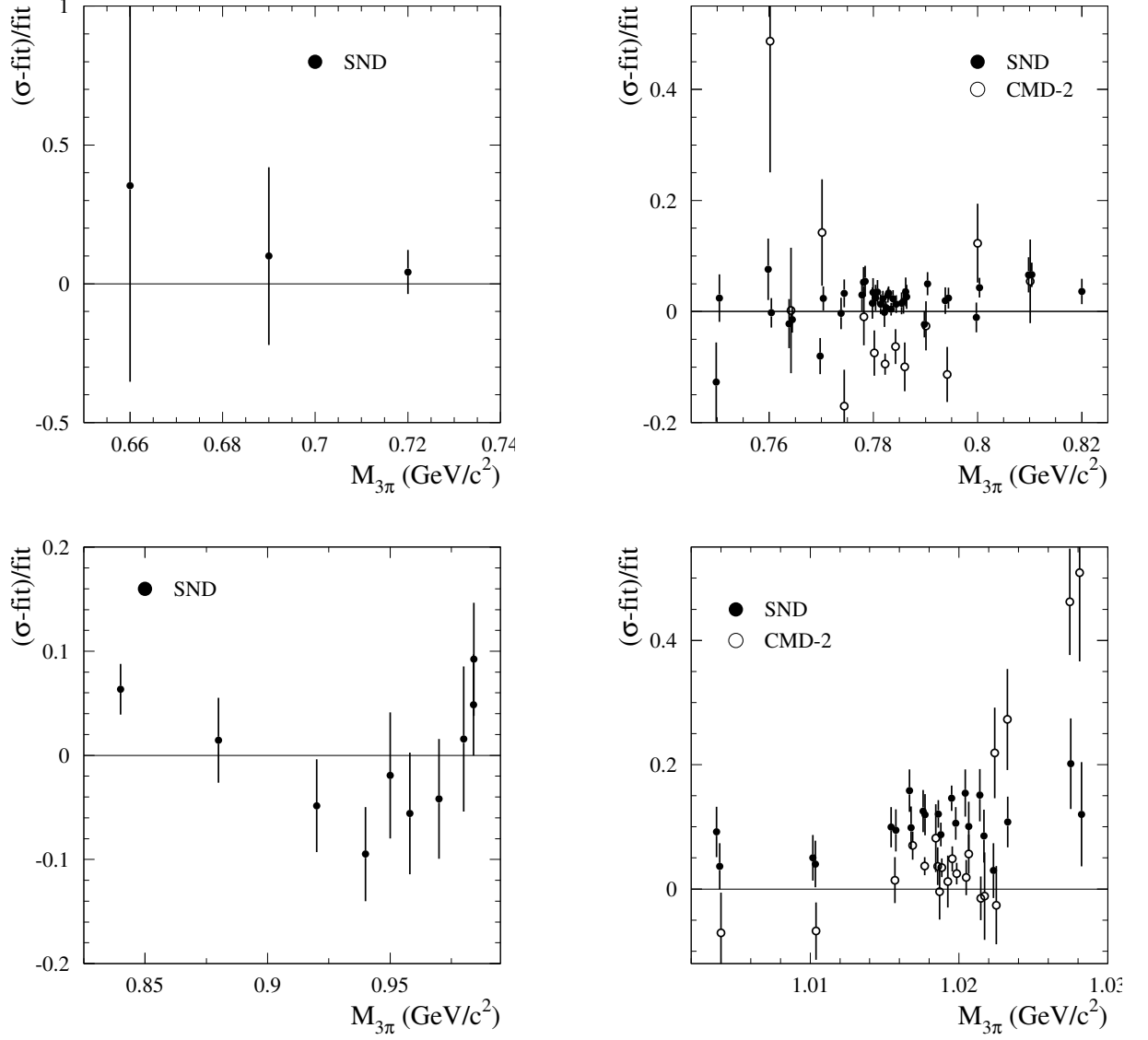


FIG. 32: The relative difference between SND [2, 3] and CMD-2 [4, 5] data on the $e^+e^- \rightarrow \pi^+\pi^-\pi^0$ cross section and the cross section calculated using Eq. (15) with parameters obtained from the fit to the 3π mass spectrum. The errors shown for the SND and CMD2-2 data are statistical. The systematic uncertainty is 3.4% for the SND data at the ω [3], 1.3% for the CMD-2 data at the ω [4], 5% for the SND data at the ϕ [3], 2.5% for the CMD-2 data at the ϕ [5]. The systematic uncertainty of the BABAR cross section is about 1.5%.

agreement with the SND results: $1.01^{+0.54}_{-0.36} \pm 0.34$ and $-(135^{+17}_{-13} \pm 9)^\circ$ [3].

It is instructive to compare the cross section calculated using Eq. (15) with the SND and CMD-2 data [2–5]. Such comparison is presented in Fig. 32, where the difference between SND and CMD-2 data and the BABAR fit is shown in the energy region of the ω and ϕ resonances. A shift in the energy (3π mass) scale between different sets of data leads to appearance of wiggles in the relative difference between them near the resonance maximum. To eliminate these wiggles we shift the SND (CMD-2) data by -0.18 (0.09) MeV at the ω region, and 0.09 (0.13) MeV at the ϕ region. It is seen that the BABAR cross section is in reasonable agreement with the SND data below the ϕ . At the ω the difference between the SND and BABAR cross section is about 2%, well below the systematic uncertainty (3.4% for SND and 1.3% for BABAR). The CMD-2 points at the ω lie about 7% below zero. With the CMD-2 statistical and systematic uncertainties of 1.8% and 1.3%, respectively, the difference between CMD-2 and BABAR is 2.7σ . Near the maximum of the ϕ -meson resonance the CMD-2 and SND data with systematic uncertainties of 2.5% and 5%, respectively, lie about 4% and 11% higher than the BABAR cross section.

VII. MEASUREMENT OF THE $e^+e^- \rightarrow \pi^+\pi^-\pi^0$ CROSS SECTION BELOW 1.1 GeV/c²

Different strategies for the cross section measurement used in the $m_{3\pi}$ regions below and above 1.1 GeV/c². We used an iterative unfolding technique that is a simplified version of a method developed for more complex unfolding problems [46]. This approach was used in the similar analyses with BABAR detector of the $e^+e^- \rightarrow \pi^+\pi^-\gamma$ [47] and $e^+e^- \rightarrow K^+K^-\gamma$ [48] processes. The folding matrix P_{ij} discussed in the Sec. VI and multiplied to the MC vector $(\frac{dN}{dm})_{FIT}^{true}$ is shown in Fig. 33. The vector corresponds to the fit to the $\pi^+\pi^-\pi^0$ invariant mass distribution discussed in previous section. The first iteration step corrects the main resolution effects on the data spectrum. The folding matrix is improved after the next step, to bring the shape of the reconstructed MC mass spectrum into better agreement with the data. The iteration step does not lead to significant change of the result because the MC spectrum is based on the fit of measured $m_{3\pi}$ mass spectrum and the model used in the fit described well all particular qualities of the spectrum.

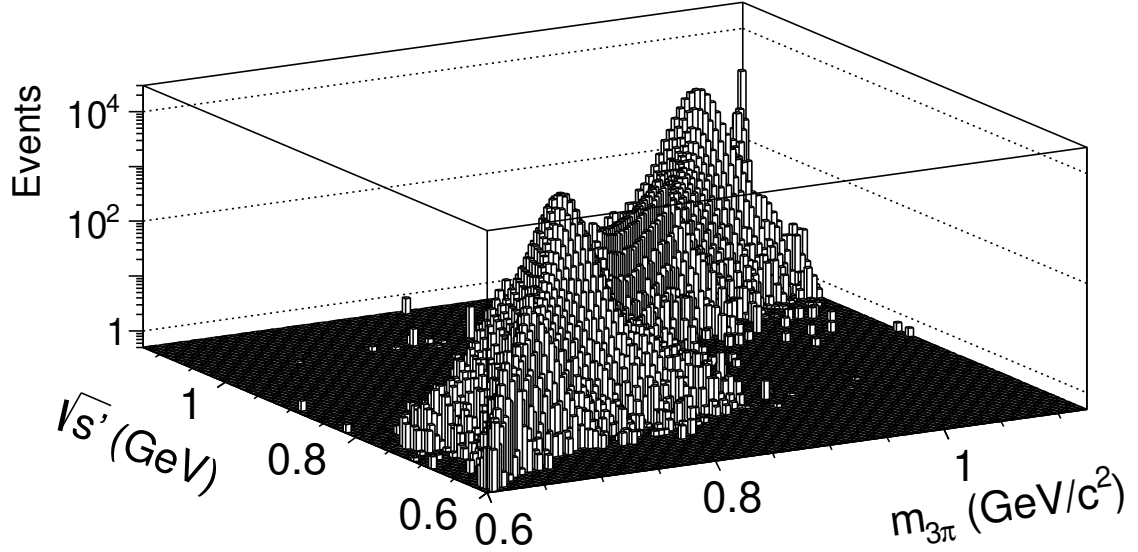


FIG. 33: The mass-transfer matrix giving the number of events generated with a (true) mass $\sqrt{s'}$ in a bin j and reconstructed with a (measured) mass $m_{3\pi}$ in a bin i .

Regularization parameter is chosen in that way to minimize dependence of unfolding result on the fluctuation of input data. We consider two TOY MC spectra, each with the number of events equaled to the number in data. The first spectrum corresponds to the fit to $m_{3\pi}$ spectrum discussed in previous section while the second spectrum is based on the fit with excluded amplitude $\rho(770) \rightarrow 3\pi$. A relative deviation of the spectra is shown by the line in the figure 34. Then both spectra were convoluted with folding matrix P_{ij} and were statistically fluctuated according to the errors in data. Finally, the spectra were subjected to the same unfolding procedure. The relative deviation of two reconstructed arrays is shown also in the figure 34 by points with error bars. The regularization parameter was tuned in that way to minimize the difference between the line and points in the figure.

Statistical uncertainty of unfolding result was calculated in a large set of fluctuated data spectra. The fluctuation corresponds to the experimental statistical errors. The same unfolding procedure is applied to each of 1000 data sets. Figure 35 shows the difference of unfolded spectrum with the result of approximation discussed in previous section. Error bars

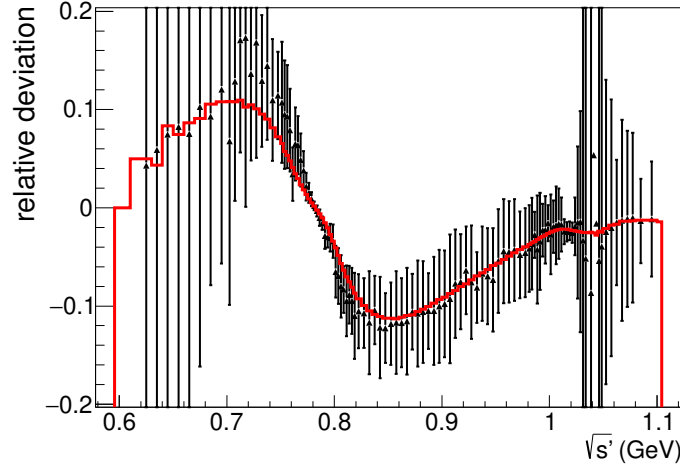


FIG. 34: (line) Relative ratio of two true TOY MC spectra used for the tuning of regularization parameters. (points with error bars) Relative ratio of unfolded data corresponded to the two TOY MC spectra.

correspond to the roots of diagonal elements of covariance matrix of unfolded spectrum. The comparison demonstrates agreement of fit results and unfolding, that confirms correctness of the model used in the fit.

Eq. (13) and unfolded 3π mass spectrum allow to calculate the Born cross section as listed in Table VII where the first error is the root of diagonal element of covariance matrix [49] and the second error is systematic. Systematic errors include uncertainties in background subtraction, luminosity, radiative correction and detection efficiency, uncertainties of unfolding procedure. As listed in Table VI, the uncertainty in detection efficiency (1.1%) dominates. Different contributions to the uncertainty of unfolding and background subtraction are shown in Fig. 36 in comparison with relative diagonal statistical errors of unfolded spectrum. Labels “ 4π ”, “ 2π ” correspond to the change of results if the unfolding made with scaled contributions of the channels as discussed in Sec. IV F. The plot “fsr” corresponds to the change of unfolding results if the FSR contribution to background did not taken into account. Besides the single iteration unfolding procedure we made additional iteration and changes in the result were included into systematic errors. Additionally we studied the dependence of unfolded spectrum on the Lorentzian smearing. Total systematic uncertainty

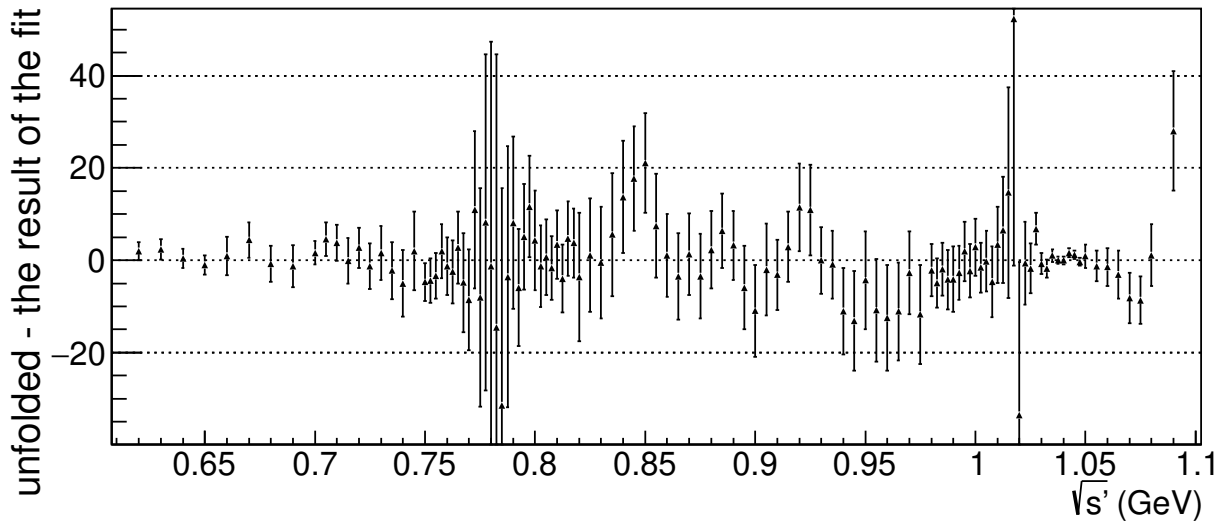


FIG. 35: The comparison of unfolded spectrum with the result of the fit of 3π mass spectrum discussed in Sec. VI. Error bars correspond to the roots of diagonal elements of covariance matrix of unfolded spectrum.

is estimated as the root of quadratic sum of all contributions.

VIII. MEASUREMENT OF THE $e^+e^- \rightarrow \pi^+\pi^-\pi^0$ CROSS SECTION ABOVE 1.1 GeV/c^2

Above $1.1 \text{ GeV}/c^2$ the resolution effects distort the 3π mass spectrum insignificantly. We test this by a convolution of the theoretical mass spectrum (13) in the mass range $1\text{--}2 \text{ GeV}/c^2$ with the resolution function obtained using simulation. The observed difference between the true and “measured” spectra does not exceed 1%. Therefore, the $e^+e^- \rightarrow \pi^+\pi^-\pi^0$ in the mass region $1.1\text{--}3.5 \text{ GeV}c^2$ is determined as

$$\sigma_{3\pi}(m) = \frac{(dN/dm)^{meas}}{\varepsilon R dL/dm}. \quad (19)$$

The obtained cross section is listed in Table VIII. The quoted errors are statistical and systematic. The latter includes uncertainties in the integrated luminosity (0.4%) and radiative correction (0.5%), the statistical (0.3–2.4%), systematic (1.7–1.8%), and model (1.5%)

TABLE VII: The reconstructed 3π invariant mass ($\sqrt{s'}$), the $e^+e^- \rightarrow \pi^+\pi^-\pi^0$ cross section. The first error is the root of diagonal element of cross section covariance matrix, the second is systematic.

$\sqrt{s'}$ (GeV)	$\sigma_{3\pi}$ (nb)	$\sqrt{s'}$ (GeV)	$\sigma_{3\pi}$ (nb)
0.62 – 0.63	0.191 \pm 0.085 \pm 0.039	0.875 – 0.88	10.582 \pm 0.410 \pm 0.143
0.63 – 0.64	0.245 \pm 0.097 \pm 0.038	0.88 – 0.885	10.591 \pm 0.404 \pm 0.143
0.64 – 0.65	0.222 \pm 0.077 \pm 0.026	0.885 – 0.89	10.567 \pm 0.438 \pm 0.139
0.65 – 0.66	0.251 \pm 0.081 \pm 0.012	0.89 – 0.895	10.266 \pm 0.426 \pm 0.132
0.66 – 0.67	0.445 \pm 0.136 \pm 0.025	0.895 – 0.9	9.701 \pm 0.420 \pm 0.128
0.67 – 0.68	0.744 \pm 0.154 \pm 0.059	0.9 – 0.905	9.391 \pm 0.428 \pm 0.143
0.68 – 0.69	0.815 \pm 0.139 \pm 0.023	0.905 – 0.91	9.782 \pm 0.410 \pm 0.130
0.69 – 0.7	1.187 \pm 0.153 \pm 0.026	0.91 – 0.915	9.727 \pm 0.382 \pm 0.130
0.7 – 0.705	1.769 \pm 0.184 \pm 0.024	0.915 – 0.92	10.052 \pm 0.376 \pm 0.131
0.705 – 0.71	2.359 \pm 0.253 \pm 0.136	0.92 – 0.925	10.508 \pm 0.427 \pm 0.163
0.71 – 0.715	2.782 \pm 0.275 \pm 0.045	0.925 – 0.93	10.588 \pm 0.430 \pm 0.139
0.715 – 0.72	3.146 \pm 0.300 \pm 0.051	0.93 – 0.935	10.216 \pm 0.373 \pm 0.135
0.72 – 0.725	4.164 \pm 0.300 \pm 0.088	0.935 – 0.94	10.350 \pm 0.386 \pm 0.143
0.725 – 0.73	5.006 \pm 0.328 \pm 0.068	0.94 – 0.945	10.116 \pm 0.412 \pm 0.133
0.73 – 0.735	6.699 \pm 0.350 \pm 0.091	0.945 – 0.95	10.301 \pm 0.443 \pm 0.136
0.735 – 0.74	8.525 \pm 0.397 \pm 0.112	0.95 – 0.955	11.002 \pm 0.427 \pm 0.145
0.74 – 0.745	11.364 \pm 0.487 \pm 0.201	0.955 – 0.96	11.119 \pm 0.438 \pm 0.174
0.745 – 0.75	16.334 \pm 0.551 \pm 0.244	0.96 – 0.965	11.514 \pm 0.429 \pm 0.173
0.75 – 0.7525	20.453 \pm 0.575 \pm 0.344	0.965 – 0.97	12.186 \pm 0.451 \pm 0.177
0.7525 – 0.755	24.953 \pm 0.616 \pm 0.386	0.97 – 0.975	13.282 \pm 0.423 \pm 0.189
0.755 – 0.7575	30.941 \pm 0.659 \pm 0.460	0.975 – 0.98	13.839 \pm 0.462 \pm 0.198
0.7575 – 0.76	39.414 \pm 0.753 \pm 0.518	0.98 – 0.9825	15.074 \pm 0.475 \pm 0.212
0.76 – 0.7625	49.814 \pm 0.824 \pm 1.224	0.9825 – 0.985	15.573 \pm 0.475 \pm 0.756
0.7625 – 0.765	65.016 \pm 0.913 \pm 1.589	0.985 – 0.9875	16.704 \pm 0.492 \pm 0.971
0.765 – 0.7675	88.409 \pm 0.968 \pm 1.147	0.9875 – 0.99	17.573 \pm 0.501 \pm 0.264
0.7675 – 0.77	123.019 \pm 1.299 \pm 1.583	0.99 – 0.9925	18.866 \pm 0.536 \pm 0.269
0.77 – 0.7725	181.584 \pm 1.628 \pm 2.375	0.9925 – 0.995	20.574 \pm 0.480 \pm 0.433
0.7725 – 0.775	289.397 \pm 2.143 \pm 4.610	0.995 – 0.9975	23.004 \pm 0.513 \pm 1.959
0.775 – 0.7775	490.723 \pm 3.029 \pm 6.409	0.9975 – 1	25.328 \pm 0.483 \pm 0.952
0.7775 – 0.78	884.607 \pm 4.722 \pm 11.358	1 – 1.0025	29.302 \pm 0.546 \pm 0.702
0.78 – 0.7825	1383.388 \pm 6.847 \pm 19.894	1.0025 – 1.005	34.048 \pm 0.492 \pm 6.642
0.7825 – 0.785	1344.120 \pm 6.718 \pm 17.716	1.005 – 1.0075	41.873 \pm 0.516 \pm 3.229
0.785 – 0.7875	856.545 \pm 4.941 \pm 11.109	1.0075 – 1.01	54.170 \pm 0.645 \pm 1.534
0.7875 – 0.79	504.097 \pm 3.050 \pm 6.466	1.01 – 1.0125	78.473 \pm 0.660 \pm 1.064
0.79 – 0.7925	316.256 \pm 2.241 \pm 4.628	1.0125 – 1.015	132.141 \pm 1.026 \pm 2.485
0.7925 – 0.795	212.732 \pm 1.679 \pm 2.784	1.015 – 1.0175	289.739 \pm 2.365 \pm 3.807
0.795 – 0.7975	154.342 \pm 1.225 \pm 2.153	1.0175 – 1.02	543.652 \pm 4.918 \pm 7.117
0.7975 – 0.8	117.491 \pm 1.216 \pm 1.800	1.02 – 1.0225	250.388 \pm 2.348 \pm 3.328
0.8 – 0.8025	91.893 \pm 1.036 \pm 1.195	1.0225 – 1.025	65.971 \pm 0.540 \pm 0.871
0.8025 – 0.805	74.100 \pm 0.942 \pm 1.151	1.025 – 1.0275	21.115 \pm 0.372 \pm 0.528
0.805 – 0.8075	61.780 \pm 0.976 \pm 0.838	1.0275 – 1.03	8.377 \pm 0.275 \pm 0.222
0.8075 – 0.81	52.221 \pm 0.849 \pm 0.771	1.03 – 1.0325	2.912 \pm 0.192 \pm 0.273
0.81 – 0.8125	45.622 \pm 0.826 \pm 0.617	1.0325 – 1.035	0.872 \pm 0.175 \pm 0.142
0.8125 – 0.815	39.234 \pm 0.780 \pm 0.559	1.035 – 1.0375	0.333 \pm 0.118 \pm 0.176
0.815 – 0.8175	35.692 \pm 0.744 \pm 0.505	1.0375 – 1.04	0.033 \pm 0.071 \pm 0.154
0.8175 – 0.82	31.970 \pm 0.689 \pm 0.422	1.04 – 1.0425	0.054 \pm 0.054 \pm 0.073
0.82 – 0.825	27.145 \pm 0.697 \pm 0.368	1.0425 – 1.045	0.320 \pm 0.073 \pm 0.175
0.825 – 0.83	23.193 \pm 0.626 \pm 0.306	1.045 – 1.0475	0.485 \pm 0.069 \pm 0.109
0.83 – 0.835	20.059 \pm 0.557 \pm 0.273	1.0475 – 1.05	0.591 \pm 0.062 \pm 0.134
0.835 – 0.84	18.081 \pm 0.620 \pm 0.257	1.05 – 1.055	0.986 \pm 0.090 \pm 0.083
0.84 – 0.845	16.768 \pm 0.616 \pm 0.259	1.055 – 1.06	1.322 \pm 0.131 \pm 0.109
0.845 – 0.85	15.628 \pm 0.624 \pm 0.252	1.06 – 1.065	1.689 \pm 0.164 \pm 0.116
0.85 – 0.855	14.710 \pm 0.576 \pm 0.356	1.065 – 1.07	1.952 \pm 0.212 \pm 0.227
0.855 – 0.86	13.155 \pm 0.523 \pm 0.221	1.07 – 1.075	2.049 \pm 0.211 \pm 0.110
0.86 – 0.865	12.155 \pm 0.427 \pm 0.173	1.075 – 1.08	2.275 \pm 0.210 \pm 0.063
0.865 – 0.87	11.367 \pm 0.416 \pm 0.164	1.08 – 1.09	2.931 \pm 0.198 \pm 0.048
0.87 – 0.875	11.165 \pm 0.429 \pm 0.147	1.09 – 1.1	3.758 \pm 0.233 \pm 0.051

TABLE VIII: Measured $e^+e^- \rightarrow \pi^+\pi^-\pi^0$ cross section above 1.1 GeV/ c^2 . The first error is statistical, the second is systematic.

$M_{3\pi}$ (GeV/ c^2)	$\sigma_{3\pi}$ (nb)	$M_{3\pi}$ (GeV/ c^2)	$\sigma_{3\pi}$ (nb)
1.100–1.125	$4.29 \pm 0.23 \pm 0.22$	2.000–2.025	$0.42 \pm 0.07 \pm 0.05$
1.125–1.150	$4.19 \pm 0.22 \pm 0.23$	2.025–2.050	$0.41 \pm 0.07 \pm 0.05$
1.150–1.175	$4.83 \pm 0.23 \pm 0.24$	2.050–2.075	$0.43 \pm 0.07 \pm 0.05$
1.175–1.200	$4.97 \pm 0.23 \pm 0.25$	2.075–2.100	$0.47 \pm 0.07 \pm 0.05$
1.200–1.225	$4.58 \pm 0.22 \pm 0.24$	2.100–2.125	$0.54 \pm 0.07 \pm 0.06$
1.225–1.250	$4.78 \pm 0.22 \pm 0.26$	2.125–2.150	$0.45 \pm 0.07 \pm 0.05$
1.250–1.275	$4.94 \pm 0.22 \pm 0.31$	2.150–2.175	$0.38 \pm 0.06 \pm 0.04$
1.275–1.300	$4.89 \pm 0.22 \pm 0.40$	2.175–2.200	$0.31 \pm 0.06 \pm 0.03$
1.300–1.325	$4.64 \pm 0.22 \pm 0.42$	2.200–2.225	$0.40 \pm 0.06 \pm 0.04$
1.325–1.350	$4.45 \pm 0.21 \pm 0.33$	2.225–2.250	$0.33 \pm 0.06 \pm 0.04$
1.350–1.375	$4.32 \pm 0.20 \pm 0.25$	2.250–2.275	$0.43 \pm 0.06 \pm 0.05$
1.375–1.400	$4.12 \pm 0.19 \pm 0.20$	2.275–2.300	$0.31 \pm 0.06 \pm 0.03$
1.400–1.425	$3.94 \pm 0.19 \pm 0.17$	2.300–2.325	$0.25 \pm 0.05 \pm 0.03$
1.425–1.450	$4.19 \pm 0.19 \pm 0.16$	2.325–2.350	$0.23 \pm 0.05 \pm 0.03$
1.450–1.475	$4.03 \pm 0.18 \pm 0.15$	2.350–2.375	$0.23 \pm 0.05 \pm 0.02$
1.475–1.500	$3.72 \pm 0.18 \pm 0.14$	2.375–2.400	$0.21 \pm 0.05 \pm 0.02$
1.500–1.525	$3.88 \pm 0.18 \pm 0.14$	2.400–2.425	$0.25 \pm 0.05 \pm 0.03$
1.525–1.550	$4.23 \pm 0.19 \pm 0.15$	2.425–2.450	$0.24 \pm 0.04 \pm 0.03$
1.550–1.575	$4.80 \pm 0.20 \pm 0.17$	2.450–2.475	$0.23 \pm 0.04 \pm 0.03$
1.575–1.600	$4.95 \pm 0.20 \pm 0.18$	2.475–2.500	$0.16 \pm 0.04 \pm 0.02$
1.600–1.625	$5.28 \pm 0.20 \pm 0.19$	2.500–2.525	$0.18 \pm 0.04 \pm 0.02$
1.625–1.650	$4.82 \pm 0.19 \pm 0.19$	2.525–2.550	$0.19 \pm 0.04 \pm 0.02$
1.650–1.675	$4.11 \pm 0.18 \pm 0.18$	2.550–2.575	$0.20 \pm 0.04 \pm 0.02$
1.675–1.700	$2.79 \pm 0.16 \pm 0.16$	2.575–2.600	$0.20 \pm 0.04 \pm 0.02$
1.700–1.725	$1.93 \pm 0.14 \pm 0.13$	2.600–2.625	$0.15 \pm 0.04 \pm 0.02$
1.725–1.750	$1.87 \pm 0.13 \pm 0.11$	2.625–2.650	$0.15 \pm 0.04 \pm 0.02$
1.750–1.775	$1.51 \pm 0.12 \pm 0.09$	2.650–2.675	$0.14 \pm 0.04 \pm 0.02$
1.775–1.800	$1.36 \pm 0.12 \pm 0.08$	2.675–2.700	$0.13 \pm 0.04 \pm 0.01$
1.800–1.825	$1.22 \pm 0.11 \pm 0.14$	2.700–2.800	$0.040 \pm 0.032 \pm 0.005$
1.825–1.850	$0.91 \pm 0.10 \pm 0.11$	2.800–2.900	$0.053 \pm 0.030 \pm 0.006$
1.850–1.875	$1.11 \pm 0.10 \pm 0.12$	2.900–3.000	$0.061 \pm 0.022 \pm 0.007$
1.875–1.900	$0.73 \pm 0.09 \pm 0.08$	3.000–3.100	$0.027 \pm 0.030 \pm 0.003$
1.900–1.925	$0.64 \pm 0.09 \pm 0.07$	3.100–3.200	$0.036 \pm 0.025 \pm 0.004$
1.925–1.950	$0.58 \pm 0.09 \pm 0.07$	3.200–3.300	$0.015 \pm 0.025 \pm 0.002$
1.950–1.975	$0.43 \pm 0.08 \pm 0.05$	3.300–3.400	$0.017 \pm 0.021 \pm 0.002$
1.975–2.000	$0.49 \pm 0.08 \pm 0.05$	3.400–3.500	$0.031 \pm 0.016 \pm 0.003$

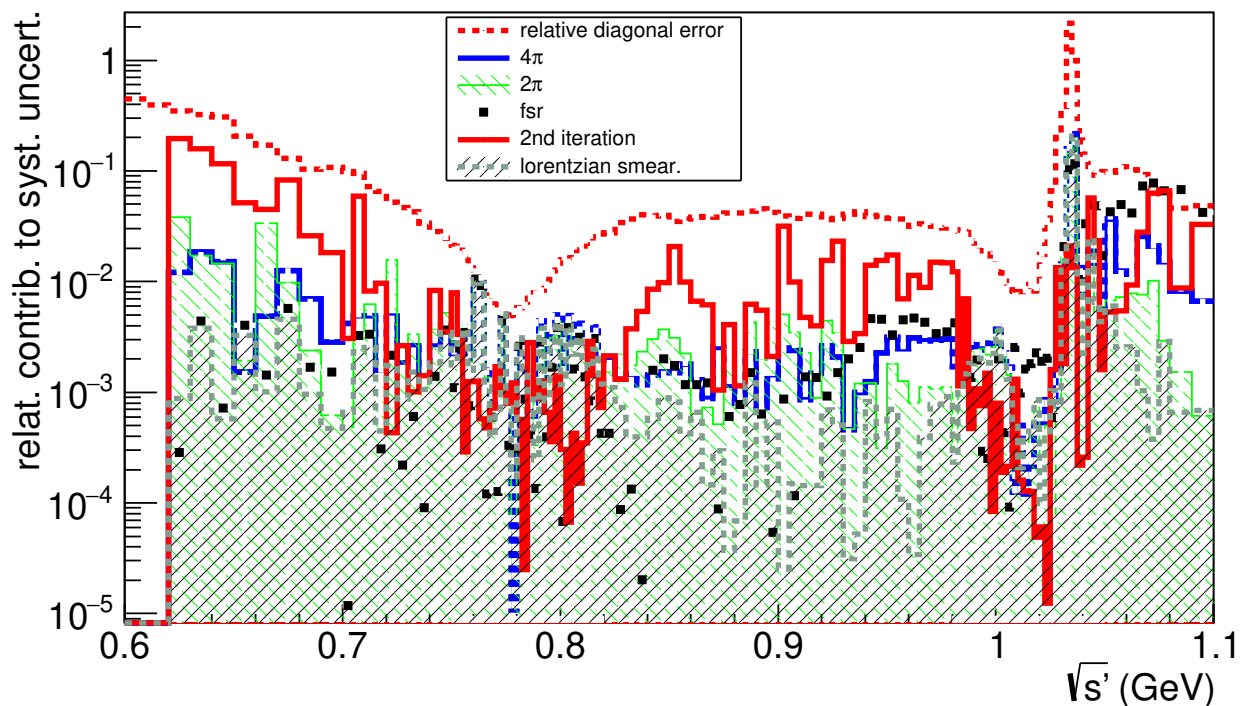


FIG. 36: Relative values of systematic uncertainties of cross section from the part of different sources. Relative diagonal errors of unfolded spectrum is shown by dashed line.

uncertainties in the detection efficiency, and the uncertainty associated with background subtraction (3–15%).

In Fig. 37 (left) the measured cross section is compared with the SND measurement [7] in the mass range 1.1–2 GeV/ c^2 . The sizable difference between the two measurements is observed near 1.25 GeV/ c^2 and 1.5 GeV/ c^2 . The cross section above 2 GeV is shown in Fig. 37 (right). The comparison of the current measurement with the previous BABAR result [6] is demonstrated in Fig. 38. The results are in reasonable agreement.

IX. THE $e^+e^- \rightarrow \pi^+\pi^-\pi^0$ CONTRIBUTION TO a_μ

The leading order hadronic contribution to the muon anomalous magnetic moment is calculated using the measured total hadronic cross section via the dispersion integral (see, for example, Ref. [43])

$$a_\mu = \frac{\alpha^2}{3\pi^2} \int_{m_\pi^2}^{\infty} \frac{K(s)}{s} R(s) ds, \quad (20)$$

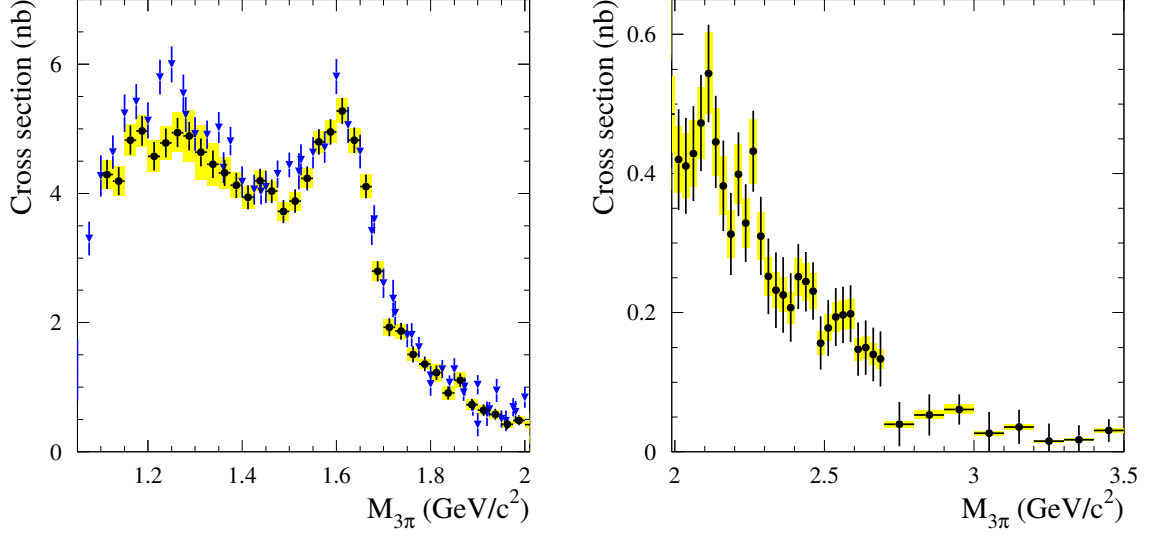


FIG. 37: The $e^+e^- \rightarrow \pi^+\pi^-\pi^0$ cross section measured in this work (circles) in comparison with the SND result [7] (triangles). For the BABAR data the error bar represents the statistical error, while the shaded box shows the systematic uncertainty. For the SND data only statistical error is shown, the systematic uncertainty is 4.4%

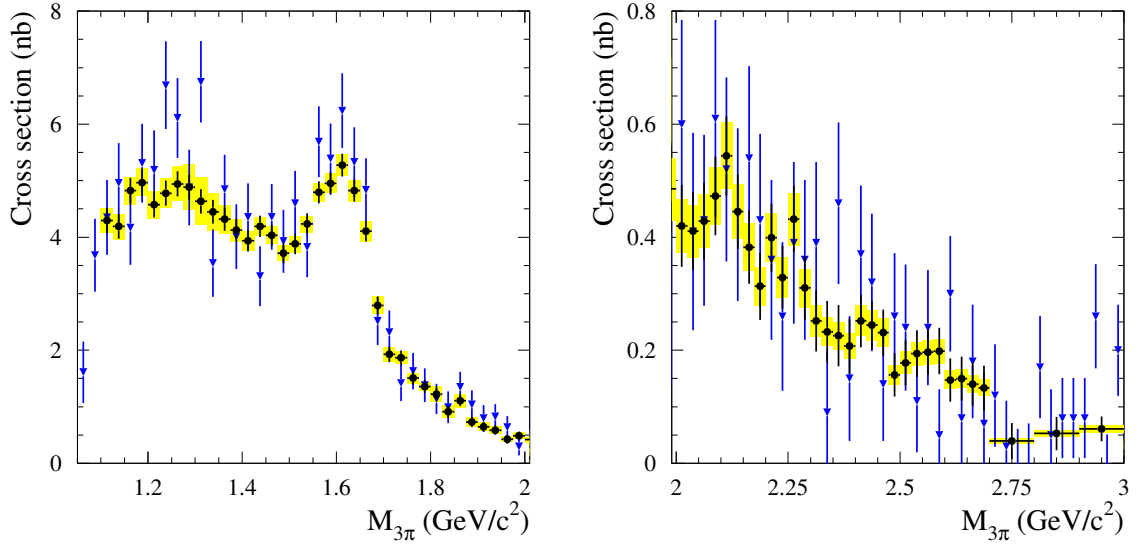


FIG. 38: The $e^+e^- \rightarrow \pi^+\pi^-\pi^0$ cross section measured in this work (circles) in comparison with the previous BABAR result [6] (triangles). For the data obtained in this work the error bar represents the statistical error, while the shaded box shows the systematic uncertainty. For the previous BABAR data [6] the statistical and systematic errors are combined in quadrature.

where the kernel function can be found in Ref. [43] and

$$R(s) = \frac{\sigma_0(e^+e^- \rightarrow \text{hadrons})(s)}{4\pi\alpha^2/s}. \quad (21)$$

Here σ_0 is the bare cross section, excluding effects from vacuum polarization.

To calculate $a_\mu^{3\pi}$ we substitute $\sigma_0(e^+e^- \rightarrow \text{hadrons})(s)$ in Eq. (21) by $\sigma_{3\pi}(s)|1 - \Pi(s)|^2$. The vacuum polarization operator $\Pi(s)$ is tabulated in Ref. [44]. The integral (20) is substituted by a sum over mass bins with $s = M_{3\pi,i}^2$. In the sum the values of the functions K and dL/dm are taken at the center of the bin. To estimate the uncertainty due to substituting of the integral by the sum, we perform $a_\mu^{3\pi}$ calculations using the theoretical cross section (15) and mass spectrum (13). The difference between the sum and integral is found to be 0.03% for the mass range 0.62–1.1 GeV/ c^2 and 0.007% for the mass range 1.1–2.0 GeV/ c^2 .

$$a_\mu^{3\pi}(0.415 - 0.62) = 5.7 \times 10^{-13}, \quad (22)$$

$$a_\mu^{3\pi}(0.62 - 1.1) = (42.905 \pm 0.141_{\text{stat}} \pm 0.550_{\text{syst}} \pm 0.XXX_{\text{VP}}) \times 10^{-10},$$

The statistical uncertainty is obtained as standard deviation of the values $a_\mu^{3\pi}$ calculated with fluctuated data sets as described in Sec. VII. The systematic uncertainty corresponds to the root of quadratic sum of uncertainties of unfolding procedure, background subtraction as well as uncertainties in luminosity, radiative correction and detection efficiency.

X. MEASUREMENT OF THE $J/\psi \rightarrow \pi^+\pi^-\pi^0$ DECAY

The 3π mass spectrum in the J/ψ mass region for data events selected with the standard criteria is shown in Fig. 39. The small width of the J/ψ resonance leads to negligible peaking background. In particular, $e^+e^- \rightarrow J/\psi\gamma \rightarrow K^+K^-\pi^0\gamma$ events reconstructed under the $3\pi\gamma$ hypothesis have the 3π invariant mass in the range 2.8 to 3.0 GeV/ c^2 . To determine the number of J/ψ events, the spectrum is fitted with a sum of a resonance distribution and a linear background. The resonance line shape is a Breit-Wigner function convolved with a triple-Gaussian function describing detector resolution. The Breit-Wigner width is fixed at its nominal value [40]. The parameters of the resolution function are determined from simulation. To account for possible difference in detector response between data and simulation,

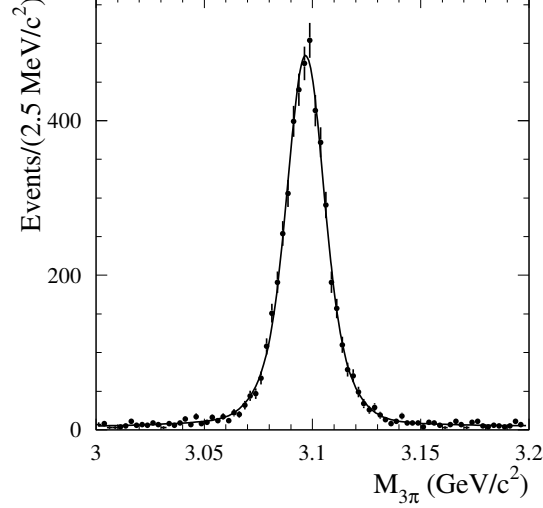


FIG. 39: The 3π mass spectrum for selected events in the J/ψ mass region. The curve is the result of the fit described in the text.

the simulated resolution function is modified by adding in quadrature an additional σ_s to the standard deviations of the triple-Gaussian function. The free parameters in the fit are the number of resonance events ($N_{J/\psi}$), the number of nonresonant background events, the slope of the background, σ_s , and the resonance mass.

The result of the fit is shown in Fig. 39. The fitted resonance parameters are following: $N_{J/\psi} = 4921 \pm 74$, $\sigma_s^2 = 1.8 \pm 2.6 \text{ MeV}^2/c^4$, and $M_{J/\psi} = 3.0962 \pm 0.0002 \text{ GeV}/c^2$. The latter differs from the nominal J/ψ mass ($3096.900 \pm 0.006 \text{ MeV}/c^2$) by $-(0.7 \pm 0.2) \text{ MeV}/c^2$, while the σ_s value is consistent with zero.

The differential cross section for ISR production of a narrow resonance, such as J/ψ can be calculated using [12]

$$\frac{d\sigma(s, \theta)}{d\cos\theta} = \frac{12\pi^2\Gamma(J/\psi \rightarrow e^+e^-)\mathcal{B}(J/\psi \rightarrow 3\pi)}{m_{J/\psi}s} W(s, x_{J/\psi}, \theta), \quad (23)$$

where $m_{J/\psi}$ and $\Gamma(J/\psi \rightarrow e^+e^-)$ are the J/ψ mass and electronic width, $x_{J/\psi} = 1 - m_{J/\psi}^2/s$, and $\mathcal{B}(J/\psi \rightarrow 3\pi)$ is the branching fraction of the decay $J/\psi \rightarrow \pi^+\pi^-\pi^0$. Therefore, the measurement of the number of $J/\psi \rightarrow \pi^+\pi^-\pi^0$ decays in the $e^+e^- \rightarrow \pi^+\pi^-\pi^0\gamma$ reaction determines the product of the electronic width and the branching fraction $\Gamma(J/\psi \rightarrow e^+e^-)\mathcal{B}(J/\psi \rightarrow 3\pi)$.

The cross section for $e^+e^- \rightarrow J/\psi\gamma \rightarrow \pi^+\pi^-\pi^0\gamma$ for $20^\circ < \theta_\gamma < 160^\circ$ is calculated as

$$\sigma(20^\circ < \theta_\gamma < 160^\circ) = \frac{N_{J/\psi}}{\varepsilon R L} = (114.7 \pm 1.7 \pm 2.4) \text{ fb}. \quad (24)$$

Here $L = 468.6 \pm 2.0 \text{ fb}^{-1}$, $R = 1.0091 \pm 0.0050$, and the detection efficiency ε corrected for the data-MC difference in the detector response and the decay model is $(9.07 \pm 0.18)\%$, where the error includes the systematic uncertainty (1.8%) and the MC statistical error (0.8%). From the measured cross section and Eq. (23), the following product is determined:

$$\Gamma(J/\psi \rightarrow e^+e^-)\mathcal{B}(J/\psi \rightarrow 3\pi) = (0.1248 \pm 0.0019 \pm 0.0026) \text{ keV}. \quad (25)$$

Using the PDG value $\Gamma(J/\psi \rightarrow e^+e^-) = (5.51 \pm 0.10) \text{ keV}$ [40] we obtain

$$\mathcal{B}(J/\psi \rightarrow 3\pi) = (2.265 \pm 0.034 \pm 0.062)\%, \quad (26)$$

which is in reasonable agreement with the average PDG value $(2.10 \pm 0.08)\%$ [40] and the most precise measurement $(2.137 \pm 0.064)\%$ by the BESIII collaboration [45].

XI. SUMMARY

-
- [1] M. Davier, A. Hoecker, B. Malaescu and Z. Zhang, Eur. Phys. J. C **80**, 241 (2020) [erratum: Eur. Phys. J. C **80**, 410 (2020)]
 - [2] M. N. Achasov *et al.* (SND Collaboration), Phys. Rev. D **63**, 072002 (2001).
 - [3] M. N. Achasov *et al.* (SND Collaboration), Phys. Rev. D **68**, 052006 (2003).
 - [4] R. R. Akhmetshin *et al.* (CMD-2 Collaboration), Phys. Lett. B **578**, 285 (2004).
 - [5] R. R. Akhmetshin *et al.* (CMD-2 Collaboration), Phys. Lett. B **642**, 203 (2006).
 - [6] B. Aubert *et al.* (BABAR Collaboration), Phys. Rev. D **70**, 072004 (2004).
 - [7] M. N. Achasov *et al.* (SND Collaboration), Eur. Phys. J. C **80**, 993 (2020).
 - [8] M. Ablikim *et al.* (BESIII Collaboration), arXiv:1912.11208 [hep-ex].
 - [9] M. Ablikim *et al.* (BESIII Collaboration), Phys. Rev. D **98**, 112007 (2018).
 - [10] A. Aloisio *et al.* (KLOE Collaboration), Phys. Lett. B **561**, 55 (2003) Erratum: [Phys. Lett. B **609**, 449 (2005)].

- [11] J. P. Lees *et al.* (BABAR Collaboration), Phys. Rev. D **95**, 072007 (2017).
- [12] M. Benayoun *et al.*, Mod. Phys. Lett. A **14**, 2605 (1999).
- [13] B. Aubert *et al.* (BABAR Collaboration), Nucl. Instrum. and Meth. A **479**, 1 (2002);
B. Aubert *et al.* (BABAR Collaboration), Nucl. Instrum. and Meth. A **729**, 615 (2013).
- [14] H. Czyz and J.H. Kuhn, Eur. Phys. J. C **18**, 497 (2001).
- [15] M. Caffo, H. Czyz, and E. Remiddi, Nuo. Cim. **110A**, 515 (1997); Phys. Lett. B **327**, 369 (1994).
- [16] E. Barberio and Z. Was, Comput. Phys. Commun. **79**, 291 (1994).
- [17] T. Sjostrand, Comput. Phys. Commun. **82**, 74 (1994).
- [18] S. Jadach, B. Ward, and Z. Was, Comput. Phys. Commun. **130**, 260 (2000).
- [19] S. Agostinelli *et al.*, Nucl. Instr. and Meth. A **506**, 250 (2003).
- [20] B. Aubert *et al.* (BABAR Collaboration), Phys. Rev. D **77**, 092002 (2008).
- [21] G. S. Adams *et al.* (CLEO Collaboration), Phys. Rev. D **73**, 012002 (2006).
- [22] G. P. Lepage and S. J. Brodsky, Phys. Rev. D **22**, 2157 (1980); S. J. Brodsky and G. P. Lepage, Phys. Rev. D **24**, 2848 (1981).
- [23] V. L. Chernyak and A. R. Zhitnitsky, Phys. Rept. **112**, 173 (1984).
- [24] K. Belous *et al.* (Belle Collaboration), Phys. Lett. B **681**, 400 (2009).
- [25] C. P. Shen *et al.* (Belle Collaboration), Phys. Rev. D **88**, 052019 (2013).
- [26] N. N. Achasov, V. V. Gubin and E. P. Solodov, Phys. Rev. D **55**, 2672-2682 (1997).
- [27] B. Aubert *et al.* (BABAR Collaboration), Phys. Rev. D **74**, 012002 (2006).
- [28] V. L. Chernyak, Private communication.
- [29] R. C. Verma, J. Phys. G **39**, 025005 (2012).
- [30] H. Y. Cheng, Y. Koike and K. C. Yang, Phys. Rev. D **82**, 054019 (2010).
- [31] J. P. Lees *et al.* (BABAR Collaboration), Phys. Rev. D **92**, no.7, 072015 (2015).
- [32] A. Ballon-Bayona, G. Krein and C. Miller, Phys. Rev. D **91**, 065024 (2015).
- [33] . Barnes, F. E. Close, P. R. Page and E. S. Swanson, Phys. Rev. D **55**, 4157 (1997).
- [34] C. Q. Pang, L. P. He, X. Liu and T. Matsuki, Phys. Rev. D **90**, 014001 (2014); K. Chen, C. Q. Pang, X. Liu and T. Matsuki, Phys. Rev. D **91**, 074025 (2015).
- [35] V. A. Shchegelsky, A. V. Sarantsev, A. V. Anisovich and M. P. Levchenko, Eur. Phys. J. A **27**, 199 (2006).
- [36] H. Czyz, A. Grzelinska, J. H. Kuhn and G. Rodrigo, Eur. Phys. J. C **47**, 617 (2006).

- [37] G. Rodrigo, H. Czyz, J. H. Kuhn and M. Szopa, Eur. Phys. J. C **24**, 71 (2002).
- [38] Z. Jakubowski *et al.* (Crystal Ball Collaboration), Z. Phys. C **40**, 49 (1988).
- [39] J. P. Lees *et al.* (BABAR Collaboration), Nucl. Instrum. Meth. A **726**, 203 (2013).
- [40] P.A. Zyla *et al.* (Particle Data Group), Prog. Theor. Exp. Phys. **2020**, 083C01 (2020).
- [41] A.B. Clegg and A. Donnachie, Z. Phys. C **62**, 455 (1994).
- [42] K. Maltman, H. B. O’Connell and A. G. Williams, Phys. Lett. B **376**, 19 (1996); C. E. Wolfe and K. Maltman, Phys. Rev. D **80**, 114024 (2009); **83**, 077301 (2011).
- [43] T. Aoyama *et al.* Phys. Rept. **887**, 1 (2020).
- [44] F. Ignatov, <https://cmd.inp.nsk.su/ignatov/vpl>
- [45] M. Ablikim *et al.* (BESIII Collaboration), Phys. Lett. B **710**, 594 (2012).
- [46] B. Malaescu, [ArXiv: 0907.3791](https://arxiv.org/abs/0907.3791).
- [47] J.P. Lees *et al.* (BABAR Collaboration), Physical Review D **86**, 032013 (2012).
- [48] J.P. Lees *et al.* (BABAR Collaboration), Physical Review D **88**, 032013 (2013).
- [49] https://raw.githubusercontent.com/eakozyrev/3pi_unfold/main/rec_cov_cr.dat